THE UNIVERSITY *of* EDINBURGH

Subsurface Seismic Imaging in the Presence of Multiply Scattered Waves

Angus Lomas

Doctor of Philosophy

University of Edinburgh

2019

To my family and friends.

We shall not cease from exploration
And the end of all our exploring
Will be to arrive where we started
And know the place for the first time.

T.S. Eliot

Declaration

I declare that this thesis was composed by myself, that the work contained herein is my own except where explicitly stated otherwise in the text, and that this work has not been submitted for any other degree or professional qualification except as specified.

Angus Lomas

May 2019

Abstract

The aim of seismic imaging is to produce maps indicative of spatial variations in properties of the Earth's subsurface. To create such images geophysicists use seismograms of energy measured over time by receivers at fixed observation points. These seismograms partially sample the seismic wavefield and are used to estimate the interactions between the seismic wavefield and the subsurface heterogeneity. However, because observation points are limited spatially the true interactions are unknown so approximations must be made to estimate these interactions. Conventional methods make the assumption that seismic waves observed in the seismograms reflect or diffract at most once from the subsurface heterogeneity (the so-called Born approximation). This assumption allows a low-wavenumber smoothly varying estimate of the subsurface velocity structure to be used to back extrapolate the observed seismic wavefield to points inside the subsurface – producing an estimate of the subsurface seismic wavefield. However, this approximation can lead to inaccuracies when the seismograms contain energy that has reflected or diffracted more than once. In this thesis we create a suite of methods that offer a solution to this problem in a variety of scenarios.

The majority of this thesis focuses on a set of novel techniques called Marchenko methods. These enable us to project seismograms to points in the subsurface – creating seismograms as though they had been measured at each subsurface point – while accounting for many of the complex, multiply-reflected seismic wave

interactions that take place in the real Earth's subsurface. As a result images created using Marchenko imaging contain a reduction in artifacts that usually contaminate subsurface images due to multiply-reflected seismic waves.

This thesis has four main aims which are addressed in consecutive chapters: (1) To introduce Marchenko methods with the minimum amount of mathematics required to understand how the methods iterate to a solution, and to provide a well-commented, easily editable MATLAB code package for demonstration and training purposes. (2) The second aim is to understand the application of Marchenko methods in a three-dimensional world, that is to say we investigate the implications of three-dimensional data, subsurface structures, wavefields and acquisition geometries on the results of Marchenko redatuming and imaging. (3) In a third set of results we aim to incorporate the additional wavefield sampling of vertical seismic profile (VSP) data (measured in boreholes in the Earth's subsurface) into Marchenko imaging with the emphasis being on improving imaging of vertical and near vertical subsurface interfaces. (4) The aim of the final set of results is to use multiply scattered (particularly duplex waves) as well as primary (singly scattered) waves to image the subsurface, again to improve imaging of vertical or near vertical interfaces but this time only using surface seismic data.

Overall the results of this thesis demonstrate the effectiveness of Marchenko methods to redatum and image accurately when only low-wavenumber smoothly varying estimates of the subsurface velocity structure are available. We demonstrate the applicability of the methods to three-dimensional problems and a means to include VSP data into the method. Finally, we also redefine the conditions used to create subsurface images, allowing us to image using singly and multiply scattered seismic waves.

Lay Summary

Let us imagine you, the reader, are sat in an empty space reading this document. If you were to read it aloud you would create a sound wave that moves through the space, with you at its origin.

Now imagine there is a second person in this space listening to you. They can hear your voice, but there is a delay between you speaking and when they hear you – it takes time for the sound wave to travel between you and your listener.

Let us make this thought experiment more realistic, the space is now a room which has four walls. The sound wave now interacts and reflects from the walls. For each wall your listener hears your voice for a second time; this time your voice is quieter and delayed further as the sound wave travels to the wall and then to your listener. This occurs multiple times because there are multiple walls. They are hearing a series of echoes.

Hypothetically what you are saying could be very important, in which case you may not want an echo to distort the clarity of your voice for your listener. So is there a way to create a sound wave that does not echo?

Yes, there is.

Novel developments have shown that signals (the sound wave) that could be observed at any point inside a medium can be related under certain approximations to the signal created and observed at one side of a medium. We refer to the methods that relate these two observations as Marchenko methods. These methods can be used to enhance our understanding of the properties of the medium and advances in these methods are the focus of this thesis.

Referring back to our original thought experiment, this means you could calculate the sound wave that you would need to create to account for the echo – enabling you to focus your voice at the position of your listener.

In this thesis our interest is applying Marchenko methods to create images of the Earth's subsurface using seismic waves. We first provide an intuitive demonstration of how the so-called Marchenko methods are implemented in one and two dimensions. We then extend their application to three-dimensional media. Next, we incorporate additional observations: seismic signals collected from a borehole to improve the results of Marchenko imaging. Finally, we reformulate the way we use these methods to create images, allowing us to use different types of waves when creating images of the subsurface.

Acknowledgements

It would not have been possible to complete the research within this thesis without the help and support of many people. Firstly, I would like to thank my supervisors: Andrew Curtis, Mark Chapman and Satyan Singh. I would like to thank Andrew and Mark for giving me the opportunity to work with them for the past three years. Andrew has provided invaluable guidance on the direction of this research, but has also given me the freedom to explore my own ideas. I would also like to thank Satyan, who has always made time to answer my questions, has spent many hours discussing this research and has always been enthusiastic about the results.

I would also like to acknowledge the input of my friends and colleagues at the University of Edinburgh, many of whom have provided technical contributions to, or welcomed relief from this thesis: Ali, Amjad, Atif, Berit, Claire, Dom, Eva, Felix, Flo, James, Jonathan, Megan, Phil, Ribanna, Richard, Steph and Xin. Furthermore, I would like to thank two former members of the University of Edinburgh, Carlos and Giovanni, who during their time in Edinburgh were always happy to answer my questions.

Finally, I would like to thank my parents, grandparents and brother for their support and encouragement during my studies in Edinburgh.

Contents

List of Tables

List of Figures

Chapter 1

Introduction

1.1 The Imaging Problem

The motivation of all wave-based imaging methods is to create a representation of a medium that indicates the spatial variations in its properties. These methods are useful because it is often unfeasible or impractical to make measurements of these properties directly. The alternative is therefore to inject some form of energy, commonly on the surface of the target medium, and measure how the medium responds. The measured response provides information about the medium through which the signals have travelled, and these signals can be manipulated so as to create a map of the properties of the medium.

To readers outside of the subject area, the imaging problem may appear relatively simple. For instance, it is routine in medical applications to use X-rays for imaging; in this case an electromagnetic wave is created, transmitted through a medium (the human body) and the measured response is indicative of the properties of the medium. For this example the measurement points and/or the

wave source points can be located such that they surround the target medium – which is always relatively small. Further applications of wave-based imaging include but are not limited to: non-destructive testing (e.g. structural monitoring of buildings), ground penetrating radar for near surface (e.g. glacial) imaging and seismic imaging on a variety of scales ranging from near surface ($< 10m$) to global seismology ($> 1000km$). All of these methods rely on similar theory but each has its own challenges in term of possible acquisition geometries, the quality and quantity of data that can be acquired and the time available to go from data acquisition to images.

This thesis focuses on exploration scale seismology. It is unusual to have illumination from more than one side of the medium (the surface of the Earth), and the imaging target is often several kilometres away form the energy source and the receiver locations. However, there is often an abundance of data available and the requirement for high quality results means that a significant amount of time is devoted to refining the images produced.

1.2 The Seismic Wavefield

Let us begin with the seismic wavefield – approximately elastic waves that move through and interact with geological features in the Earth's subsurface. In seismic imaging we try to understand the wavefield propagation at all points inside the medium. If there is any form of scattering (deflection or reflection) or directional change in the wavefield as it moves through the subsurface, that is indicative of a change in the properties of the medium. However, as we discussed in the previous section, it is unfeasible to observe the seismic wavefield inside the medium; rather we have measurements of the wavefield at the observation points, commonly only along a linear array on the surface of the Earth. Therefore, given the partially sampled seismic wavefield, we want to use the recorded information to estimate

the location of the subsurface features that interacted with and scattered the observed wavefield components. The subsurface imaging problem can therefore be described mathematically as a problem in the form $\mathbf{d} = F(\mathbf{m})$, where $\mathbf{d}$ is the observed data, in this case the measured signals, $\mathbf{m}$ is the medium which we aim to image, and F is the operator that maps a given medium $\mathbf{m}$ to the data $\mathbf{d}$. For seismic imaging problems the operator F is the wave equation, which governs how seismic waves move through a medium. We can measure $\mathbf{d}$, we have a reasonably good understanding of the wavefield physics F and we want to accurately calculate the model $\mathbf{m}$ (or a representation of its properties).

Throughout this thesis we assume that the mapping operator F is the variable density acoustic wave equation, and because all examples presented herein are synthetic (computer simulations) this equation is known to be accurate. The most logical step would be to set this problem up as an inverse problem which solves for the model parameters $\mathbf{m}$, a technique known as full waveform inversion (FWI) (Tarantola, 1984; Pratt *et al.*, 1998; Virieux and Operto, 2009). However, this equation is highly non-linear and inverting for the global minimum is nearly impossible. In particular, it is challenging to solve for the high wavenumber variations in the model parameters – it is these variations that are of particular interest to geoscientists. Therefore, an alternative approach is often taken, which we follow in this thesis, instead of solving for $\mathbf{m}$ we solve for a map indicative of changes in the subsurface properties.

For both of these techniques however we required some knowledge of the wavefield physics and throughout this thesis we assume this is the variable density acoustic wave equation, where the observed wavefield is dependent on four parameters: time (t), space ($\mathbf{x}_i$), velocity (v) and density (ρ). In practice the Earth is more complex than this and more accurate wave equations (elastic, anisotropic, viscoelastic) better describe the actual seismic wave propagation. However, the synthetic data we present do not contain the more complex wave attributes

associated with such equations, so these more complex topics are limited to points of discussion.

1.3 Seismic Imaging

In this thesis we will focus on seismic imaging techniques, in particular migration methods which are used to create subsurface maps representative of changes in acoustic impedance ($= \rho v$). Migration methods are often divided into two groups: pre-stack and post-stack methods. The process of *stacking* data involves first grouping seismic data into so-called common mid-point (CMP) gathers, where the CMP is the surface location half-way between the source and receiver locations, and a CMP *gather* is the group or subset of all data that share approximately the same CMP. These data are adjusted to make them compatible in various senses and are then summed (stacked) together such that random noise is attenuated in the result (Mayne, 1962). This data is now a stacked seismic section, a set of spatially varying seismic traces that form a representation of variations in the subsurface properties, these can be migrated (post-stack), a process which attempts to move the observed seismic energy to the correct subsurface location in the section. A limitation of this technique is that scattered events in the observed seismic wavefield are initially assumed to have formed at a location directly below the CMP – the so-called 'zero-dip' assumption (Yilmaz, 2001). This assumption is inaccurate in almost all cases, therefore in this thesis we focus on the alternative, more accurate, *pre-stack* migration.

The migration methods that we focus on throughout this thesis all rely on similar principles. The seismic data observed at the surface of the Earth is propagated backwards in time from the receiver positions, this creates an estimate of the subsurface wavefield prior to its measurement at the surface but after scattering. Simultaneously, a source term is forward propagated in time from the initial

source position, this produces an estimate of the wavefield prior to scattering. Both of these wavefields use an estimate of the subsurface velocity (and density) structure for propagation, hence they do not perfectly represent the true seismic experiment. Nevertheless, an imaging condition is then applied to the two wavefields, this tests their similarity in time and space – the wavefields should be most similar at the scattering locations and a high level of similarity produces a relatively large contribution to the final image.

The formulation described above to create subsurface images can be derived from the adjoint-state approach (Plessix and Mulder, 2004), which solves for the unknown perturbations in model parameters (relative to the initial model). When only a smoothly varying estimate of the subsurface velocity (and density) structure is available this should correspond to the location of high-wavenumber variations of interest. This is also the first step in solving the FWI problem described in the preceding section.

However, alternative formulations also exist for describing how images of the subsurface can be created. Firstly, a relationship can be derived from one-way reciprocity theorums by solving for the subsurface reflection response (R). This reflection response is related to the upgoing ($-$) and downgoing ($+$) signals (G) from a source at $\mathbf{x}_0$ measured at a subsurface point $\mathbf{x}_i$ or $\mathbf{x}_i'$ on a subsurface boundary $\partial\mathbb{D}_i$ through (Wapenaar *et al.*, 2008):

$$G^{-}(\mathbf{x}_i, \mathbf{x}_0, \omega) = \int_{\partial\mathbb{D}_i} R(\mathbf{x}_i, \mathbf{x}_i', \omega) G^{+}(\mathbf{x}_i', \mathbf{x}_0, \omega) d\mathbf{x}_i' \tag{1.1}$$

This equation can then be solved for the refelctivity R at a range of image point ($\mathbf{x}_i$) and taking the zero offset, zero time component of the reflectivity will allow an image to be constructed. However, this relies on signal decomposition in the

up and down direction at the image point – the potential limitations of this will be discussed in more detail in chapters 4 and 5. A final method for describing image formulation is given by taking the zero time component of a scattered signal (G_s) when both the source and receiver are at an image point ($\mathbf{x}_i$):

$$I(\mathbf{x}_i) = G_s(\mathbf{x}_i, \mathbf{x}_i, t = 0) \tag{1.2}$$

There are several alternative methods suggested for obtaining G_s, Vasconcelos (2008) discusses these in more detail and provides an exact formulation based on representation theorems. Whilst each of the formulations described above to create images are different in their theoretical foundations they all rely on similar principles. That is, taking the observed seismic data, estimating the appearance of that data at a subsurface image point and using that to create an image.

In practice, three of the most prominent methods of pre-stack migration are: Kirchhoff migration, one-way wave-equation migration (OWEM) and reverse time migration (RTM). The first, Kichhoff migration (Schneider, 1978; Buske, 1999; Yilmaz, 2001) uses the eikonal equation (Vidale, 1988; van Trier and Symes, 1991; Aki and Richards, 2002) to trace rays and calculate source to image-point to receiver travel times. The travel times are then used to extrapolate the seismic data into the subsurface. This method is advantageous because of its flexibility and low computational cost. However, it is often unsuitable in areas where the subsurface is structurally complex. This is because computing a single point to point travel time will be inappropriate when there are multiple direct paths between the surface acquisition array and subsurface image points. Secondly OWEM methods use an approximation of the full two-way wave equation from equation 1.2 that only allows wave propagation that include a component in a single direction (usually downwards) (Claerbout, 1971). Again, this is then used

to extrapolated data to the subsurface image point. However, this approximation is limited as often it is unable to handle subsurface structures that are steeply dipping (Etgen, 1994; Mulder and Plessix, 2004). Finally, RTM methods use the full two-way wave equation to extrapolate the data into the subsurface (Baysal *et al.*, 1983; McMechan, 1983; Whitmore, 1983). This is the most accurate of the imaging methods discussed as it accurately represents the physics from equation 1.2, although the numerical solutions we implement to solve equation 1.2 are always approximate (Kelly *et al.*, 1976; Galetti *et al.*, 2013).

In this thesis we consider the implications of imaging when multiply scattered waves are present in the observed seismic wavefield. We begin in Figure 1.1 by defining these components of the seismic wavefield. Throughout this thesis we subdivide the components that we observe in the scattered wavefield into singly scattered components (primaries) and multiply scattered components (multiples). The first of these, primaries, are components of the wavefield that have scattered exactly once inside the subsurface of the Earth, an example of which is shown in Figure 1.1a. If the observed component of the wavefield has scattered more than once it is a multiply scattered wave, these components can manifest themselves in a variety of ways depending on the path they have taken through the subsurface of the Earth. The first of these, shown in Figure 1.1b, is a first-order internal multiple which has scattered three times inside the subsurface, reverberating between layers. The second in Figure 1.1c is a first-order surface-related multiple which has scattered from within the subsurface as well as from the free-surface of the Earth. Finally, in Figure 1.1d we have included a special form of multiply scatted wave, a duplex wave, which has scattered twice inside the subsurface, wavefield components like these predominantly form in the presence of steeply dipping subsurface structures.

A problem with all of the migration methods we have described is that if the estimated velocity model is inaccurate (which it always is), they are unable to

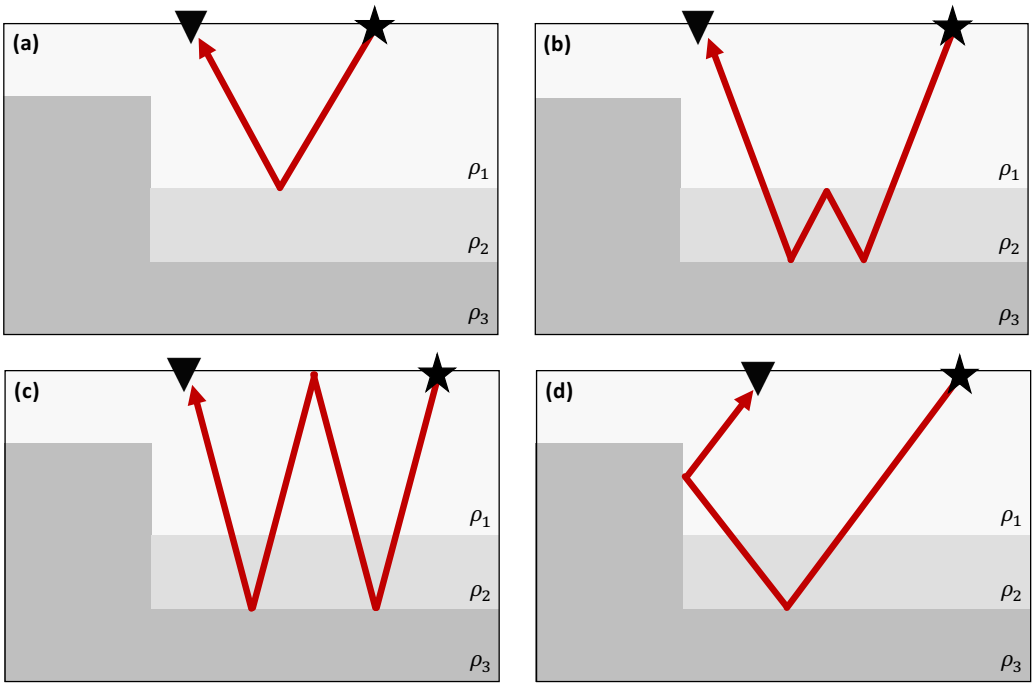

Figure 1.1: A comparison of the ray-paths of scattered waves through a synthetic subsurface model. Panel (a) shows a singly scattered wave (primary) and panels (b)-(d) show multiply scattered waves (multiples). More specifically, panel (b) shows an internal multiple, panel (c) shows a free-surface multiple and panel (d) shows a duplex wave. In all diagrams the black star represents a seismic source, the black triangle a receiver and the red lines the travel path of the observed wavefield component.

account for multiply scattered seismic waves. More specifically, multiply scattered waves are assumed to be primaries and produce 'false' scattering points in the image. There are two approaches that can be taken to accurately image the subsurface in the presence of multiply scattered waves. The multiply scattered components can either be removed from the measured data (Verschuur *et al.*, 1992; Weglein *et al.*, 1997; Jakubowicz, 1998; Amundsen, 2001), or imaging methods that accurately account for them can be developed and deployed (Malcolm *et al.*, 2009; Vasconcelos, 2013; Wapenaar *et al.*, 2014). The former is much more common because of its simplicity, however none of the methods commonly implemented are perfect. Alternatively, the latter is a rapidly developing field because the multiply scattered waves potentially include additional information about the subsurface which can be used to improve imaging results.

1.4 Thesis Outline

In the preceding section we have reviewed the way in which we use seismic data to create images of the subsurface and the impact of multiply scattered waves when images are created using these techniques. The aim of the work within this thesis is to overcome the limitations of imaging in the presence of such waves. We consider techniques for both using and accounting for multiply scattered waves, this includes the three forms of multiple described in Figure 1.1. The majority of this thesis focusses on so-called Marchenko methods, which we introduce in detail in chapter 2. The main body of this thesis, which follows the preface, consists of seven chapters, this chapter (the introduction) is the first. We then present a comprehensive methodology chapter and three results chapters before the sixth and seventh chapters, which are the Discussion and Conclusion respectively. Below I summarise each of the upcoming chapters, in which I use "we" rather than "I" since all of this work was conducted with co-authors (I was the lead author in all submitted articles).

In **Chapter 2** we introduce, the Marchenko methods with the minimum amount of mathematics required to understand how they can iterate to a solution. We also provide a well-commented, easily editable MATLAB code package for demonstration and training purposes. Green's function estimation using the Marchenko method is first illustrated for a constant velocity, variable density, one-dimensional medium, with results that show a near perfect match when compared to true, synthetically modelled solutions. Similar quality results are shown for variable velocity, two-dimensional Green's function estimation. Finally, we show how these estimates can be used to create images of the subsurface, which, when compared to standard methods contain reduced contamination due to multiple-related artifacts. The accompanying code package includes the two-dimensional dataset required to reconstruct the relevant figures presented, and allows readers to experiment with the implementation of the Marchenko method and the application of Marchenko imaging.

In **Chapter 3** we investigate the application of Marchenko methods to three-dimensional data, subsurface structures and wavefields. We first show that for waves propagating in three dimensions, Marchenko methods can be applied to seismic data collected using both linear (so-called 2D-seismic) and areal (3D-seismic) acquisition arrays. However, for 2D acquisition arrays the Marchenko workflow requires additional dimensionality correction factors to obtain accurate solutions, even in a subsurface that only varies with depth. Without these correction factors phase errors occur in redatumed Marchenko estimates; these errors propagate through the Marchenko algorithm and create depth errors in the Marchenko images. Furthermore, applying Marchenko methods to fully three-dimensional seismic wavefields recorded by linear (2D-seismic) arrays that contain out-of-plane reflections deteriorates surface-to-subsurface Green's function estimates with spurious energy and resulting images are less accurate than those

created using 'conventional' imaging methods. The application of fully three-dimensional Marchenko methods using data recorded on areal arrays solves both of the above problems, creating accurately redatumed wavefields and images with reduced artifact contamination. However, it appears that source/receiver spacing at most of $\lambda_A \big/ 4$ is required for accurate results using existing Marchenko methods, where λ_A is the dominant wavelength. This is impractical in many real 3D seismic acquisition scenarios, so different algorithms may be required to implement Marchenko methods in the 3D Earth.

In **Chapter 4** we exploit recent theoretical advances that enable both virtual sources and virtual receivers to be placed at arbitrary points inside the subsurface as a means to incorporate vertical seismic profile (VSP) data into Marchenko methods. The advantage of including this type of data is that the additional acquisition boundary increases subsurface illumination, which in turn enables vertical interfaces and steeply dipping structures to be imaged. We demonstrate this methodology on two synthetic datasets. The first is a simple, variable density, constant velocity model. We show in this example that our newly devised VSP Marchenko imaging methodology enables imaging of both horizontal and vertical structures and that optimum results are achieved by combining these images with those created using standard Marchenko imaging. A second example demonstrates that the method can be applied to more realistic subsurface structures, in this case a modified version of the *Marmousi2* model. We show the applicability of the methods to image fault structures with the final imaging result containing reduced contamination due to internal multiples and an improvement in the imaging of fault structures when compared to other standard imaging methods alone.

In **Chapter 5** we suggest a new imaging method, Heaviside imaging, which uses multiply as well as singly scattered components of the seismic wavefield to create images of the subsurface. We first demonstrate that this method is capable of

improving seismic imaging results of vertical interfaces on two synthetic datasets, a step model and the *Amoco* model. However, it is shown, in the same way as for conventional imaging, that this method is vulnerable to imaging artifacts as a result of multiply scattered seismic waves in the input seismic data. We therefore combine Heaviside and Marchenko imaging into a single method that is shown on a final synthetic model to image horizontal and vertical interfaces whilst containing a greatly reduced number of artifacts due to multiples.

In **Chapter 6** we discuss the findings of this thesis and consider four topics: First we review plane-wave Marchenko imaging, which offers reduced computation cost for three-dimensional Marchenko methods. Second, we investigate errors in Marchenko imaging, identifying prominent errors in estimated Green's functions, their cause and the implications for imaging complex subsurface structures. We then contemplate the theory of Marchenko methods and the issues that need to be considered before widespread applications are possible. Finally, we consider the way which we approach seismic imaging problems, the data processing flow we apply for subsurface imaging, and its role within in the exploration workflow.

Finally, in **Chapter 7** we make some concluding remarks about the overall outputs of the work: the advances we have made, the potential applications and the opportunities for further research.

1.5 Publications

A significant proportion of the work presented in this thesis has been published in, or submitted to, peer-reviewed journal articles or conference proceedings. Below is a list of these publications. This work is all collaborative but in each case I am the lead author. I therefore acknowledge my co-authors in the preamble of the chapter to which they have contributed. I made a significant contributions to

every aspect of the work presented, my co-authors contributions were primarily technical discussions and editorial changes. Furthermore, I recognise those who have made other specific contributions in the acknowledgements of each chapter.

1.5.1 Journal Articles

Lomas, A. and Curtis, A., 2019. An introduction to Marchenko methods for imaging. Geophysics, 84(2), pp.F35-F45.

Lomas, A. and A. Curtis, 2018, Marchenko Methods in a Three-dimensional World: Journal Geophysical International, **Submitted**.

Lomas, A., Singh, S., and A. Curtis, 2018, Imaging Vertical Structures using Marchenko Methods with Vertical Seismic Profile Data: Geophysics, **Submitted**.

1.5.2 Conference Proceedings

Lomas, A. and Curtis, A., 2017, December. 3D Seismic Imaging using Marchenko Methods. In AGU Fall Meeting Abstracts. American Geophysical Union.

Lomas, A. and Curtis, A., 2018, June. 3D Marchenko Redatuming Using 2D and 3D Seismic Data. In 80th EAGE Conference and Exhibition 2018. European Association of Geoscientists and Engineers.

Lomas, A., Singh, S. and Curtis, A., 2018, October. Marchenko imaging of both vertical and horizontal interfaces using VSP data. In SEG Technical Program Expanded Abstracts 2018 (pp. 5027-5031). Society of Exploration Geophysicists.

Chapter 2

An Introduction to Marchenko Methods for Imaging

Angus Lomas[1] **and Andrew Curtis**[1,2]

This chapter focusses on introducing Marchenko methods, and for simplicity we have kept the mathematics to a minimum, whilst maintaining sufficient detail to explain how Marchenko methods operate. For readers who are interested in these details, they are included in appendix A and the upcoming chapters. Furthermore, to aid intuition and understanding we have provided a set of MATLAB codes which are discussed in the text and included in appendix B. These codes provide readers with further details on implementing Marchenko methods and with these many of the two-dimensional examples presented in this chapter are reproducible.

[1]School of GeoSciences, University of Edinburgh, Edinburgh, UK
[2]Institute of Geophysics, ETH Zurich, Zurich, Switzerland

2.1 Introduction

The aim of seismic imaging is to map unknown heterogeneities in the Earth's subsurface, given a wavefield measured on or close to the Earth's surface. An approximate seismic wave speed model, usually called a velocity model, is required in order to map the subsurface accurately. This model provides a basic level of understanding about how seismic waves propagate through the subsurface and allows seismic information measured at the surface to be mapped to approximately correct subsurface locations. Much effort goes into estimating the velocity model using migration velocity analysis (Yilmaz, 2001; Sava and Biondi, 2004), travel time tomography (Stork, 1992; Jones, 2010) and full waveform inversion (Tarantola, 1984; Pratt *et al.*, 1998; Virieux and Operto, 2009) but it is always imperfect. In particular it is usually far more smooth than the true Earth and therefore is not kinematically accurate; in other words it does not map waves that reflect from abrupt interfaces to their true subsurface positions. Even when these errors are sufficiently small that the image produced is correctly positioned, the inaccuracies usually cause other additional artifacts to be superimposed on the final image. Artifacts that are often most troublesome are those created by recorded seismic waves that reflect more than once in the subsurface, called multiples. This tutorial explains a set of methods that account for such waves so that these artifacts do not occur.

Marchenko methods (Rose, 2001; Broggini *et al.*, 2012) are data-driven methods that use measured surface seismic data and an approximate velocity model to calculate the signal that would have been recorded at the surface if an impulsive, frequency band-limited source had fired at each chosen subsurface image point – including multiples. The estimated signals are called (frequency band-limited) Green's functions, and are exactly the information needed for accurate subsurface imaging (Behura *et al.*, 2014; Wapenaar *et al.*, 2014), seismic

redatuming (Wapenaar *et al.*, 2014) or identifying and removing multiples (Meles *et al.*, 2014, 2016).

The name Marchenko comes from the author of the original work on inverse scattering (Marchenko, 1955) who devised methods to estimate Green's functions in the field of quantum mechanics in one dimension (Snieder (2015) provides more information about this application). More recently a solution to the so-called Marchenko equations was formulated for geophysical applications that allow two and three-dimensional media to be imaged under certain approximations (Wapenaar *et al.*, 2013; Lomas and Curtis, 2017).

This chapter presents an intuitive introduction to the Marchenko method and its applications. The aim is not to introduce fundamentally new concepts but to provide an easily accessible guide to some of the key concepts and methods that already exist. Additionally, a Marchenko MATLAB code and a relevant dataset accompany this chapter: the code is well commented, easily editable and adaptable for two-dimensional seismic problems. It is constructed so as to give readers further insight into the workflow used to calculate Green's functions using Marchenko methods, and to allow them to experiment and gain comfort with the methods - rather than being geared towards computationally efficient construction of large seismic images. Nevertheless, all two-dimensional examples presented herein were constructed using this code, hence it is perfectly sufficient to be used to teach and learn about Marchenko methods, and to process small datasets. Other codes exist in the public domain (e.g. Thorbecke *et al.* (2017)) but our code is designed specifically for user experimentation and so is written in a more intuitively accessible (higher-level) programming language. It is therefore also ideal as an aid to teaching about Marchenko methods in Masters or professional development courses.

Marchenko methods are simplest, most intuitive, and most accurate for one-dimensional problems, so the first section of this chapter introduces Green's functions estimation for a simple one-dimensional medium in which full wavefields can be displayed and understood. We then introduce the reader to two-dimensional examples, the accompanying MATLAB code and the application of Marchenko imaging. Throughout this chapter multiple datasets are used: all are constructed in acoustic media and exclude free surface multiples as such data allow the simplest and most studied form of Marchenko methods to be applied. However, theory exists for Marchenko methods using elastic data (da Costa Filho *et al.*, 2014, 2015; Wapenaar, 2014; Wapenaar and Slob, 2014) and data containing surface-related multiples (Singh *et al.*, 2015, 2016). There are also limited examples of applications to real data (Ravasi *et al.*, 2016; Jia *et al.*, 2017; Wapenaar *et al.*, 2018). For an entirely non-mathematical introduction to Marchenko methods we refer readers to van der Neut *et al.* (2015d), or for an introduction to one-dimensional Marchenko methods see Cui *et al.* (2018b); for a thorough introduction to the more sophisticated mathematical aspects of the Marchenko methods see Slob *et al.* (2014b), Wapenaar *et al.* (2014) or van der Neut *et al.* (2015b) . Our tutorial fills the niche between these studies by introducing the concepts, the mathematics, and the computational machinery in an accessible way, with a code designed to facilitate experimentation and education.

2.2 The Marchenko Method

There are multiple applications of Marchenko methods (imaging, redatuming, constructing primaries and multiple removal) but they all have the same foundation, namely Green's function estimation. Green's functions are the waves that arrive at a receiver location due to the firing of a spatio-temporally impulsive

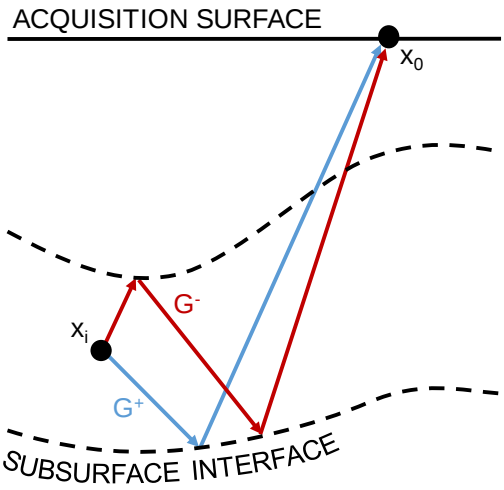

Figure 2.1: Illustration of the types of singly- or multiply-reflected signals estimated by the Marchenko method.

source. We represent these Green's functions as $G(x_0, x_i, t)$ where x_0 is the location of a receiver on the recording surface, x_i is a source point in the subsurface and t represents the time domain. In this syntax each term is a signal with two locations (x): the second always denotes the source location and the first is the receiver location. The Marchenko method estimates Green's functions between an arbitrarily chosen image point (or an artificial or virtual source) within the subsurface, and any point within the surface acquisition array (Figure 2.1).

The most basic form of Green's function estimation is to assume or estimate an initial approximate velocity model and estimate Green's functions $G(x_0, x_i, t)$ using either ray propagation or wavefield calculation through that model. This is standard practise in reverse time migration (RTM) for example (Baysal *et al.*, 1983). Marchenko methods provide a workflow to estimate Green's functions but decomposed into two constituent parts: the first part consists of all waves that are upgoing ($-$) at the image point in the Earth's subsurface while the second part consists of the downgoing ($+$) waves. This includes components of the wavefield that have undergone multiple reflections, so-called multiples. In other words two

Green's functions can be constructed from each subsurface image point which are recorded at the surface: the first G^- contains signals that start at the image point as a source wavefield propagating upward, the second G^+ contains signals that initially propagate downward from the image point and are reflected back up to the surface.

For simplicity let us begin with the one-dimensional Marchenko method. Two pieces of information are needed to calculate the decomposed Green's functions G^+ and G^-. The first is the reflectivity from a point source at the surface measured by a point receiver at the surface, denoted by $R(x_0, x_0, t)$; in the real world this is an idealised version of a one-dimensional surface seismic reflection data after surface-related multiple removal. The second is an estimate of the direct (non-reflected) wave arrival $T_d(x_i, x_0, t)$ between the surface source and an image point. The decomposed Green's functions $G^{+/-}$ between x_0 and x_i are related to the reflectivity R through additional terms f^+ and f^- which are called focusing functions and are the subject of the next section:

$$G^+(x_0, x_i, t) = f^+(x_0, x_i, t) \otimes R(x_0, x_0, t) - f^-(x_0, x_i, t) \tag{2.1}$$

$$G^-(x_0, x_i, t) = f^+(x_0, x_i, -t) - R(x_0, x_0, t) \otimes f^-(x_0, x_i, -t) \tag{2.2}$$

Equations 2.1 and 2.2 are both defined in the time domain. Symbol $-t$ (and also later in this chapter, superscript *) denotes time reversal of the signal that precedes it. This is accomplished if we simply flip the positive and negative time axis of the initial signal, an operation that corresponds to complex conjugation in the frequency domain. The symbol $\otimes$ represents a time domain convolution, which is equivalent to multiplication in the frequency domain.

It is worth noting that equations 2.1 and 2.2 differ from those given in most of the existing literature on Marchenko methods. To aid intuition we have created a virtual source at the image point inside the subsurface rather than a virtual receiver (the latter is more common). Comparing these cases, the direction of wave propagation is reversed: $G^{+}(x_0, x_i, t) = G^{-}(x_i, x_0, t)$. However the property of source-receiver reciprocity states that these are equivalent (identical signals). We will continue to use the virtual source syntax for the remainder of this chapter.

2.2.1 Focusing Functions

Focusing functions are key for understanding Marchenko methods. Imagine throwing a stone into a still pond on a windless day: ripples diverge from the location of impact, propagating as waves across the water surface. Let us imagine that these ripples are recorded on some closed boundary of receivers that surrounds the impact point. If we waited until all of the energy had settled, we could then use the receivers as sources to inject the recorded wavefield back into the pond. If we do this in time-reversed order (inject the last wave recorded at each receiver first), the original ripples will be recreated, but this time they would converge inwards rather than propagating outwards (Cassereau and Fink, 1992). They will all eventually re-focus at the impact point, then diverge outwards again, creating another wavefield that can be recorded at the receiver boundary. In this thought experiment, the (time reversed) wavefield injected on the boundary, is called a focusing function: it defines exactly which waves we should inject in order to focus the in-going energy at the impact point.

Focusing functions used in Marchenko methods are intuitively similar to those above. The only conceptual differences are that the source point in this case is the subsurface source in Figure 2.1, and that the receiver boundary is at the Earth's surface and so is only on one side of the source point. Downgoing focusing functions are related to wavefields that if injected at the Earth's surface, would

focus (collapse all of their energy to a point) at a specific location in the subsurface (here, the location of any chosen virtual source or image point). However, in the case of focusing in the subsurface, this only occurs in an idealised (truncated) model of the Earth's subsurface structure which is homogeneous below the depth of that point, but which has the true Earth's structure above that depth.

Focusing means that there is a time at which the waves at a certain depth only exist at one specific image point – everywhere else at that depth the wavefield is zero. The function f^+ is the wavefield that we would have to inject at the surface (at point x_0) in order for the wavefield to focus at the image point, and hence this wavefield is downgoing at the surface. Function f^- is the wavefield that we would record at the surface as we inject f^+ in the truncated model, hence f^- is upgoing at the surface. Both wavefields are shifted along the time axis such that the focus occurs at time zero.

Figure 2.2 includes a standard representation of a focusing function (Slob *et al.*, 2014b) for a simple one-dimensional subsurface model that consists of layers with varying density and a constant velocity. First, Figure 2.2a shows the wavefield that develops in space and time when a simple impulsive source (convolved with a Ricker wavelet) is injected at the surface at time $t = 0$ (note that time is on the horizontal axis). This consists of a direct wave (the first continuous, linear wave on the left) and a set of (singly and multiply) reflecting waves. At a particular image point in depth (for example $1400m$ - indicated by an arrow in Figure 2.2) multiple waves arrive and hence there is not a focus of energy. In order to create such a focus additional energy must be injected to cancel all but the direct wave at that point.

The focusing function is the signal at the surface ($depth = 0m$) in Figure 2.2b, shown in Figure 2.2c. The downgoing component f^+ is the signal injected at the surface in order to create the focus at $depth = 1400m$, shown by the circle in

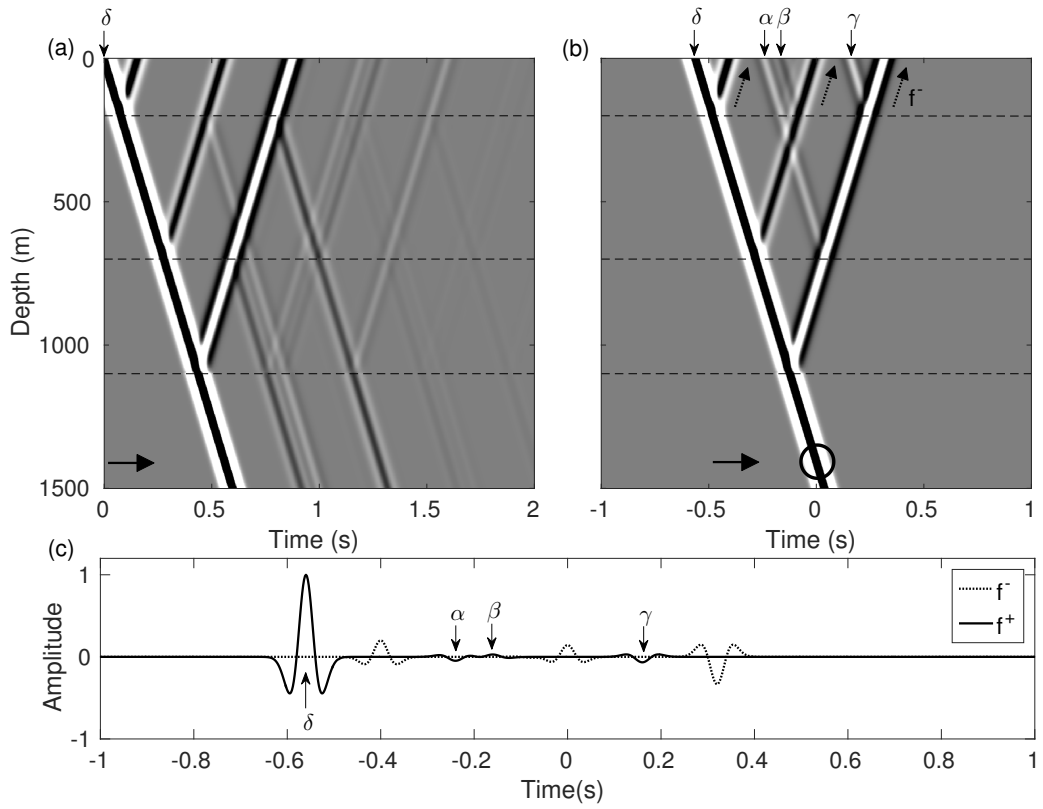

Figure 2.2: Reflectivity and focusing functions of a one-dimensional medium. The medium has a constant velocity ($2500m/s$) but variable density: dashed lines represent subsurface interfaces between layers of different densities which reflect energy. The reflectivity of the medium in panel (a) shows the location of the wavefield in space (depth) at every time for a single impulsive source (denoted δ) fired at time zero. This can be related to the focusing function in panel (b) where additional components α, β and γ are injected at the surface after the initial source δ: these cancel various reflections in the subsurface to ensure that focusing occurs in the subsurface. In this example the focusing location was chosen to be at $1400m$ depth (indicated by an arrow, and circled in panel (b)). The decomposed focusing functions (c) are the downgoing f^+ and upgoing f^- (dashed arrows) components at the surface ($depth = 0m$) in panel (b). These diagrams are of a similar form to those presented by Slob *et al.* (2014b).

Figure 2.2b. The upgoing component f^- is the reflected response observed at the surface from this injected signal. It can be seen that three pulses of energy (α, β and γ) are injected at x_0 in addition to the initial pulse δ to cancel out the reflected components of the wavefield observed in Figure 2.2a. These three signals together with δ make up the complete downgoing focusing function f^+ and all of the up-coming waves at $depth = 0m$ comprise f^-.

2.2.2 Iterative Solution

The Marchenko method works by first calculating the focusing functions and then using equations 2.1 and 2.2 to estimate the Green's functions. While the relationships between focusing functions and Green's functions in those equations is a relatively simple one, they do not explain how one can calculate focusing functions. Several methods have been proposed to do this (Broggini *et al.*, 2014; van der Neut *et al.*, 2015a,b), and here we present the method of Wapenaar *et al.* (2014) as it can be understood most intuitively.

In a one-dimensional system we assume that we know the reflectivity at the surface $R(x_0, x_0, t)$ as well as the direct arrival between the surface and the image point $T_d(x_i, x_0, t)$ – which identifies the chosen image point x_i. The first step in estimating the focusing functions is to set:

$$f_0^+(x_0, x_i, t) = T_d(x_i, x_0, t)^{-1} \tag{2.3}$$

Equation 2.3 inverts the direct arrival, commonly approximated as simply performing a time reversal (switching the time axis of T_d and setting the signal at positive times to zero: $T_d(x_i, x_0, t)^{-1} \approx T_d(x_i, x_0, -t)$). The result is used as a first approximation for f^+ denoted f_0^+ (Wapenaar *et al.*, 2014) and forms the

component δ from Figure 2.2b. This makes intuitive sense: if we time reverse the direct wave between the image point and the surface, it will propagate back to its source point (the image point) and create a pulse of energy there at zero time, just as in the example of ripples on the pond. Unfortunately though, as it propagates back into the subsurface some of its energy will scatter or reflect from heterogeneities in the Earth, creating a more complex part of the wavefield that will disrupt the focus. Marchenko methods design energy to inject in order to destructively interfere with these scattered waves, reducing them to zero amplitude.

The estimate for f_0^+ can then be used to estimate f_0^-:

$$f_0^-(x_0, x_i) = \theta(x_0, x_i, t) \left[R(x_0, x_0, t) \otimes f_0^+(x_0, x_i, t) \right] \tag{2.4}$$

Within the square brackets equation 2.4 convolves the initial estimate of f_0^+ with the reflectivity, which is equivalent to injecting f_0^+ into the Earth and recording the result at the surface. Again this is equivalent to injecting the time-reversed wavefield in the pond, and recording the reflecting waves on the source boundary. The additional term in this equation, θ, is a focusing-location dependent window which removes all energy that arrives at times greater than or equal to the direct arrival and is symmetric in time. It may appear counter intuitive to apply a window that removes all energy at these times as this is the data that we are ultimately trying to estimate in the Green's functions. However, this stage of the Marchenko method estimates the focusing functions, and these functions only exist at times *before* the direct arrival and *after* the time reversed direct arrival. Outside this window is where the Green's function exists but its accuracy is dependent on the accuracy of the focusing functions (by equations 2.1 and 2.2). Furthermore, this in itself is an approximation as we are assuming that

the Green's function and focusing functions can be separated by a windowing operator in the space-time domain, which is not always the case (e.g. when the focusing location is on or near to a subsurface interface). Nevertheless, we work with these approximations and now iterate to a solution as follows.

In Figure 2.2b three wave packets are labelled (α, β and γ): these are injected at the surface in addition to the initial impulsive source δ that is used to obtain the reflectivity in Figure 2.2a. These additional wave packets make up M_k^+ which is the coda (later part) of f_k^+, where k is the number of iterations:

$$f_k^+(x_0, x_i, t) = f_0^+(x_0, x_i, t) + M_k^+(x_0, x_i, t) \tag{2.5}$$

As a demonstration of how the focusing functions are estimated using equations 2.3 and 2.4 (and equations 2.6 and 2.7 below), Figures 2.3 and 2.4 show a series of ray path diagrams that explain their various travel time relationships. These figures use a similar display format to that presented by van der Neut *et al.* (2015b). In Figure 2.3 the three primary reflections from the reflectivity are depicted individually (middle column) and convolved with the inverted direct arrival f_0^+ (left column) from equation 2.3. The main point of Figure 2.3 is to show that the results of this convolution are a series of *non*-physical signals, each of which is contained within the pass-window of θ and make up f_0^-. They are not physical because each signal on the right is made up of combinations of energy that has positive (solid) and negative (dashed) travel times which survive the windowing operation in equation 2.3. Despite being non-physical at this stage, they can be used to construct the focusing functions by progressing them to the next iteration:

$$M_k^+(x_0, x_i, -t) = \theta(x_0, x_i, t) \left[R(x_0, x_0, t) \otimes f_{k-1}^-(x_0, x_i, -t)\right] \tag{2.6}$$

To estimate M_k^+ using equation 2.6 we start with the estimate f_{k-1}^- produced by the previous iteration (or the initial iteration f_0^-), time reverse it, and then convolve it with the reflectivity. The same windowing operator (θ) as above is then applied to isolate the focusing functions of interest.

A schematic of the first iteration ($k = 1$) to calculate M_1^+ is shown in Figure 2.4. The columns on the left of Figure 2.4 show a subset of the (time reversed) columns on the right of Figure 2.3, a subset was selected (rows 2 and 3 from Figure 2.3 only) as these are the only components that contribute to M_1^+. This column is convolved across rows with primary reflections from R; again we have only included a subset of these reflections as these are the components that contribute to M_1^+. The solutions to this convolution step are shown in the third column and the time reversal of this result is given in the final column.

The final column represents M_1^+ and is composed of three signals each of which is made up of the time reversed direct arrival (the left column in Figure 2.3) plus an additional time lag. This additional time lag is equal to the two-way travel time through one or more subsurface layers. This travel time information is what the Marchenko method requires to accurately account for internal multiples. To demonstrate this we have included the travel times $\alpha = -0.24s$, $\beta = -0.16s$ and $\gamma = 0.16s$ from Figure 2.2b and 2.2c in the column depicting M_1^+ in Figure 2.4. This shows that at $depth = 0m$ we have calculated the travel times of the signals we need to inject into the subsurface to destructively interfere with the multiply-scattered components of the reflectivity so as to cancel them out above the focus point. We have therefore demonstrated that the additional components of the focusing functions that are used in Figure 2.2b to remove multiples from the seismic reflection data can be formed by convolving the data with itself (and with the direct wave estimate). While the travel times of α, β and γ are correct, the amplitudes of the energy constructed in iteration 1 does not cause perfect cancellation of the internal multiples; amplitudes are corrected in subsequent

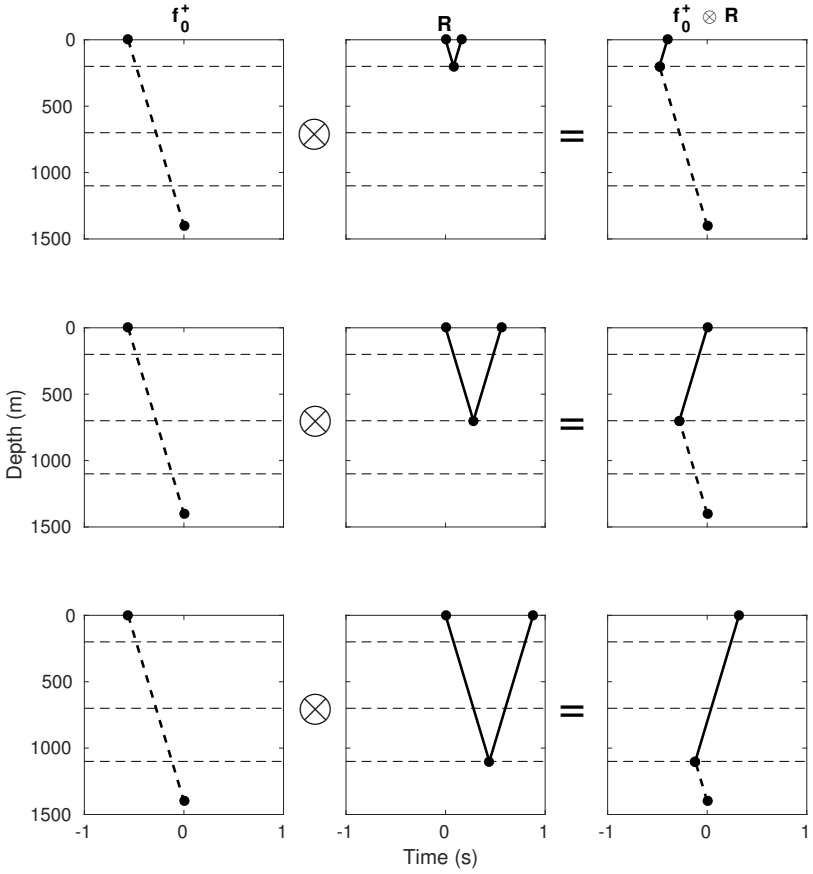

Figure 2.3: A schematic diagram of ray paths contributing to the initial focusing function estimate f_0^- using equations 2.3 and 2.4. The first column shows the inverted direct arrival f_0^+, approximated by the time reversed direct wave (note that zero time is at the centre of each horizontal axis). As stated in equation 2.3, this is convolved with the reflectivity, which in column two is decomposed into three primary reflections. The combination of these two events across each row creates the events shown in the right column which are all components of f_0^-. Dashed rays are time-reversed compared to their physical counterparts; solid rays are not time-reversed. Hence, starting at the source point at time zero, a wave in the right column would have the travel time of the solid ray segments minus the travel time along the dashed segments (and is therefore non-physical). These diagrams are of a similar form to those presented by van der Neut *et al.* (2015b).

iterations.

The waves in M_k^+ can then be injected into the subsurface and what would return to the surface can be calculated (the convolution with R); the results are windowed with θ and whatever remains is added to the estimate of f_0^-:

$$f_k^-(x_0, x_i, t) = f_0^-(x_0, x_i, t) + \theta(x_0, x_i, t) \left[R(x_0, x_0, t) \otimes M_k^+(x_0, x_i, t)\right] \qquad (2.7)$$

Equations 2.6 and 2.7 are iterated until the solutions for M_k^+ and f_k^- in consecutive iterations have converged to stable values. When the solutions have converged, the total downgoing focusing function f_k^+ can be constructed by summing the inverted direct arrival f_0^+ and M_k^+ using equation 2.5.

It is worth noting that within equations 2.4-2.7 the quantity from the previous iteration is convolved with the reflectivity (R), which in practise always contains a source term (no matter whether real or modelled data are used). To avoid iteratively convolving multiple source terms together, the source wavelet was initially deconvolved from the reflectivity. If the reflectivity was not deconvolved, the effective source wavelet would change with each iteration so consecutive iterations would be inconsistent. An alternative approach that avoids deconvolution is illustrated in the two-dimensional example below.

2.2.3 Green's Function Estimation

Once calculated, the focusing functions can be used to estimate directionally decomposed Green's functions ($G^{+/-}$) using equations 2.1 and 2.2; summing those two signals gives the total Green's function $G(x_0, x_i, t) = G^-(x_0, x_i, t) +$

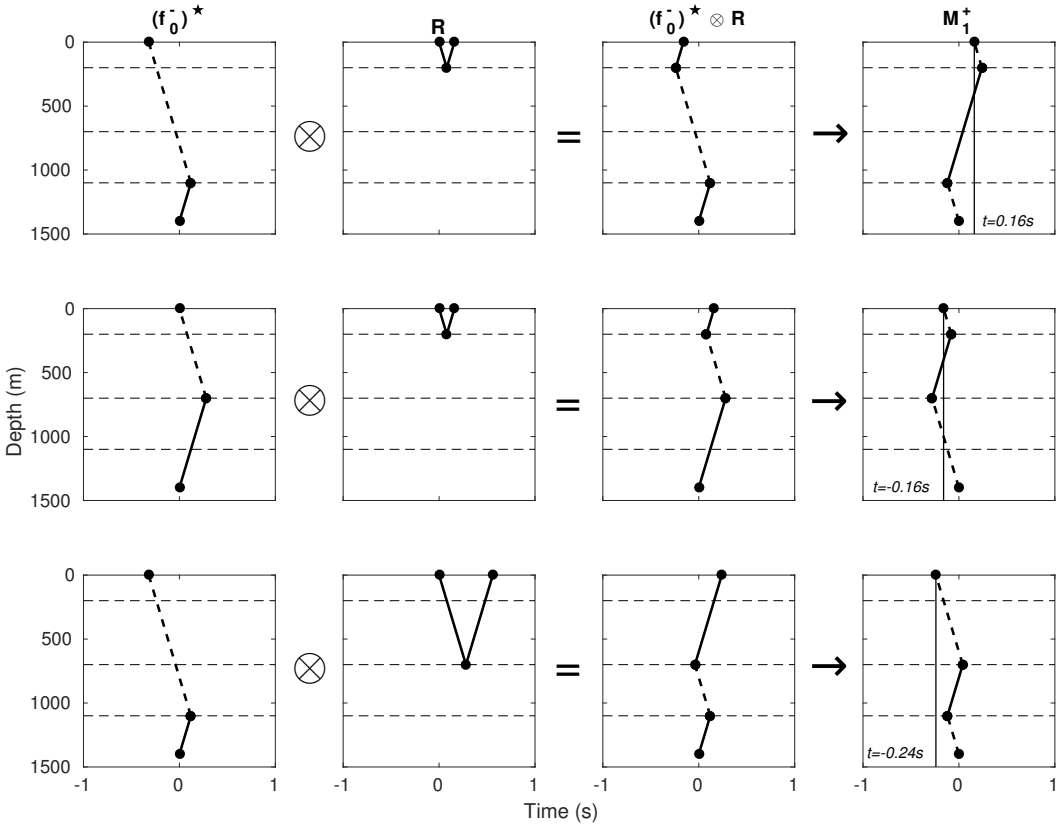

Figure 2.4: A schematic ray path diagram for the retrieval of the first estimate ($k = 1$) of $M_k^{+\star}$ using equation 2.6. The input into this step is $(f_0^-)^\star$ given in the first column which is obtained from different rows in the right column of Figure 2.3 after time reversal. This is convolved again with the reflectivity in column two (equation 2.6) and produces the results $(f_0^-)^\star \otimes R$ in column three. After windowing with θ these are the time reverse of the components that make up the later part of the downgoing focusing function injected in Figure 2.2b and c (components α, β and γ). This is shown in column 4 which is simply the time reversal of the results in column 3. These diagrams are of a similar form to those presented by van der Neut *et al.* (2015b).

$G^+(x_0, x_i, t)$. This Green's function represents the signal that would have been measured at the surface if there had been a source at the image point (or vice versa, by source-receiver reciprocity).

As this experiment is synthetic we can test the accuracy of the Green's function estimates by comparing them with the true Green's function – one that is obtained by modelling an actual source at the image point, as shown in Figure 2.5. The final panels of Figure 2.5a and 2.5b show the estimated and true Green's functions for two different subsurface image points. For both examples they match in time, and amplitudes are correct for all arrivals. In the first two panels of both Figure 2.5a and 2.5b the Green's functions are shown in decomposed form as obtained directly from equations 2.1 and 2.2: we observe well separated events in the upgoing and downgoing components. It can be seen that there are no measured downgoing arrivals in Figure 2.5a which is to be expected given that downgoing waves from a virtual source at the image point would have to be reflected back upward in order to be recorded at the surface; there are no interfaces below the image point in Figure 2.5a (as shown by the reflector locations in Figure 2.2) so no such reflection can occur. By contrast the image point in Figure 2.5b lies between reflectors and therefore both the downgoing and upgoing signals contain arrivals.

Marchenko methods are only able to construct events that follow ray paths for which the energy was recorded in the original reflectivity (R). Therefore in the examples presented in Figure 2.5 we have only plotted the estimated Green's function to a maximum time of $1.4s$. This equates to times preceding the recording time of the reflectivity (R) minus the travel time of the direct arrival (T_d). This shows that it is important to have sufficiently long recording times for Marchenko methods to be effective.

So far we have discussed a simple, one-dimensional example which demonstrates

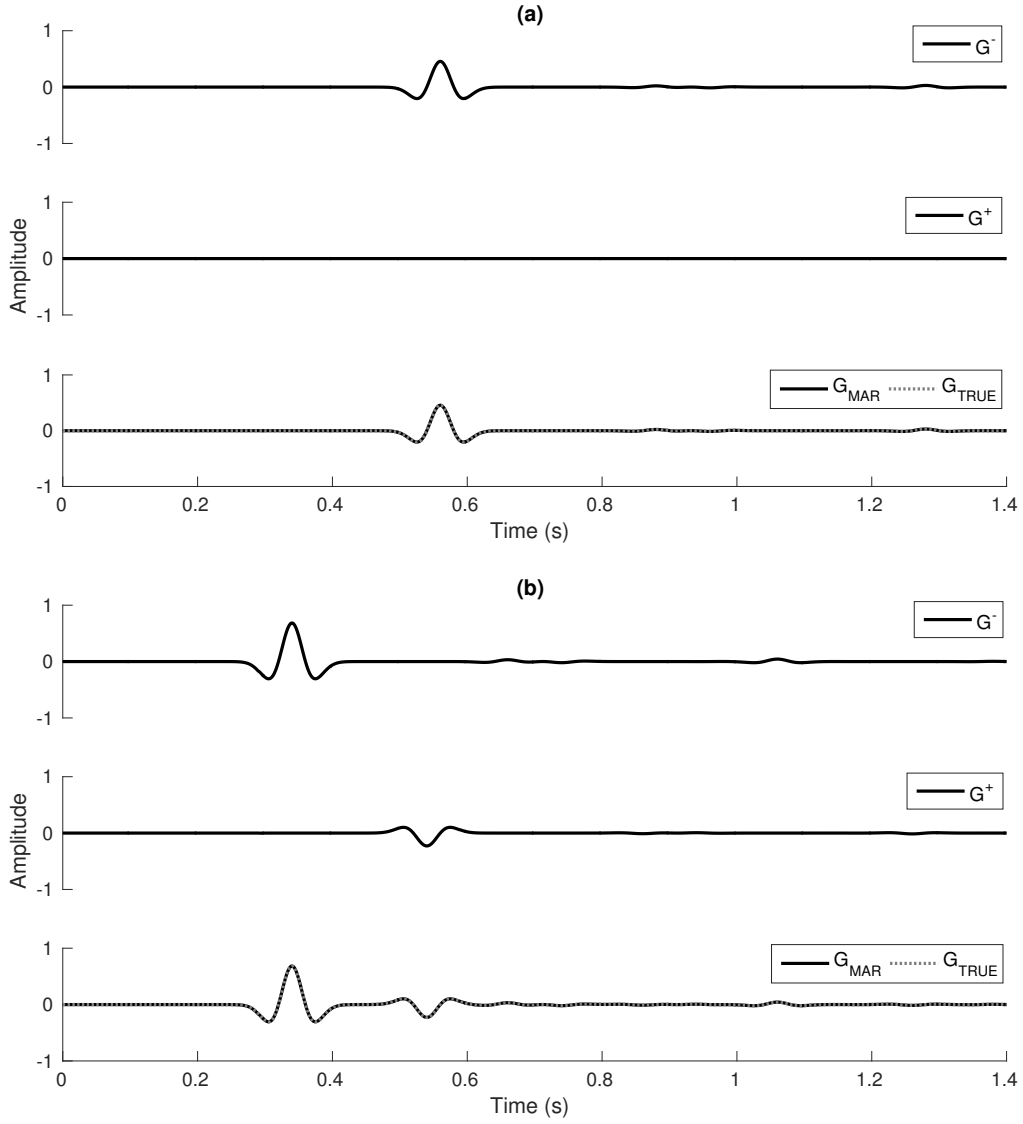

Figure 2.5: Estimated Green's functions from two subsurface image points. Figure (a) is for an image point at 1400m; Figure (b) is for an image point at 850m. Panels 3 and 6 (counting from the top downwards) compare Marchenko and true Green's functions. Panels 1, 2, 4 and 5 show the upgoing and downgoing decomposition of the corresponding total Green's function.

the methodology clearly and in which the solutions are essentially perfect. The next section extends the examples to higher dimensions, where the results are more prone to errors.

2.3 Marchenko Methods in Higher Dimensions

The example above illustrated for one-dimensional problems that all of the information required to determine Green's functions between a subsurface image point and the surface is contained within just two signals, $R(x_0, x_0, t)$ and $T_d(x_i, x_0, t)$. In two dimensions this is not the case as the reflectivity from one surface source ($\mathbf{x}_0'$) is measured by multiple receivers ($\mathbf{x}_0$). It is worth noting that our notation must now change to account for the extra spatial coordinate where $\mathbf{x} = (x_1, x_2)$. Nevertheless, in two or three dimensions concepts similar to those in Figures 2.3 and 2.4 hold. Indeed while for one-dimensional problems those diagrams have axes of depth and time, they apply with similar geometries (but incorrect angles of transmission and reflection) to two-dimensional problems if the horizontal time axis is replaced with the horizontal space axis. Each arrival in the desired Green's function at any particular angle is constructed by the interference of other specific arrivals at other particular receiver and source combinations in the reflectivity.

Rather than requiring that we selected specific arrivals to convolve in order to construct each arrival in the Green's function, Marchenko methods sum (integrate) over all possible sources along the acquisition array (boundary) and rely on destructive interference to cancel out unwanted energy. A similar cancellation occurs in reverse time migration (Kaelin and Guitton, 2006) and in seismic interferometry (van Manen *et al.*, 2005, 2006; Wapenaar and Fokkema, 2006). This only works accurately in two dimensions if the reflectivity is of the correct form, and in practise this means that a vertical spatial derivative (often

called a dipole) source or receiver needs to be created or measured. In the two-dimensional examples presented in this chapter the reflectivity is from a pressure (monopole) source measured by a vertical particle velocity (dipole) receiver.

In the previous section we introduced a set of formulae to estimate Green's functions using Marchenko methods. These formulae are extended to two dimensions by changing the one-dimensional convolutions to multi-dimensional convolutions and integrating across all sources on the acquisition boundary (we denote this boundary as $\partial\mathbb{D}_0$). For example the two-dimensional versions of equations 2.1 and 2.2 for source redatuming are:

$$G^{+}(\mathbf{x}_0, \mathbf{x}_i, t) = \int_{\partial\mathbb{D}_0} f^{+}(\mathbf{x}_0', \mathbf{x}_i, t) \otimes R(\mathbf{x}_0, \mathbf{x}_0', t)\, d\mathbf{x}_0' - f^{-}(\mathbf{x}_0, \mathbf{x}_i, t) \tag{2.8}$$

$$G^{-}(\mathbf{x}_0, \mathbf{x}_i, t) = f^{+}(\mathbf{x}_0, \mathbf{x}_i, -t) - \int_{\partial\mathbb{D}_0} R(\mathbf{x}_0, \mathbf{x}_0', t) \otimes f^{-}(\mathbf{x}_0', \mathbf{x}_i, -t)\, d\mathbf{x}_0' \tag{2.9}$$

To implement equations 2.8 and 2.9 the focusing functions need to be available between the focusing location and both the surface sources and receivers (e.g. $f^{+}(\mathbf{x}_0, \mathbf{x}_i, t)$ and $f^{+}(\mathbf{x}_0', \mathbf{x}_i, t)$). In practice the two-dimensional formulation of these functions requires interchangeability between the two. We therefore impose the condition that the source array and receiver array are co-located $\mathbf{x}_0' = \mathbf{x}_0$.

A further consideration for implementation of the two-dimensional Marchenko method is the direct arrival estimate (T_d) and windowing function (θ) which now need to be estimated in two dimensions as they were above in one dimension. These functions are now calculated between a single focusing location and multiple surface sources/receivers. This increases the complexity of these functions

and the potential for errors in estimating them; nevertheless if this is done following the same workflow as one-dimensional Marchenko methods the relationships discussed in the previous sections still hold.

2.3.1 Green's Function Estimation in Two Dimensions

In the following two-dimensional example, the source wavelet in the reflectivity is not the same as that in the focusing functions. We use the $20Hz$ Ricker wavelet shown in Figure 2.6b for the focusing function, whereas we use a flat spectrum wavelet shown in Figure 2.6a as the source wavelet for our reflectivity. The flat spectrum wavelet is defined in the frequency domain so as to have an amplitude of 1 over the range of frequencies of interest (the frequencies contained within the Ricker wavelet) as demonstrated in Figure 2.6c. Using this formulation removes the need for deconvolution as it ensures that the frequency content of the updated focusing functions does not change between iterations of the Marchenko method (in each iteration they are simply multiplied by a source wavelet that does not change the shape of the current wavelet within the frequency band of interest (Thorbecke *et al.*, 2017)).

Figure 2.7 shows a subsurface model that is used to demonstrate two-dimensional Marchenko methods. This subsurface model has both variable density and velocity. There are 188 symmetrically spread sources and receivers co-located at 16 meter intervals along the surface of the model ($depth = 0$). A point is also marked in the subsurface, $\mathbf{x}_i = (1000m, 800m)$ which identifies a chosen image point for Marchenko Green's function calculation.

Two models have been used to create the two input datasets required for the Marchenko method. The reflectivity from surface sources measured at the surface receivers and excluding free surface multiples has been created using the true model given in Figure 2.7a. This represents surface seismic reflection data after

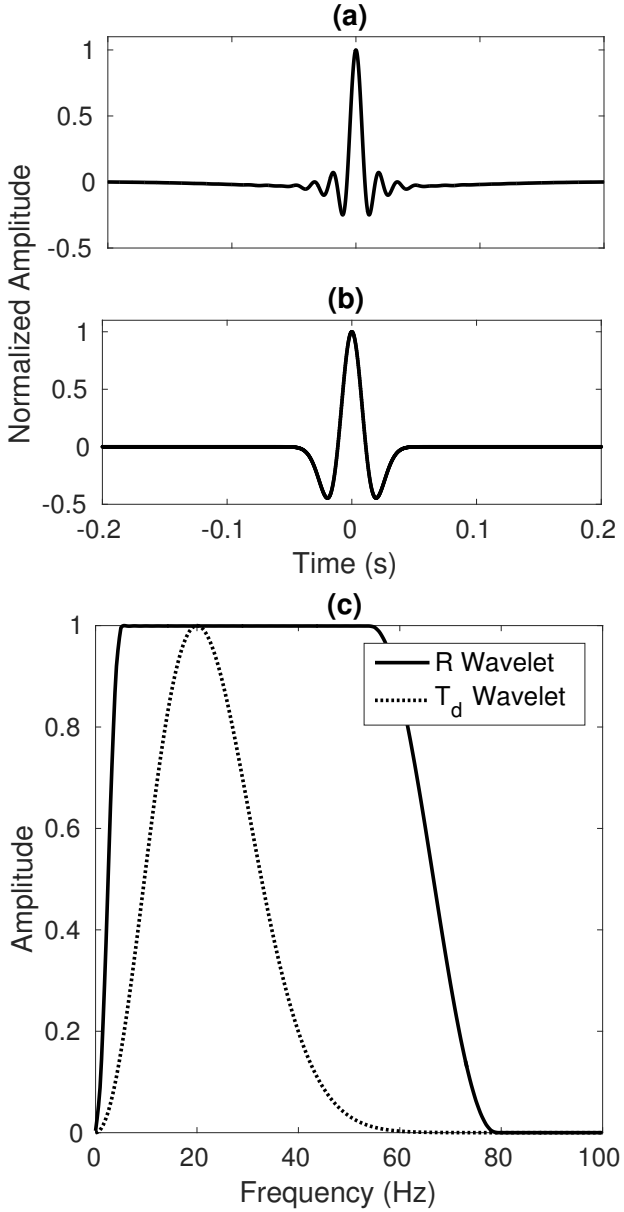

Figure 2.6: Wavelets used in two-dimensional finite-difference modelling. Panels (a) and (b) show zero phase, time domain plots of the reflectivity and direct arrival wavelets respectively, and panel (c) compares the amplitude of the frequency spectra of the two wavelets. The reflectivity and direct arrival are shown as solid and dashed lines respectively.

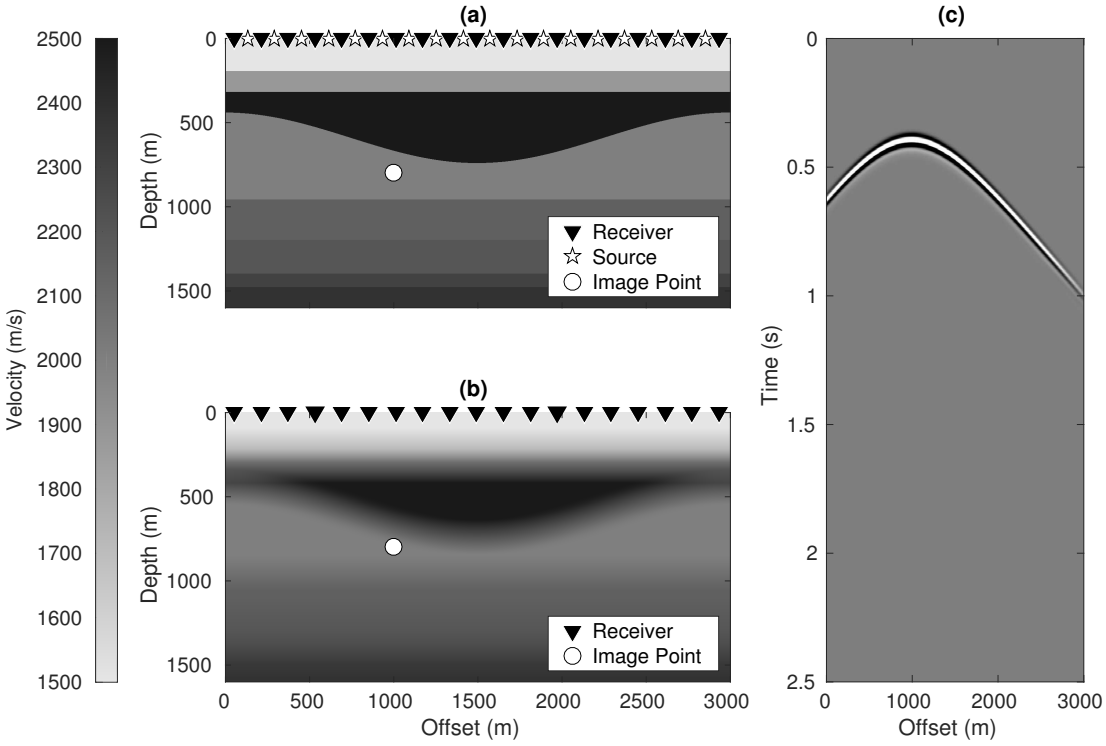

Figure 2.7: The true (a) and smoothed (b) subsurface models used for the two-dimensional synthetic example. The subsurface model has a variable velocity (shown) and a proportionate variable density model (densities lie in the range $1000kg/m^3 - 5000kg/m^3$). The surface is spanned by 188 co-located sources and receivers represented by stars and triangles (with every tenth source and receiver plotted). The white circle in (b) marks a chosen subsurface image point at location $\mathbf{x}_i$. Panel (c) shows an estimate of the direct arrival between the image point and the surface as calculated through the smooth model in panel (b).

free-surface multiples have been removed. An estimate of the direct arrival between the surface and the image point has been created using the smooth model in Figure 2.7b. In practice we do not have access to the true model, hence we have used a smoothed version of the true model for our direct arrival calculations, assuming that in practise some initial or reference velocity model will be available. The direct arrival signal can be modelled with finite-difference solvers (Figure 2.7c), or approximated using eikonal solvers to find the travel time at which a scaled source wavelet can be assumed to arrive. In this example, for accuracy, both datasets were created using finite-difference solutions to the acoustic wave equation (in Figure 2.7b a source was fired at the image point and recorded along the surface receiver array, giving Figure 2.7c). See van der Neut and Wapenaar (2016) for an alternative solution to solving the Marchenko method if an estimated velocity model is not available.

By iterating the two-dimensional form of equations 2.1-2.7 (Wapenaar *et al.*, 2014) the focusing functions and Green's functions are obtained, and the final Green's function estimates are shown in Figure 2.8b. For simplicity we have not included every component of the estimated Marchenko Green's function (e.g. focusing functions) - for these we refer readers to the accompanying code package within which these figures are included.

To test the accuracy of the Marchenko solution, the calculated Green's functions in Figure 2.8b are plotted beside the true solutions in Figure 2.8a. The latter panel shows a solution computed in the true model in Figure 2.7a by firing a source at the image point. The estimated signal shows a good match, with negligible errors visible. The errors that are present can be attributed to limited boundary coverage by the acquisition array, errors in the finite difference solution, and windowing artifacts.

In Figure 2.8 all of the amplitudes have been scaled to values between 1 and

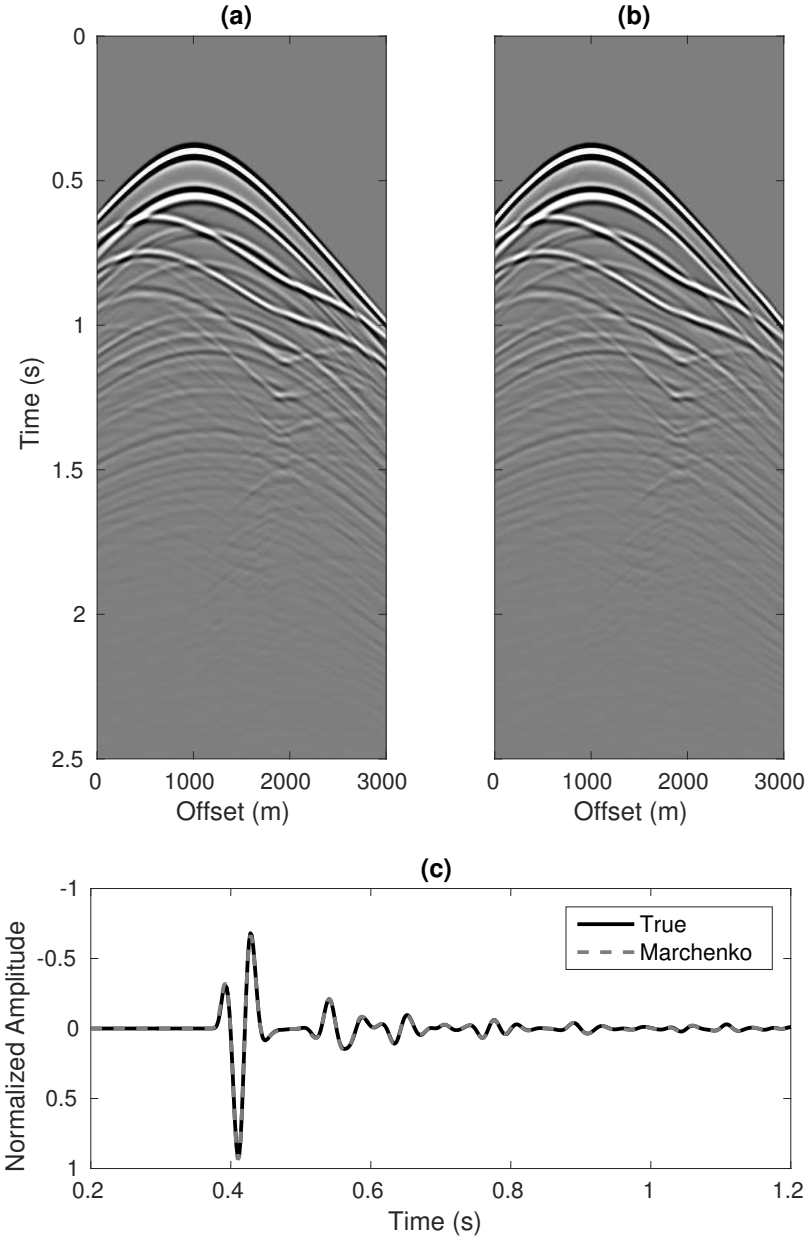

Figure 2.8: A comparison of Green's functions from image point $\mathbf{x}_i$ in Figure 2.7b. Panel (a) shows the true solution calculated through the true model in Figure 2.7a using finite difference methods. Panel (b) shows the Marchenko solution calculated using the methods discussed in the main text. Panel (c) compares trace number 51 (offset=$804m$) taken from panels (a) and (b).

-1. This has been done for comparison purposes, as the Marchenko methods implemented in this chapter cannot estimate true absolute amplitudes of Green's functions. The primary reason for this is that the direct arrival was approximated at the start of the Marchenko method as $f_0^+(\mathbf{x}_0, \mathbf{x}_i, t) \approx T_d(\mathbf{x}_i, \mathbf{x}_0, -t)$: we do not know the amplitude of the true inverse, so it is impossible to estimate a Marchenko solution with the true absolute amplitude as the initial focusing function estimate is implicit in the final solution – see equation 2.5.

2.4 Marchenko Code Package

Accompanying this chapter is a set of well-commented MATLAB codes for two-dimensional Green's function estimation. The first of these (*CODE_1*) is the code used to create Figure 2.8 and running it without edits should produce a version of that figure. For this code the inputs are pre-computed and the variables already set, below we discuss the operation of this. However, because that code is inflexible (the image point is fixed) we have included a second code for user experimentation which we introduce at the end of this section. By choosing an appropriate set-up, users should be able to use the second code to reproduce similar outputs of the first – a good exercise for learning and teaching purposes.

2.4.1 Data

Four datasets accompany this MATLAB code, as summarised in Table 1. All of these datasets are stored in the time domain, although for computational efficiency most of the code operations are performed in the frequency domain.

The direct arrival, windowing function and true signals are all common shot gathers from a source at the image point with identical dimensions: $i = 2001$ and $j = 188$, where i is the number of time samples and j is the number of surface

Dataset	**Description**
ICCR_marchenko_R.mat	The modelled reflectivity: the acquisition boundary is at the top surface ($depth = 0m$) of the model defined in Figure 2.7a.
ICCR_marchenko_TD.mat	The modelled direct arrival: the signal with a source at the image point and the receivers on the acquisition boundary as shown in Figure 2.7b.
ICCR_marchenko_theta.mat	A filter designed using the direct arrival *ICCR_marchenko_TD.mat*, which mutes the signal at times greater than or equal to the direct arrival.
ICCR_marchenko_GT.mat	The modelled true solution for comparison: a real source is located at the image point and receivers are on the acquisition boundary in Figure 2.7a.

Table 2.1: Description of the datasets used as inputs to the MATLAB code *ICCR_marchenko.m*.

receivers. In this example the sampling interval was $0.002s$ and the recording time was from $-2s$ to $2s$. The fourth dataset is the reflectivity which has an extra dimension k to account for multiple shot locations, with $i = 2001$, $j = 188$ and $k = 188$.

2.4.2 Codes

The code called *ICCR_marchenko.m*, follows the same workflow introduced earlier in this paper. Algorithm 1 shows the corresponding pseudocode. The equations referred to in Algorithm 1 are the one-dimensional versions given herein, but the code uses the equivalent two-dimensional versions given in Wapenaar *et al.* (2014). We have not defined a measure of convergence within this code; instead a desired number of iterations is input by the operator, the default being 5.

Algorithm 1 Marchenko Green's Function Estimation Pseudocode

load R, T_d and θ
calculate f_0^+ and f_0^- using equations 2.3 and 2.4
for n iterations (k=1,2,..,n) **do**
  calculate M_k^+ using equation 2.6
  calculate f_k^- using equation 2.7
end for
calculate f_k^+ using equation 2.5
calculate G^+ and G^- using equations 2.1 and 2.2 (or 2.8 and 2.9)
return G^+ and G^-

One additional feature in the MATLAB code has not been discussed above: a spatial taper is applied during each summation (integration) of sources along the acquisition boundary. Its purpose is to account for the limited acquisition coverage: it ensures cancellation of edge effects from the extremities of the acquisition array, as these would otherwise create spurious energy in the solutions (if the boundary was infinite, as assumed in two- or three-dimensional Marchenko

theory, this would not be required). The taper takes a half cosine shape at either end of the array and the number of points to be tapered at either end of the array can be varied by the user (the default is 20% of the number of receivers).

A second code in the accompanying package (*CODE_2*), operates using the same fundamentals as the code introduced above, but has been implemented as matrix multiplications for computational efficiency and changed to allow alternative virtual source locations to be used. To the latter end the direct arrival and window are no longer pre-computed. Instead we have included a function that computes these using an eikonal solution (*ICCR_marchenko_eik.mat*). The input seismic data remains the same but there is no longer a true solution available for comparison. This code is set up so the input data can be changed; to do this a measured or calculated reflectivity dataset in the correct form will be required as well as an eikonal solution through an estimated velocity model.

2.5 Marchenko Imaging

Marchenko imaging creates images of the subsurface using the estimated Green's functions. This works in a similar way to conventional imaging algorithms such as reverse time migration (RTM), in the sense that the similarity of two signals is tested by the use of an imaging condition (Claerbout, 1971), and the result is used to identify subsurface inhomogeneities.

Marchenko imaging should in theory be able to be used to calculate more accurate images than standard methods as we have access to more accurate Green's functions $G^{+/-}$ which account for multiply reflected waves. The imaging condition applied for our implementation of Marchenko imaging is a (zero-lag) cross-correlation between the downgoing Green's function G^{+} and the direct arrival estimate T_d as proposed by da Costa Filho *et al.* (2015):

$$I_{MI}(\mathbf{x}_i) = \sum_{\mathbf{x}_0} \sum_{t} T_d(\mathbf{x}_i, \mathbf{x}_0, t)\, G^{+}(\mathbf{x_0}, \mathbf{x}_i, t) \tag{2.10}$$

For comparison purposes we have also implemented an alternative imaging condition to approximate standard methods:

$$I_{RTM}(\mathbf{x}_i) = \sum_{\mathbf{x}_0} \sum_{t} T_d(\mathbf{x}_i, \mathbf{x}_0, t)\, G_0^{+}(\mathbf{x_0}, \mathbf{x}_i, t) \tag{2.11}$$

where $G_0^+ \approx R \otimes T_d^*$, which is equivalent to a back-propagated wavefield used in RTM methods – see da Costa Filho and Curtis (2016) for further details.

The two signals in equations 2.10 and 2.11 should be most similar when the image point $\mathbf{x}_i$ is on a reflector, so the cross-correlation will produce maxima at those points. We note that as with conventional RTM there are several alternative imaging conditions that could be applied. Comparisons and discussion of these is beyond the scope of this chapter but more detail is given in da Costa Filho *et al.* (2015) and Singh and Snieder (2017b).

We imaged the model in Figure 2.7a using equations 2.10 and 2.11, with results shown in Figure 2.9. Image points were selected on a four meter grid inside the imaged area. Directionally decomposed Green's functions were calculated at each of these points. The only difference between these Green's functions and those calculated in Figure 2.8 is in the direct arrival input, which here was constructed by placing a source wavelet at the travel time calculated using an eikonal solver, rather than calculating T_d using finite difference methods; this saves on computational cost since eikonal solvers require relatively few operations compared to finite-difference methods. This example therefore also illustrates that this approximate method of modelling the direct field can be sufficient for

some imaging applications.

The image calculated using equation 2.10 at each image point is shown in Figure 2.9a. All interfaces in the subsurface are identified with few artifacts in the solution, despite the presence of internal multiples in the surface acquisition data that is input to the Marchenko method. The clarity of the image is mainly due to the accuracy of the Green's function estimates G^+ which are calculated by Marchenko methods and used by equation 2.10. For comparison the solution in Figure 2.9b is calculated using equation 2.11 with the approximate G_0^+ shows clear artifacts due to internal multiples.

We have included a final code (*CODE_3*) in the software package which can be used to implement Marchenko imaging using the methods discussed above. There is an increased computational cost associated with implementing this because a Green's function now needs to be calculated at each and every imaging point. Inside the code the image can be target-orientated by defining the image point spacing and a limited or targeted subsurface location.

2.6 Discussion

The aim of this tutorial is to provide beginners to Marchenko methods with an accessible way to understand the topic, and to allow them to begin to experiment with the methods on synthetic examples using easily understandable and editable MATLAB code. Marchenko methods as introduced in this paper use surface seismic data and an estimate of the subsurface velocities to estimate Green's functions between a subsurface image point and the surface. These estimated signals have a steadily increasing number of applications, including subsurface imaging and seismic redatuming, but also for removing multiples (Meles *et al.*, 2014), constructing primaries (Meles *et al.*, 2016) and calculating Green's function

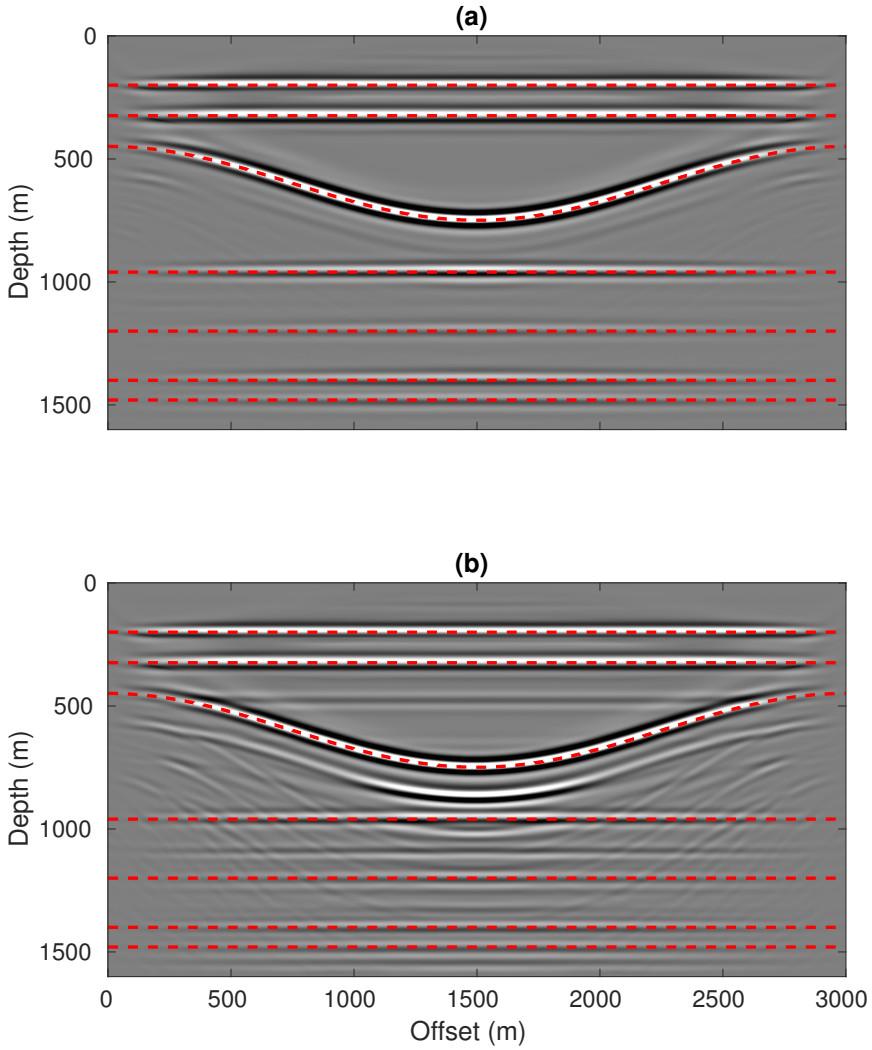

Figure 2.9: The Marchenko (a) and reverse time migration (b) images for the subsurface models defined in Figure 2.7a and 2.7b. A Green's functions has been estimated every 4 meters and the imaging condition used for each of the images is defined in equations 2.10 and 2.11 respectively. The dashed red lines represent the true subsurface heterogeneities.

where both the source and receiver are inside the subsurface (Wapenaar *et al.*, 2016; Singh and Snieder, 2017a). Marchenko methods also have applications outside of seismology, for example for imaging using ground penetrating radar (Slob *et al.*, 2014a) or for medical imaging (van der Neut *et al.*, 2017).

The results are promising, and offer a data-driven method that improves on current imaging methods, in particular by correctly predicting the arrival of multiply reflected waves at image points. Given the novelty of these methods there are still aspects that are poorly understood – areas of ongoing research. They include exploring how to apply Marchenko in real, dissipative media with seismic attenuation, the effects on Green's function estimates of velocity model errors and corresponding poor estimates of direct arrivals (both in time and amplitude), the effect of various types of noise in the reflectivity field, and the cost and effort of scaling two-dimensional Marchenko methods to three dimensions.

The accompanying MATLAB codes for the estimation of acoustic Green's functions using two-dimensional Marchenko methods, also comes with an accompanying dataset which can be used to reconstruct Figure 2.8. The codes can easily be adapted for users to include their own datasets. The data will need to be formatted correctly, the details for which are discussed in the earlier sections of this tutorial and in comments within the code. Datasets of a similar simplicity should achieve similarly positive results. Extending these methods to more realistic datasets and examples is an active area of research, and with the accompanying code readers have the tools to contribute to this.

2.7 Conclusion

In this chapter we have introduced Marchenko methods, a set of novel, data-driven techniques that can be applied to seismic redatuming and imaging problems.

We have shown these methods can accurately estimate directionally decomposed Green's functions from virtual subsurface source locations to surface receiver locations in both one and two dimensions, and this includes the multiply-scattered components of the Green's functions. However, all of the methods we have presented are based on synthetic seismic datasets; extending these methods to more realistic datasets and examples is an area of active research, and with the accompanying MATLAB code readers have the tools to contribute to this.

2.8 Acknowledgments

The authors would like to thank Petrobras and Shell for their sponsorship of the International Centre for Carbonate Reservoirs (ICCR), and for permission to publish this work from the VSP project. We would also like to thank fellow members of the ICCR and members of the Edinburgh Interferometry Project (EIP) for their numerous fruitful discussions. Finally, we would like to thank Jan Thorbecke, Johan Robertsson, two anonymous reviewers and the Associate Editor Jonas D. De Basabe for their comments which helped improve this chapter. The data used within this chapter was generated with the Madagascar open-source software package freely available from **www.ahay.org**.

Chapter 3

Marchenko Methods in a Three-dimensional World

Angus Lomas[1] **and Andrew Curtis**[1,2]

In this chapter we investigate the implications of moving from two-dimensional Marchenko methods (introduced in the preceding chapter) to three dimensions. Whilst the theory for applying Marchenko methods to three-dimensional media holds as it did in two dimensions, prior to completing the work within this chapter their application had been limited to two-dimensional media.Therefore we investigate the effects of three-dimensional wavefields, structures and data on the results of two- and three-dimensional Marchenko methods.

3.1 Introduction

The aim of seismic imaging is to produce maps indicative of spatial variations in

[1]School of GeoSciences, University of Edinburgh, Edinburgh, UK
[2]Institute of Geophysics, ETH Zurich, Zurich, Switzerland

properties of the Earth's subsurface. Methods of seismic imaging, such as Reverse Time Migration (RTM – Baysal *et al.* (1983)) typically use seismograms recorded on or near the surface of the Earth and assume that seismic reflections observed in these seismograms are singly-scattered, meaning that they have reflected or diffracted only once from subsurface heterogeneities (the so-called Born approximation). This assumption is imposed within such methods by the use of a low-wavenumber, smoothly varying estimate of the subsurface seismic velocity, to extrapolate surface seismic data into the subsurface. Extrapolating the injected source wavefield estimates what the wavefield looked like before it scattered, and back-extrapolating the wavefield recorded at the surface estimates the subsurface wavefield after it scattered (both operations being called redatuming). These wavefield are combined to form an image of any scattering heterogeneity that converted the source wavefield into the receiver wavefield. However, the extrapolated wavefields and hence the images are generally in error since in reality some parts of the wavefield scattered multiple times from the omitted high wavenumber velocity variations as they propagate through the subsurface.

Marchenko methods overcome the single scattering assumption by extrapolating wavefields into the subsurface including all multiply-scattered waves, even when only a smoothly varying estimate of the subsurface velocity structure is available (Broggini *et al.*, 2012; Wapenaar *et al.*, 2013). Images created using these wavefields and a variety of imaging conditions exhibit a reduction in the artifacts that usually contaminate seismic images due to multiples (da Costa Filho *et al.*, 2015; da Costa Filho and Curtis, 2016; Singh and Snieder, 2017b).

Following the development of Marchenko methods (Marchenko, 1955; Rose, 2001; Broggini *et al.*, 2012) their application was initially limited to synthetic acoustic seismic imaging and redatuming problems without allowing for free-surface reflections (Wapenaar *et al.*, 2013). Further developments have extended Marchenko methods to elastic media (da Costa Filho *et al.*, 2014, 2015; Wapenaar,

2014) and to seismic data containing free surface multiples (Singh *et al.*, 2015, 2016). More recently Marchenko methods have been applied to real, reservoir scale, seismic datasets (Ravasi *et al.*, 2016; Jia *et al.*, 2017; Staring *et al.*, 2018) and to real ultrasonic (non-destructive testing) data (Wapenaar *et al.*, 2018; Cui *et al.*, 2018a; da Costa Filho *et al.*, 2018). However, given the novelty of these methods there are still aspects that are poorly understood. One of these, and the focus of this article, is the behavior of Marchenko methods when applied to three-dimensional seismic wavefields, structures and data.

Marchenko methods are based on mathematical derivations by Wapenaar *et al.* (2013) that all assume three spatial dimensions, but only recently have Marchenko methods been applied to so-called three-dimensional seismic data (Lomas and Curtis, 2017). The prospect of applying Marchenko methods in three dimensions was discussed in earlier work (Wapenaar *et al.*, 2014), however concerns were raised about the practicalities of the spatially dense acquisition geometries that would be required for the input reflectivity. This is because similarly to seismic interferometry (Snieder, 2004a; Curtis *et al.*, 2006) and RTM (Baysal *et al.*, 1983), Marchenko methods rely on destructive and constructive interference of seismograms from neighbouring source and receivers in order to produce the seismograms of interest. Recorded waveforms can only accurately interact with adjacent signals if they are recorded with a source or receiver spacing that is a fraction of the seismic wavelength (van Manen *et al.*, 2005, 2006; Wapenaar and Fokkema, 2006), hence the concern.

In this chapter we first show that Marchenko methods hold in three dimensions when seismic data collected with sufficient boundary coverage in both horizontal directions are available. However, given issues with the practicality of acquiring such data we also assess the performance of Marchenko methods on data acquired along a linear surface seismic array above a three-dimensional (3D) Earth. We show that simply sub-sampling the full areal three-dimensional wavefield along

this line and applying the same Marchenko methods produces a redatumed wavefield that contains phase inconsistencies which produce depth errors in subsurface images. These can be removed by the application of correction factors within the Marchenko workflow to account for inconsistencies in dimensionality. Finally we demonstrate the impact of out-of-plane reflections on Marchenko estimates using data from linear seismic arrays. We show that these can be detrimental to the redatumed seismograms and the resulting images. These errors do not exist when using seismic data from full areal arrays.

3.2 Marchenko Methods

3.2.1 Theory

The theoretical foundations of Marchenko methods are the one-way reciprocity theorems of the convolution and correlation type for pressure-normalized wavefields (Wapenaar and Grimbergen, 1996; Wapenaar *et al.*, 2014):

$$-\int_{\partial\mathbb{D}_0} \rho^{-1}\left[p_A^+(\partial_z p_B^-) + p_A^-(\partial_z p_B^+)\right]\ d^2\mathbf{x}_0 = \int_{\partial\mathbb{D}_i} \rho^{-1}\left[(\partial_z p_A^+)p_B^- + (\partial_z p_A^-)p_B^+\right]\ d^2\mathbf{x}_i \tag{3.1}$$

$$-\int_{\partial\mathbb{D}_0} \rho^{-1}\left[p_A^{+*}(\partial_z p_B^+) + p_A^{-*}(\partial_z p_B^-)\right]\ d^2\mathbf{x}_0 = \int_{\partial\mathbb{D}_i} \rho^{-1}\left[(\partial_z p_A^+)^* p_B^+ + (\partial_z p_A^-)^* p_B^-\right]\ d^2\mathbf{x}_i \tag{3.2}$$

Equations 3.1 and 3.2 are the three-dimensional acoustic reciprocity theorems given in the frequency domain. Two states are represented by A and B, and

these represent directionally decomposed $(+/-)$ wavefields (p) traveling through two different media (or subsurface models) chosen to be those described in Figure 3.1. These wavefields are decomposed to represent either the component propagating downwards $(+)$ or upwards $(-)$ at the recording location, therefore no horizontally-propagating waves are accounted for within current Marchenko theory. Equations 3.1 and 3.2 describe the relationship between the measured wavefields in these two different media. We define state A to be a so-called focusing state, in which the wavefield injected at the surface would focus to create a spatio-temporal impulse at location $\mathbf{x}_i' = (x, y, i)$ at time defined to be $t = 0$. Thereafter this impulsive energy will diverge like a source placed at $\mathbf{x}_i'$. In order for this to be possible the medium is defined to be equal to the true Earth's acoustic structure above, and to be reflection-free below the horizontal subsurface boundary $\partial\mathbb{D}_i$; this defines the so-called reference medium. State B is the true medium within which the true Green's functions between the surface source/receiver array at locations $\mathbf{x}_0''/\mathbf{x}_0$ (on the horizontal surface boundary $\partial\mathbb{D}_0$) and the subsurface point $\mathbf{x}_i'$ exist, and these are ultimately the wavefields of interest. We define Green's functions (G) as the pressure recordings measured at a receiver location due to the firing of a spatio-temporally impulsive source at $t = 0$: G therefore depends on source and receiver locations and on frequency or time. Additionally $\mathbf{x}_0$ represents an array of points with a fixed depth coordinate $z = 0$ and a variable horizontal coordinate at an array of locations which vary in both the first (x) and second (y) horizontal dimension: $\mathbf{x}_0 = \{(x_j, y_j, 0) : j = 1, 2, \ldots, N\}$, where N is the number of surface source/receiver positions. For the implementation presented here $\mathbf{x}_0$ has to equal $\mathbf{x}_0''$ and $\mathbf{x}_i'$ represents a point on the boundary $\partial\mathbb{D}_i$.

Given the relationships described in Figure 3.1 we can assign values to the wavefields of interest in equations 3.1 and 3.2. In state B quantity $p_B^{+/-}$ is a Green's function created by a source at location $\mathbf{x}_0''$ and measured on the boundary

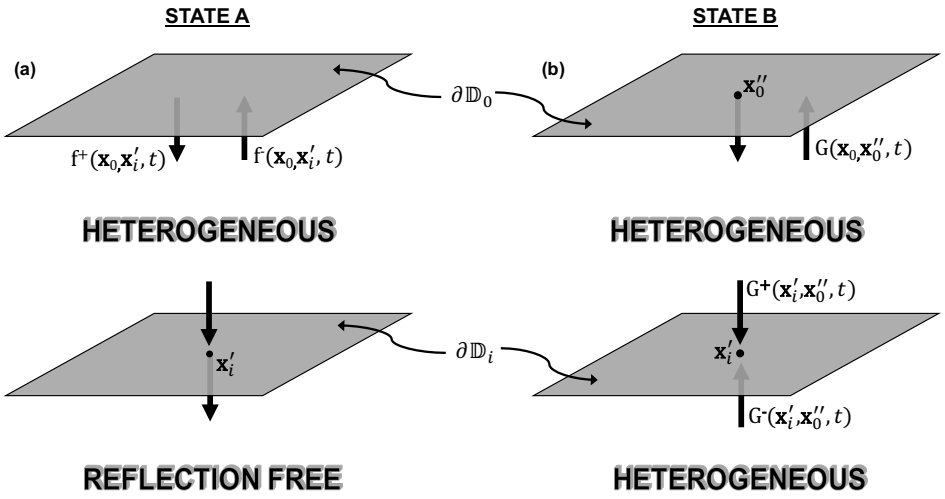

Figure 3.1: A three-dimensional diagrammatic comparison of the differences between states A and B, described in equations 3.1 and 3.2. Panel (a) shows state A (the reference medium) which is equal to the true medium above constant depth boundary $\partial\mathbb{D}_i$, and is reflection free below $\partial\mathbb{D}_i$ where $\mathbf{x}_i'$ is the focusing location and is a point on the boundary $\partial\mathbb{D}_i$. Panel (b) is the true medium, which is identical to state A above the surface $\partial\mathbb{D}_i$ but also includes the true medium heterogeneity below this depth.

represented by the integral ($\partial\mathbb{D}_{0/i}$). In state A, quantity $p_A^{+/-}$ is a focusing function (denoted $f^{+/-}$ below). We define a downgoing focusing function f^+ as a set of signals that when injected at a boundary as a source time function would collapse to a singular peak in the pressure field at the focusing location; the upgoing focusing function f^- is the reflected component (in State A) of the downing focusing funcion recorded at the injection surface. In state A we define the focusing location as a point $\mathbf{x}_i'$ on the boundary $\partial\mathbb{D}_i$. This focus is created by injecting a source time function at the boundary represented by the integral ($\partial\mathbb{D}_{0/i}$). Hence the values are defined as $p_A^{+/-} = f^{+/-}(\mathbf{x}_0/\mathbf{x}_i, \mathbf{x}_i', \omega)$ and $p_B^{+/-} = G^{+/-}(\mathbf{x}_0/\mathbf{x}_i, \mathbf{x}_0'', \omega)$. We assume free-surface multiples have been removed from the data so that the upper (ground surface) boundary $\partial\mathbb{D}_0$ is effectively absorbing. Furthermore, state A is reflection free below the boundary $\partial\mathbb{D}_i$. These two conditions allow us to simplify equations 3.1 and 3.2 when we substitute in the wavefields defined above – this is formally derived in appendix A of Wapenaar *et al.* (2014), and fully expanded this gives:

$$G^-(x_i', y_i', i; x'', y'', 0; \omega) = \iint_{\partial\mathbb{D}_0} [R(x'', y'', 0; x, y, 0; \omega) f^+(x, y, 0; x_i', y_i', i; \omega)] dx\ dy - f^-(x'', y'', 0; x_i', y_i', i; \omega) \tag{3.3}$$

$$G^+(x_i', y_i', i; x'', y'', 0; \omega) = f^+(x'', y'', 0; x_i', y_i', i; \omega)^* - \iint_{\partial\mathbb{D}_0} [R(x'', y'', 0; x, y, 0; \omega) f^-(x, y, 0; x_i', y_i', i; \omega)^*] dx\ dy \tag{3.4}$$

Equations 3.3 and 3.4 are the three-dimensional equivalent of equations 11 and 12 presented by Wapenaar *et al.* (2014) (as well as most of the literature on this topic), therefore for convenience we will revert back to standard notation from this point forward, where $\mathbf{x}_i' = (x_i', y_i', i)$, $\mathbf{x}_0 = (x, y, 0)$ and $\mathbf{x}_0'' = (x'', y'', 0)$. Equations 3.3 and 3.4 define a relationship in three dimensions between the focusing functions (f) and the Green's functions (G) of interest. These are linked by the reflectivity (R) which is the measured upward propagating wavefield in the true medium created by a volume injection rate impulsive source, and is the vertical (z) particle velocity component measured by receivers where both the sources and receivers are on the boundary $\partial\mathbb{D}_0$ (Wapenaar and Fokkema, 2006), multiplied by a scaling factor of -2 (Thorbecke *et al.*, 2017).

The aim of the Marchenko method is to calculate the Green's functions. However, the only known quantity in equations 3.3 and 3.4 is the measured reflectivity. Therefore, to solve for G^+ and G^- we require a method that enables an estimate of the focusing functions to be obtained. An elegant algorithmic way to solve this problem is first described by Slob *et al.* (2014b) and Wapenaar *et al.* (2014), discussions of the mathematical foundation of the algorithm are described by van der Neut *et al.* (2015b), and an intuitive demonstration of how this method works is given by van der Neut *et al.* (2015d), Cui *et al.* (2018b) and Lomas and Curtis (2019). The algorithm is an iterative procedure which requires as input both an estimate of the reflectivity (R), and an estimate of the direct arrival between the chosen virtual receiver (location $\mathbf{x}_i'$) and the surface sources (denoted T_d). The algorithm is embodied within equations 3.5-3.8 below, and upon convergence the solutions for $f^{+/-}$ can be used as input to equations 3.3 and 3.4:

$$f_0^-(\mathbf{x}_0'', \mathbf{x}_i', \omega) \approx \theta \int_{\partial\mathbb{D}_0} [R(\mathbf{x}_0'', \mathbf{x}_0, \omega) T_d(\mathbf{x}_0, \mathbf{x}_i', \omega)^*] \, d^2\mathbf{x}_0 \tag{3.5}$$

$$M_n^+(\mathbf{x}_0'', \mathbf{x}_i', \omega)^* = \theta \int\limits_{\partial \mathbb{D}_0} \left[R(\mathbf{x}_0'', \mathbf{x}_0, \omega) f_{n-1}^-(\mathbf{x}_0, \mathbf{x}_i', \omega)^* \right] d^2\mathbf{x}_0 \tag{3.6}$$

$$f_n^-(\mathbf{x}_0'', \mathbf{x}_i', \omega) = f_0^-(\mathbf{x}_0'', \mathbf{x}_i', \omega) + \theta \int\limits_{\partial \mathbb{D}_0} \left[R(\mathbf{x}_0'', \mathbf{x}_0, \omega) M_n^+(\mathbf{x}_0, \mathbf{x}_i', \omega) \right] d^2\mathbf{x}_0 \tag{3.7}$$

$$f_n^+(\mathbf{x}_0'', \mathbf{x}_i', \omega) \approx T_d(\mathbf{x}_i', \mathbf{x}_0'', \omega)^* + M_n^+(\mathbf{x}_0'', \mathbf{x}_i', \omega) \tag{3.8}$$

In equation 3.5, the complex conjugate (*) of the estimated direct arrival (T_d) in the frequency domain (ω) is convolved with the reflectivity (a multiplication in the frequency domain). The result is multiplied by a window $\theta(\mathbf{x}_0'', \mathbf{x}_i', t)$ in the time domain which filters out data that does not contribute to the focusing functions. The operator θ is therefore defined as a transform from the frequency to the time domain, a multiplication by window θ and then a transfer from the time to the frequency domain. The time window component of this operation is defined as:

$$\theta(\mathbf{x}_0'', \mathbf{x}_i', t) = \begin{cases} 0 & t \leq -t_d(\mathbf{x}_0'', \mathbf{x}_i') \\ 1 & -t_d(\mathbf{x}_0'', \mathbf{x}_i') < t < t_d(\mathbf{x}_0'', \mathbf{x}_i') \\ 0 & t \geq t_d(\mathbf{x}_0'', \mathbf{x}_i') \end{cases} \tag{3.9}$$

where t_d is the travel time between its two arguments ($\mathbf{x}_0''$ and $\mathbf{x}_i'$). The initial estimate for f_0^- is then used to begin a procedure that iterates equations 3.6 and 3.7. These two equations are repeated for n iterations, until convergence, upon which equation 3.7 produces a value for the upgoing focusing function f^- and equation 3.6 produces a value for the coda (scattered component) of the

downgoing focusing function M_n^+. The final step consists of solving for f_n^+ by summing T_d and M_n^+ (equation 3.8).

Equations 3.3-3.8 are the three-dimensional form of the two-dimensional equations implemented in existing applications of the Marchenko method. The only difference between the two forms is the acquisition boundary which has changed from a line in two-dimensional applications to a surface integral in three-dimensional applications, and consequently an extra dimension is added to all coordinates.

3.2.2 Dimensionality of Seismic Data

There are two main factors to consider when working with three-dimensional rather than two-dimensional wavefields. The first is the difference between measured responses to waves propagating through two and three-dimensional media. The second is the data acquisition array, given that the Marchenko method ideally needs full boundary coverage (to infinite offsets) in both horizontal spatial dimensions to perform integrals in the equations above.

First consider the measured seismic response for a wavefield propagating through a lossless three-dimensional medium. In this case a source signal will propagate outwards from the injection point in all directions (x, y, z) distributing the initial energy over an increasingly large wavefront as it propagates. This change in energy is a function of the distance any packet of energy on the wavefield has travelled $r = |\mathbf{x}_i' - \mathbf{x}_0''|$. In three dimensions this energy change is proportional to the surface area of a sphere, hence the amplitude change is a function of $1/r$ (since amplitude is proportional to the square root of the energy). In two dimensions the same intuition applies but the energy is only distributed over a two-dimensional wavefront (x, z) so amplitude change is instead a function of $1/\sqrt{r}$. Furthermore, differences in phase, and an additional frequency dependent

difference in amplitude occur between two and three dimensions. These various differences can be expressed mathematically within the expressions for the two-dimensional and three-dimensional Green's functions for a homogeneous medium as (Snieder, 2004b; Galetti *et al.*, 2013; Auer *et al.*, 2013):

$$G^{2D}(r,k) \approx \frac{1}{2\sqrt{2\pi kr}} \exp\left(ikr + \frac{i\pi}{4}\right) \tag{3.10}$$

$$G^{3D}(r,k) = \frac{1}{4\pi r} \exp\left(ikr\right) \tag{3.11}$$

Equations 3.10 and 3.11 are expressed in the frequency domain. However, for simplicity of notation we have expressed the solutions in terms of angular wavenumber k, which is a function of angular frequency (ω) and the velocity (c) of the medium ($k = \frac{\omega}{c}$). It is worth noting that the two-dimensional Green's function (G^{2D}) given in equation 3.10 is an approximate solution which is valid in the far-field of the source. This approximation only holds if the distance r is significantly greater than the wavelength ($r > \lambda$).

Given the formulae in equations 3.10 and 3.11 we can use simple algebra to calculate an approximate function that transforms data from waves propagating in a first dimensionality into the equivalent data that would have been obtained if the waves had propagated in the other dimensionality:

$$G^{2D}(r,k) \approx G^{3D}(r,k)\sqrt{\frac{2\pi r}{k}}\exp\left(\frac{i\pi}{4}\right) \tag{3.12}$$

$$G^{3D}(r,k) \approx G^{2D}(r,k)\sqrt{\frac{k}{2\pi r}}\exp\left(-\frac{i\pi}{4}\right) \tag{3.13}$$

Implementing the filters in equations 3.12 and 3.13 is not straightforward in variable velocity media because the ray-path r is generally unknown. Implementation is therefore often approximated (Auer *et al.*, 2013) or r can be estimated using ray theory (Bleistein, 1986). In this chapter this problem has been avoided by using a known constant velocity medium but we acknowledge that in further work in variable-velocity media a more robust algorithm will be required and there will be errors associated with our implementation.

In Figure 3.2 we have modelled wave propagation using staggered-grid finite difference methods through a two-dimensional and a three-dimensional medium (G_{TRUE}). The measured responses for a set of source-receiver pairs at an offset of $750m$ are plotted in black in Figure 3.2a and 3.2b. In this example the injected wavelet is the temporal derivative of a $15Hz$ Ricker wavelet. Each of these two signals is then transformed to the other dimensionality to test the accuracy of the transfer functions given in equations 3.12 and 3.13, with results given by the dashed red lines in Figure 3.2a and 3.2b.

Figure 3.2 confirms, perhaps counter intuitively that the response to a Ricker wavelet source in two dimensions is more complex than it is in three dimensions, undergoing a phase shift which offsets the zero-crossing from the predicted arrival time (marked by a black cross). The comparisons after transferring between the two forms of Green's function are a good match even though this is not an

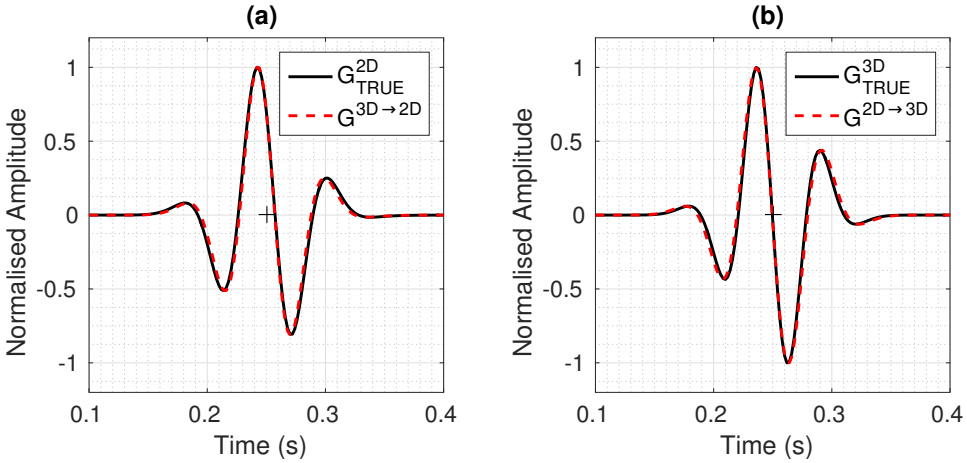

Figure 3.2: A comparison of the modelled responses following the injection of a 15Hz Ricker derivative wavelet inside a homogeneous medium ($c = 3000m/s$). Panels (a) and (b) compare the signals that are measured at the receiver in two and three dimensions respectively in repose to a source of $750m$ offset. A second comparison in panels (a) and (b) show the modelled three-dimensional Green's function converted to the equivalent two-dimensional Green's function (panel a) and the modelled two-dimensional Green's function converted to the equivalent thee-dimensional Green's function (panel b).

exact solution given the approximation made in equation 3.10 and errors in the finite difference wave propagation. These transforms will therefore be used in the remainder of this article.

It is important to consider these differences when implementing the Marchenko method in three dimensions. All real data from seismic waveforms originates from three-dimensional wave propagation, however it is very common for seismic surveys to sample these wavefields only in two dimensions (e.g. seismic streamers use approximately linear spatial arrays plus time). In equations 3.12 and 3.13 we provide a method to transfer between dimensions but we still need to consider the implications of limited acquisition aperture. This is not problematic with limited aperture data providing that the subsurface contains near-horizontal subsurface structures and tapering at far offsets in both horizontal axes. However, this means when steep dips are present in the subsurface the accuracy of the results

of Marchenko methods may be compromised.

3.3 Experimental Setup

The seismic data examples presented in this chapter are based on a single synthetic dataset, created by modelling acoustic seismic wave propagation through a three-dimensional subsurface model. The model has variable density but a constant velocity ($3000m/s$) in order to make straight ray based interpretations of the various packets of energy. It contains a three-dimensional trough structure and multiple horizontal planar layers (see Figure 3.3). Although this model is simple it was designed to optimise compute times due to its symmetries about vertical planes, to easily separate events observed in the seismic wavefield and to enable simple analysis of the results, yet to contain sufficient three-dimensional structure to illuminate features of interest.

The seismic data from each impulsive source at location $\mathbf{x}_0$ to all receivers at locations $\mathbf{x}_0''$ are used as an approximation to the three-dimensional reflectivity $R(\mathbf{x}_0'', \mathbf{x}_0, t)$, measured using an areal grid of sources and receivers on the model ground surface ($z = 0$). Sources and receivers are co-located at $32m$ intervals in both directions giving a total of 5922 locations (Figure 3.3b). This spacing was chosen to reduce the computational cost of Marchenko receiver redatuming but ensure accurate solutions were obtained. The source wavelet for the reflectivity is a constant-amplitude frequency spectrum wavelet with a bandwidth of $0 - 45Hz$, so designed to remove the need for source-signature deconvolution that would otherwise be required in order to estimate R, thus eliminating a potential source of error (Thorbecke *et al.*, 2017). A second $15Hz$ Ricker derivative wavelet, is used to calculate the direct arrival (equation 3.5); as this is then convolved with the reflectivity, which has a flat frequency spectrum, this is the 'effective' injected wavelet that will be contained within our Marchenko Green's function estimates

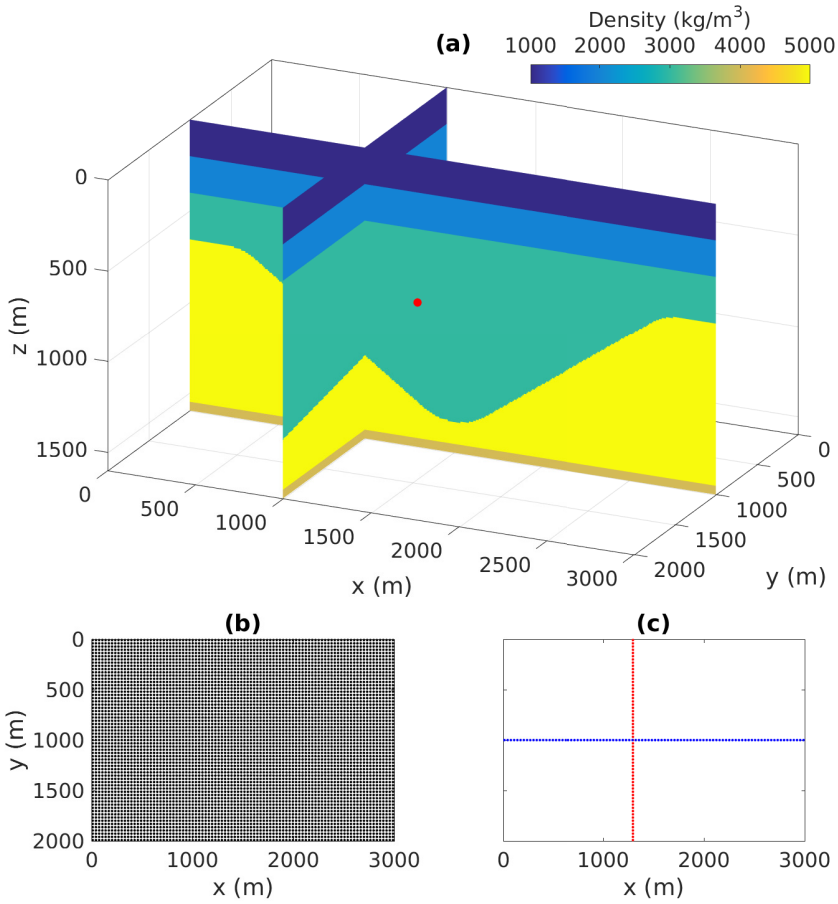

Figure 3.3: The three-dimensional variable density, constant velocity ($3000m/s$) model used to created synthetic seismic data. In panel (a) we compare two slices through the model ($x = 1004m$ and $y = 1000m$). The red sphere defines a subsurface virtual receiver position $\mathbf{x}_i'$ at location at $(1292m, 1000m, 600m)$. Panels (b) and (c) show the areal and linear acquisition geometries used in later sections of this article: each dot is both a source and receiver location. The linear arrays in panel (c) are at $x = 1292m$ and $y = 1000m$.

and in this example this was modelled to reduce errors in the estimated Green's function. We produced seismic data using the parameters described above, with each of the 5922 source positions measured by all 5922 receivers – a total of 35,070,084 seismic traces. Each of these traces has a recording length of $2s$ and a temporal sampling interval of $0.002s$. These data form the reflectivity R used as input to the three dimensional Marchenko algorithm (equations 3.3-3.8).

In the later sections of this chapter we consider the implications of sub-sampling the three-dimensional seismic data along spatially linear source and receiver arrays shown in Figure 3.3c. The reflectivity for the linear arrays contains just 8836 traces (blue profile) and 3969 traces (red profile).

3.4 Three-dimensional Green's Function Estimation

We can use the seismic dataset and the virtual receiver position defined in Figure 3.3 as input to the three-dimensional Marchenko algorithm defined in equations 3.3-3.8. First, five iterations of equations 3.5-3.8 are used to estimate the focusing functions f_n^+ and f_n^- which are shown in Figure 3.4a and 3.4b respectively. Then we solve for the directionally decomposed Green's functions $G^{+/-}$ using equations 3.3 and 3.4 and sum the result to obtain the full Green's function $G = G^+ + G^-$. This result can be compared to the true modelled Green's function as displayed in Figure 3.4d.

Qualitative analysis of Figure 3.4 suggests a good match between the true and estimated Green's functions. A second test of the solution accuracy is given in Figure 3.5a where we make a trace by trace comparison of the calculated three-dimensional Marchenko estimate and the modelled Green's function (recorded along a 2D profile). The results demonstrate the applicability of Marchenko

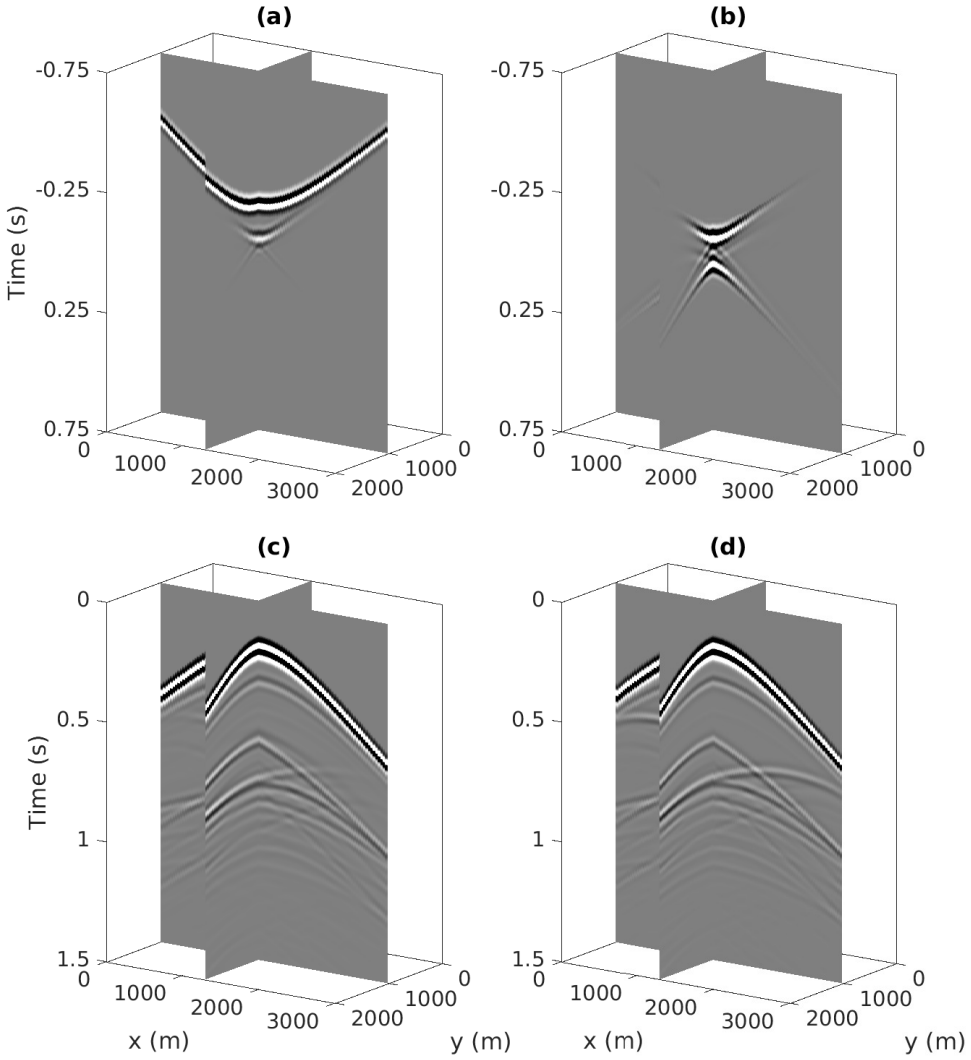

Figure 3.4: Three-dimensional focusing functions, common virtual receiver gathers estimated using the Marchenko method, and directly modelled Green's functions. Panels (a) and (b) respectively show the estimated solutions for the focusing functions f_n^+ and f_n^- obtained from equations 3.5-3.8. These functions are used to estimate the Green's functions $G = G^+ + G^-$ where $G^{+/-}$ are estimated from equations 3.3 and 3.4, and G is displayed in panel (c). This can be compared to the directly modelled Green's functions in panel (d).

methods to three-dimensional wavefields and structures. There are some small discrepancies in Green's function components at far offsets due to the wavefields interacting with the steeply dipping trough structure (see Figure 3.3). The poorer estimation of these components is due to the limited source and receiver aperture of the seismic array (the errors increase as aperture is decreased) and hence could be improved by including additional sources and receivers beyond the extremities of the current experiment. This limitation is not unique to this method and is also known to cause inaccuracies in conventional imaging algorithms like RTM.

A consideration for all implementations of Marchenko methods is how to scale the amplitude of the reflectivity. Marchenko methods will only iterate to accurate solutions when the amplitude of the true reflectivity is known. This problem is often overcome in synthetic experiments by using perfectly scaled wave propagation codes but in our experiment, as is the case with real seismic data, the reflectivity is not scaled correctly. We therefore implement a method for calculating a scaling factor (which is then multiplied by the reflectivity) using the '*j-curve*' analysis presented by van der Neut *et al.* (2015c). This method provides a solution that can be implemented regardless of the dimensionality of the seismic data, and therefore reduces systematic and subjective errors in the comparisons we make in the following sections.

3.5 Green's Function Estimation with a 2D-Seismic Profile

All previous applications of Marchenko methods in geophysics (using both synthetic and real data) have used seismic datasets collected along a spatially linear acquisition geometry. This is a reasonable avenue of study as it is common to acquire seismic data along a line of sources and receivers where only one of the horizontal coordinates varies. However, with the exception of real data

applications, these studies have also been limited to two-dimensional media. In this section we investigate Marchenko solutions when the acquisition geometry is linear but wave propagation is three-dimensional. The differences in the measured seismic responses are of the type defined in equations 3.10 and 3.11 and illustrated in Figure 3.2.

To test the impact of these differences we extract a linear-array data subset from the areal survey measured over the three-dimensional model given in Figure 3.3a, taken along the line $y = 1000m$ (see Figure 3.3c). This provides a reflectivity profile collected with a constant y coordinate but with three-dimensional wave propagation and therefore three-dimensional Green's functions. This line was selected as it contains minimal out-of-plane reflections (we discuss the implications of those in more detail in the following section). We apply the two-dimensional equivalents of equations 3.3-3.8 (Wapenaar *et al.*, 2014) to this subsampled dataset to calculate an estimate of the Green's functions between the surface sources and the same virtual receiver position as in the previous three-dimensional examples. We compare the solutions for two- and three-dimensional Marchenko methods applied to three-dimensional wavefields, as shown in Figure 3.5b and 3.5a respectively.

The results in Figure 3.5b show successful calculation of the Green's functions. However the trace comparison highlights that there is a mismatch in phase between some components of the calculated and true solutions. This mismatch does not appear in the equivalent three-dimensional solution given in Figure 3.5a. It can therefore be assumed that the errors observed are due to the differences in acquisition geometries which impose the constraint that the two-dimensional Marchenko methods can not integrate over the second horizontal spatial dimension. A solution to overcome this problem is to apply a transform to the seismic data measured along a linear array but propagating in three-dimensions, to convert it into the two-dimensional equivalent data by implementing equation

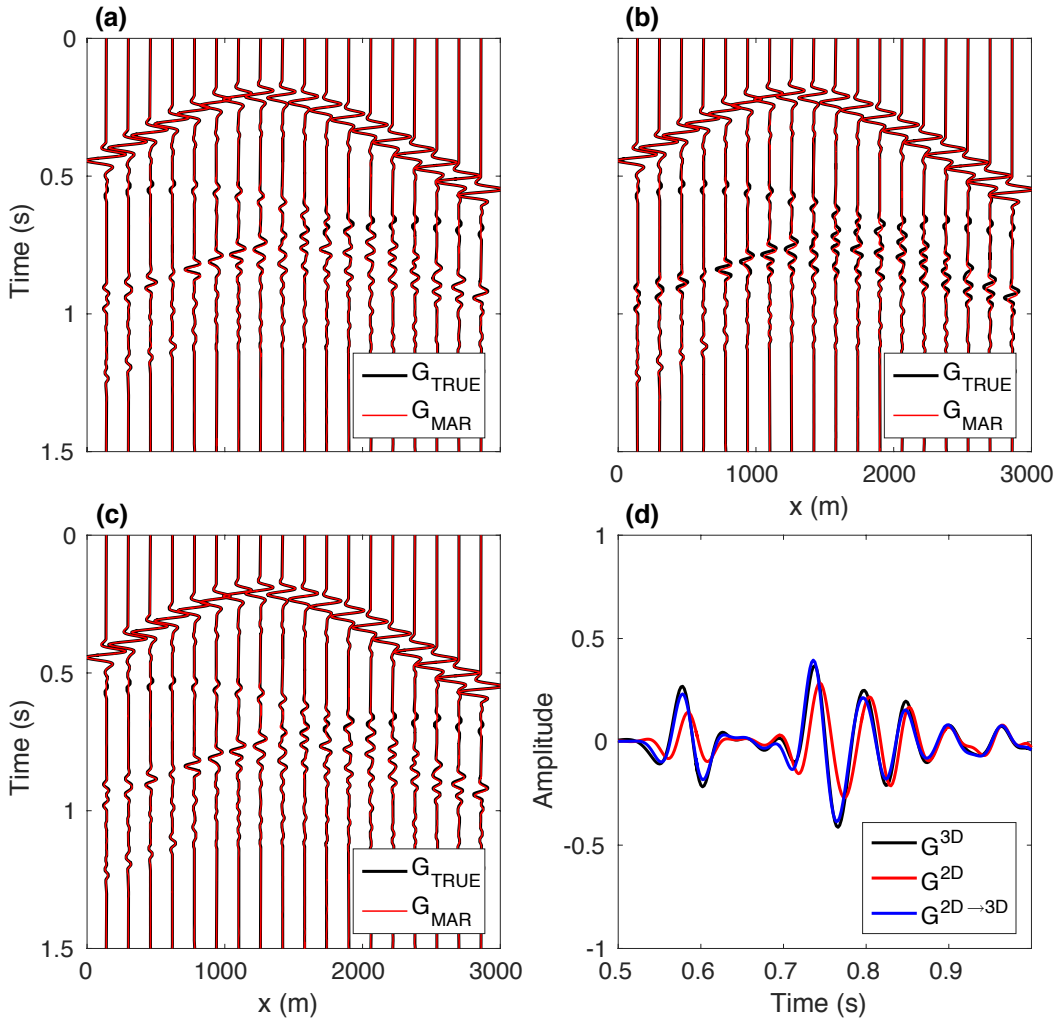

Figure 3.5: A comparison of the estimated Marchenko common receiver gathers (red) compared to the modelled receiver gathers (black). Panel (a) shows the fully three-dimensional Marchenko estimate, panel (b) shows the two-dimensional Marchenko estimate for waves propagating in three-dimensions, and panel (c) shows the dimensionally corrected two-dimensional Marchenko estimate. Panel (d) compares a single trace for each Marchenko estimate from source position $(1292m, 1000m, 0m)$. For display purposes a time dependent gain has been applied to all panels.

3.12. This modified dataset can then be used as input into the two-dimensional Marchenko scheme. The Marchenko solution is then approximately equivalent to one propagating in two dimensions. For purposes of comparing it to the full three-dimensional solution it must therefore first be transferred back into its three-dimensional equivalent using equation 3.13. The final estimate is displayed in Figure 3.5c.

Figure 3.5a shows the fully three-dimensional solution and can be viewed as a reference solution – the best result that can be achieved if three-dimensional seismic data is available over a dense areal array. The result in Figure 3.5b uses a, sub-sampled version of the three-dimensional data that is only recorded along a linear-array, thus forcing two-dimensional Marchenko methods to be applied which in turn produce a solution that contains phase errors. If we calculate the l_2-norm of the data misfit between the true and Marchenko result for both the reference solution and the result in Figure 3.5b it increases by 60% in the latter case. If we compare the l_2-norm of the data misfit between the reference solution and the dimensionally corrected result, shown in Figure 3.5c (which uses the same input data as Figure 3.5b), there is only a 4% increase in the latter case. We have therefore demonstrated how to accurately retrieve Marchenko solutions with three-dimensional wavefields when using two-dimensional seismic data: the data first needs to undergo dimensionality corrections. This method appears to be accurate in the case that there are minimal out-of-plane reflections in the data employed.

3.5.1 Out-Of-Plane Reflections

A significant motivation to use seismic data from areal arrays is their ability to discriminate reflections that occur outwith the vertical plane beneath any linear array and thus allow us to map three-dimensional geological structures accurately.

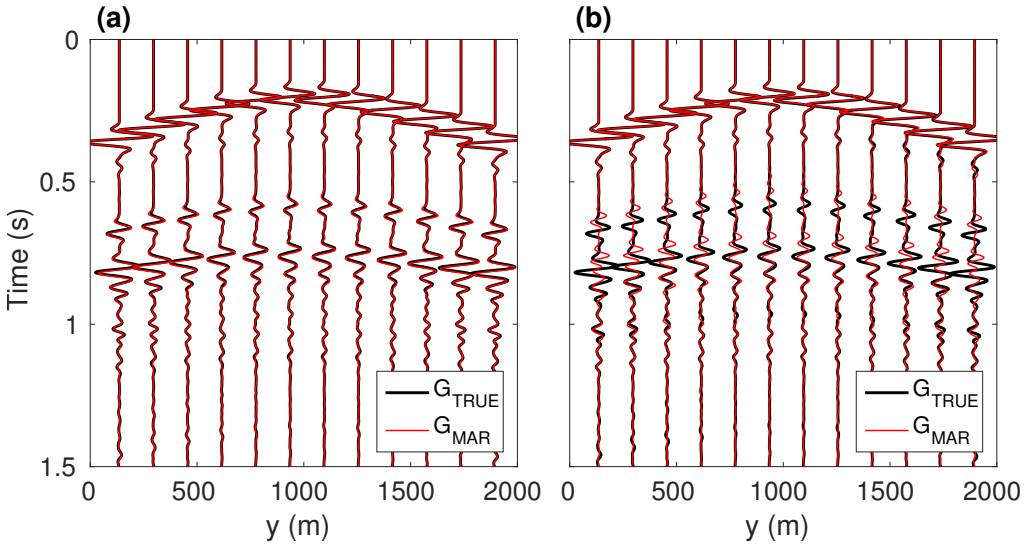

Figure 3.6: A comparison of two virtual receiver gathers constructed using Marchenko methods from seismic data recorded on a full areal array and a linear array where the data contain out-of-plane reflections. Panel (a) shows the gather constructed using the full areal survey. Panel (b) shows the gather constructed using only a seismic data subset from a linear array that contains out-of-plane reflections. In both panels the subsurface virtual receiver position is at $(1292m, 1000m, 600m)$ as shown in Figure 3.3a, and both the two-dimensional profile displayed and the data subset used in panel (b) have a constant x coordinate of $1292m$ (Figure 3.3c).

In this section we investigate the implications of seismic data containing out-of-plane reflections on the solutions to the two- and three-dimensional Marchenko method.

Consider a linear seismic array with a constant x coordinate of $1292m$ (Figure 3.3c) that is perpendicular to the line in the previous section. We use this dimensionally-corrected data as input to the two-dimensional Marchenko method with results displayed in Figure 3.6b. For comparison we also use the data from the full areal array to construct the same virtual receiver gather with results shown in Figure 3.6a.

The results in Figure 3.6 show that with a linear array spanning only part

of the top boundary, the Marchenko method is not able to process out-of-plane reflections correctly. The final virtual receiver gather estimates are therefore inaccurate. However, when three-dimensional data is used for the same reconstruction the results are accurate.

3.6 Multi-dimensional Marchenko Imaging

One of the reasons Marchenko methods are of particular interest to Geophysicists is because of their applications in subsurface imaging. The Marchenko Green's functions estimates from equations 3.3 and 3.4 can be used to produce seismic images with reduced multiple related contamination (Behura *et al.*, 2014). Marchenko imaging operates similarly to other imaging algorithms such as RTM, by applying imaging conditions to the estimated subsurface wavefields to identify where seismic waves reflect. In this article, as an example we use a cross-correlation imaging condition in which we calculate the zero-lag correlation coefficient of the upgoing Green's function (G^-) and the direct arrival estimate (T_d) at every desired image point $\mathbf{x}_i'$ to form the image I (Claerbout, 1971; da Costa Filho *et al.*, 2015):

$$I(\mathbf{x}_i') = \int\limits_{\partial\mathbb{D}_0} d\mathbf{x}_0'' \int\limits_{-\infty}^{\infty} [G^-(\mathbf{x}_i', \mathbf{x}_0'', \omega) T_d(\mathbf{x}_i', \mathbf{x}_0'', \omega)^*] \, d\omega \tag{3.14}$$

This imaging condition essentially measures the similarity of the two input signals. We therefore rely on these two signals being similar when and only when the virtual receiver (image point) is on a subsurface interface, as would be the case if the downgoing direct-wave in T_d had caused the upgoing Green's functions G^- by reflection. However, given that the data we are using is frequency band-limited we expect reflectors to be identified within approximately half a wavelength of the true subsurface interface location. There are alternative imaging conditions that

can be applied in Marchenko imaging which include deconvolution (Singh and Snieder, 2017b), multi-dimensional deconvolution (van der Neut *et al.*, 2011) and imaging conditions that combine Marchenko imaging with reverse time migration at relatively little extra cost (da Costa Filho and Curtis, 2016). Equation 3.14 was chosen here because it is robust, cheap to compute, it has been shown to provide clean images in two-dimensional applications, and hence is a common choice amongst practitioners.

Applying equation 3.14 to the redatumed Greens functions shown in Figure 3.5 and 3.6 gives four Marchenko images shown in Figure 3.7 each of which is based on data taken from the same three-dimensional wavefields. The results in Figures 3.7b and 3.7c, which use the data from Figure 3.3b and the blue line from Figure 3.3c respectively, identify all subsurface interfaces. The true locations of the interfaces are shown in Figure 3.7a. The input data for all of these images has undergone no pre-processing to remove internal multiples. Despite this there is limited evidence of false reflectors due to peg-leg multiples, which would be observed at $\sim 600m$ if RTM was deployed for example. However, there are differences between the images presented in Figure 3.7. The first and most significant is the error in interface depth imaging. To highlight this effect we picked the peak amplitude (which corresponds to the interface location) of the signal in each image and compare them in Figure 3.7a. This shows that the phase errors observed in Figure 3.5b manifest themselves as depth errors of $16m$ in the Marchenko image presented in Figure 3.7c. We have already demonstrated the accuracy of our dimensionality correction which would enable us to construct results similar to Figure 3.7b with two-dimensional data. In Figure 3.7a we have identified the true location of the subsurface interface within a margin of error of $\pm 8m$, where the residual uncertainty corresponds to the image point spacing. In Figures 3.7e and 3.7f we image an area of the subsurface perpendicular to the images in Figure 3.7b and 3.7c using the data from Figure 3.3b and the red

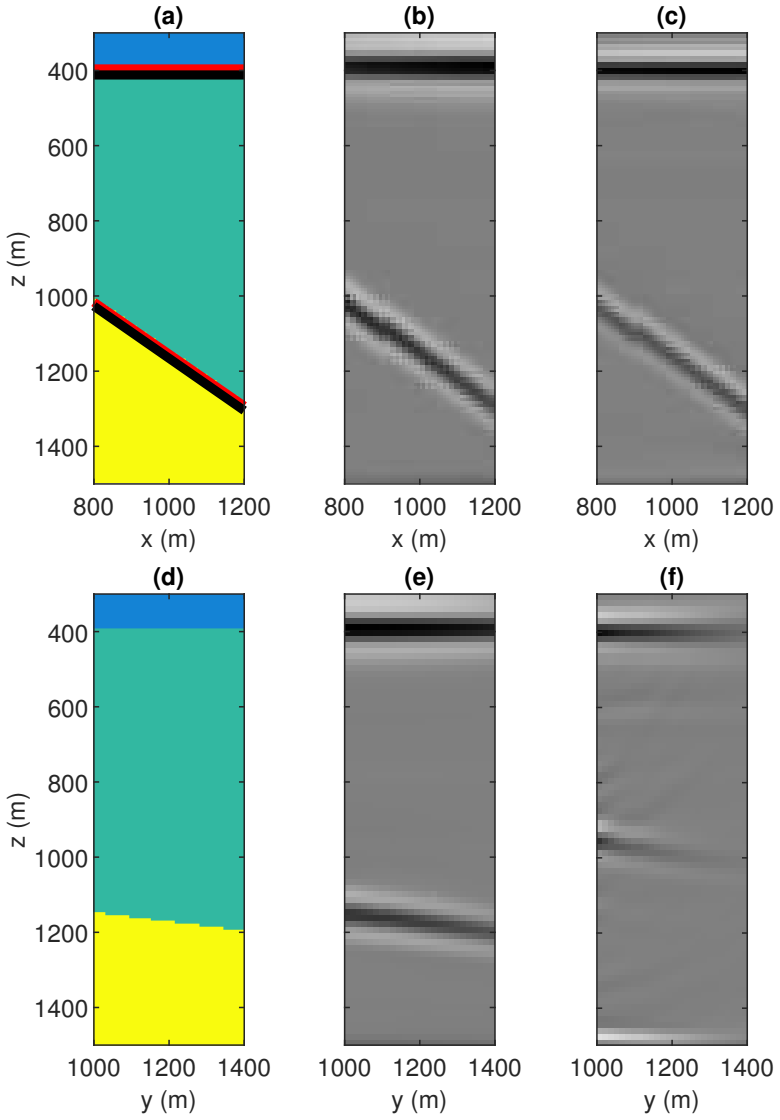

Figure 3.7: Panel (a) shows a two-dimensional slice ($y = 1000m$) taken from the three-dimensional model in Figure 3.3a. Panel (b) is the three-dimensional Marchenko image created using the areal survey shown in Figure 3.3b. Panel (c) is a two-dimensional Marchenko image created using a seismic dataset recorded on a linear array (the blue line in Figure 3.3c) without dimensionality corrections. The red line in panel (a) corresponds to the peak amplitude in panel (b), likewise the black line corresponds to the peak amplitude in panel (c). Panel (d) shows a second two dimensional slice ($x = 1000$), perpendicular to the line shown in panel (a). Panel (e) shows the three-dimensional Marchenko imaging result and panel (f) the two-dimensional Marchenko imaging result using the dataset recorded on a linear array (the red line in Figure 3.3c).

line from Figure 3.3c. Again, using the full three-dimensional seismic data we are able to obtain accurate images of the subsurface. However, when using a 2D linear array of seismic data across the strike of the subsurface structure the resulting image is inaccurate. This is to be expected given the observed primary components of the wavefield originate from features out-of plane.

3.7 Acquisition Geometries

A limitation of all Marchenko methods is the requirement for dense source and receiver sampling along boundary $\partial\mathbb{D}_0$ to calculate a result. This is particularly problematic in three dimensions given that the densely sampled area must span a surface rather than only a line. There is not a simple solution to this issue because the method we have implemented depends on constructive and destructive interference to create a result; if traces required for either are missing due to limitations in the acquisition geometry then errors will occur. Therefore, for application to more practical or cost-efficient acquisition geometries an interpolation step may be required to densify data sampled in space. However, it is not clear what impact this would have on calculated Marchenko solutions as the interpolation method would have to be able to recreate data at points where the interference is critical. It could be that these issues are resolved by alternative methods for implementing the Marchenko method. Nevertheless this raises a further question: *what spatial resolution do Marchenko methods require to iterate to a solution?*

In Figure 3.8 we have queried the relationship between the accuracy of Marchenko solutions and variable source/receiver spacing in a two-dimensional planar-layered medium (Figure 3.8a). We have defined a virtual receiver position in the subsurface of the model at point $\mathbf{x}_i' = (1500, 1200)$, and calculated the Marchenko Green's functions (G_{MAR}) to this point, comparing them with the modelled

Green's functions (G_{TRUE}). This comparison is made for a single trace between $\mathbf{x}_i'$ and a source position $(1500, 0)$ that is included within the array $\mathbf{x}_0''$. Our measure of accuracy is defined as:

$$Accuracy = \frac{1}{||G_{MAR} - G_{TRUE}||} \tag{3.15}$$

where $||.||$ denotes the l_2-norm. The relationship between source/receiver spacing and Marchenko estimate accuracy (equation 3.15) is likely to be dependent on both acquisition and subsurface properties. In Figure 3.8b we have tested the dependency on dominant apparent wavelength (λ_A), which has been implemented by changing the dominant frequency of the Ricker wavelet source. It is also likely that there is a further dependency on structural dip in the subsurface, which we have not considered in this experiment. Other factors that could effect theses result include, but are not limited to, acquisition aperture and focal point location, however these are likely to have a less significant impact. The results in Figure 3.8 confirm there is a dependency on dominant apparent wavelength, and from this graph we can extract an approximate empirical relationship for the successful application of Marchenko redatuming:

$$\Delta\mathbf{x}_0 \lessapprox \frac{\lambda_A}{4} \tag{3.16}$$

Typically for applications in seismic interferometry the Nyquist criterion is used to define the spatial sampling required for signal reconstruction (van Manen *et al.*, 2006). However, the lowest frequency components of the signal will have a negligible contribution to the reconstructed signal, hence we have instead defined our empirical relationship in terms of dominant frequency. The results in Figure 3.8 show that to retrieve accurate Marchenko solutions for

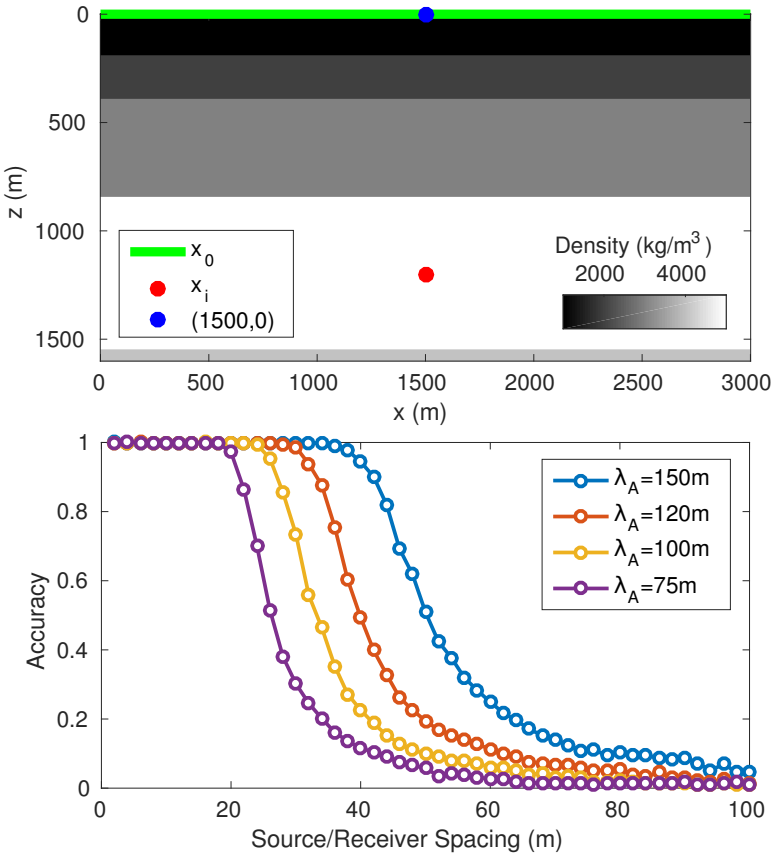

Figure 3.8: A comparison of the accuracy of estimated Marchenko Green's functions with variable source/receiver spacing. Panel (a) shows the variable density constant velocity ($1500m/s$) subsurface model, with the virtual receiver $\mathbf{x}_i'$, source array $\mathbf{x}_0''$ and the surface point $(1500, 0)$ from which the estimated Green's functions are calculated. Panel (b) compares the accuracy (equation 3.15) of Marchenko estimates with increasing receiver spacings, these are shown to have a dependence on apparent dominant wavelength (λ_A) which are represented by the variable colours.

the wavelengths tested the required source/receiver spacing can vary between maximum values of $19m-38m$. Whilst this is only a two-dimensional experiment, if similar relationships hold in three dimensions these acquisition geometries are impractically dense. The solution going forward is therefore either to use two-dimensional datasets where dense acquisition geometries are possible, and as we have shown Green's functions using the Marchenko method can be accurately estimated. However, in areas of structural complexity where three-dimensional surveys are required, the iterative Marchenko method will require an interpolation step; the accuracy and implementation of this part of the workflow warrants further research.

3.8 Discussion

3.8.1 Out-of-plane Reflections

Given that we are implementing Marchenko methods as an iterative alogithm (as apposed to RTM which is not), this raises the question: *how* do out of plane reflections cause errors in Marchenko methods? The Marchenko method for Green's functions estimation presented in equations 3.3-3.8 removes contamination due to multiples in the overburden by 'injecting' downgoing focusing functions along the top boundary $\partial\mathbb{D}_0$. These focusing functions are calculated using the travel-time and amplitude relationships present in the measured reflectivity (see van der Neut *et al.* (2015b)). The two-dimensional Marchenko method assumes that all components of the measured reflectivity are caused by features in-plane. However, the out-of-plane events still contribute to the formation of focusing functions and this means that the focusing functions will not be consistent, so the signal 'injected' at the surface will not accurately destructively interfere with the internal multiples within the seismic data. Therefore, the focusing functions will either not completely account for the internal multiples, or will add spurious multiples

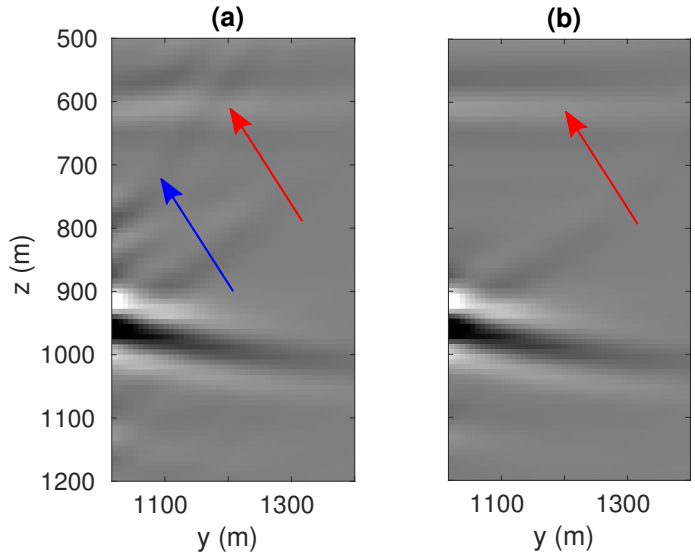

Figure 3.9: A comparison of (a) Marchenko imaging and (b) RTM imaging results created using seismic data collected along a linear seismic array (the red line in Figure 3.3c). Highlighted by the red arrows in both images is a 'false reflector' created by internal multiples in the input seismic data. The blue arrows identifies aretfects which are present only in the Marchenko imaging result. For comparison purposes the true model is given in Figure 3.7d.

into the final result, both of which would cause the focus at $\mathbf{x}_i'$ to be imperfect. This would cause the Marchenko methods to produce inaccurate Green's function estimates. To demonstrate this in Figure 3.9 we compare the imaging results from Figure 3.7f with the image obtained using the initial estimates of the focusing functions, an imaging method equivalent to RTM (da Costa Filho and Curtis, 2016).

In Figure 3.9 we have highlighted two features in the Marchenko image (Figure 3.9a) and the RTM image (Figure 3.9b). The first is the presence of a 'false' subsurface reflector indicated by the red arrow. This is present in both of the images which suggests the out of plane-reflectors are disrupting the focus and these events are not removed for the Green's function estimation. A second more concerning feature, highlighted by the blue arrow in Figure 3.9b, is the increase in coherent noise in the Marchenko imaging result. Again, this could be explained

by the algorithm's inability to focus when out-of-plane reflections are included in the input data, the focusing energy is instead misplaced and causes additional artefacts to be superimposed on the resulting images.

3.8.2 Computational Cost

Consider first the differences in storage requirements for Marchenko methods applied to two- and three-dimensional seismic data. There are three variables that impact the size of the seismic dataset: the number of time samples per trace (N_t), the number of sources (N_s) and the number of receivers (N_r): the total number of time samples in a seismic dataset is: $N_t \times N_s \times N_r$. If we assume that the number of sources is equal to the number of receivers (they are co-located) and that the number of sources in the y direction is equal to the number of sources in the x directions we can quantify the change in file size between two and three dimensions - this factor is $N_{s/r}^2$. For acquisition setups even with relatively few sources and receivers this scaling factor increases the data storage requirements by several orders of magnitude. In practice this can be reduced through survey design and data compression. This is a problem for implementation of any imaging algorithm in three dimensions (e.g. RTM), however, for the implementation of the Marchenko method defined in this chapter we require the full reflection response (from every source to every receiver) to be convolved with the intermediate outputs (equations 3.5-3.7) multiple times to calculate the Green's function for a single imaging point. Therefore due to the large file size the three-dimensional Marchenko methods require shared memory machines and parallelised algorithms to keep processing times reasonable.

It is also of interest to quantify how the number of calculations required to implement Marchenko methods scales with increasing dimensionality. The most computationally intensive parts of the algorithm (in higher dimensions) are the convolution steps. Therefore, in Table 3.1 we have calculated the number of

	Number of convolutions	Example
1D	$2n + 3$	13
2D	$(2n + 3)(nx^2)$	1.41×10^5
3D	$(2n + 3)(nx^2 \times ny^2)$	4.56×10^8

Table 3.1: A comparison of the number of convolutions required for Marchenko Green's functions calculation with increasing dimensionality. Column two provides a formula for the calculation count and column three is an example based on the survey parameters used within this chapter (Figure 3.3b) with $n = 5$.

convolutions required for the implementation of Marchenko methods in 1D, 2D and 3D. Here n is the number of iterations, nx is the number of sources/receivers in the x direction, and ny is the number of sources/receivers in the y dimension. In Table 3.1 the number of convolutions $2n + 3$ is the number of times in the Marchenko workflow each input trace is convolved with each trace in the reflectivity. The second component of this equation (e.g. nx^2) is a function of the size of the reflectivity which therefore varies between dimensions. This term accounts for the number of convolutions between every source and every receiver, so its value is the size of the data squared. There are several orders of magnitude between the calculation count required in different dimensionalities, and because of this in the examples conducted herein the run-time of the algorithm for a single Green's function estimate varies from fractions of a second in lower dimensionalities to hours in higher dimensionalities.

3.9 Conclusion

In this chapter we have shown that Marchenko methods can be applied to seismic data from areal arrays (so-called three-dimensional seismic data) in order to image subsurface structures that are three-dimensional. However, if only linear seismic acquisition arrays are used, the reflectivity must first undergo amplitude

and phase corrections to be consistent with the two-dimensional Marchenko equations which must be applied. These corrections result in significantly improved Green's function estimates. However, when out-of-plane reflections occur in the subsurface, two-dimensional Marchenko methods are unable to estimate Green's functions accurately. This is because the accuracy of the focusing functions is reduced so the advantages of the Marchenko method are compromised and the resulting images are less accurate than those produced using standard imaging methods. The minimum density of arrays required to implement the Marchenko methods is a receiver spacing of approximately $\lambda_A \big/ 4$ where λ_A is the dominant wavelength. This represents an impractical constraint in many real acquisition scenarios. Future work will require careful consideration of the mode of implementation and the associated computational costs of applying Marchenko methods in three-dimensions.

3.10 Acknowledgments

The authors would like to thank Petrobras and Shell for their sponsorship of the International Centre for Carbonate Reservoirs (ICCR), and for permission to publish this work from the VSP project. We would also like to thank the fellow members of the ICCR and members of the Edinburgh Interferometry Project (EIP) for their numerous fruitful discussions.

Chapter 4

Imaging Vertical Structures using Marchenko Methods with Vertical Seismic Profile Data

Angus Lomas[1], Satyan Singh[1] and Andrew Curtis[1,2]

In this chapter we focus on incorporating vertical seismic profile (VSP) data into Marchenko methods, more specifically we aim to make use of the additional wavefield sampling from downhole seismic data to improve the accuracy of the results. To do this we have reverted back to two-dimensional examples (to reduce the computational cost), however we have demonstrated in the previous chapter that the same concepts hold in three dimensions. In the preceding chapters we have shown that Marchenko methods can accurately estimate Green's functions for simple sub-horizontal surface structures. Here

[1]School of GeoSciences, University of Edinburgh, Edinburgh, UK
[2]Institute of Geophysics, ETH Zurich, Zurich, Switzerland

we focus on areas of complexity – steeply dipping subsurface structures, where the results from standard Marchenko methods will be inaccurate.

4.1 Introduction

Marchenko methods are novel techniques used in geophysics to redatum receivers that are physically located on the Earth's surface to arbitrary virtual receiver positions inside the subsurface. The methods estimate the seismograms that would have been recorded at those new positions if physical receivers had been placed there. Marchenko methods have applications that include Marchenko and target oriented imaging (Behura *et al.*, 2014; Wapenaar *et al.*, 2014; Ravasi *et al.*, 2016), redatuming (Wapenaar *et al.*, 2014; Ravasi, 2017) and internal multiple attenuation (Meles *et al.*, 2014, 2016; da Costa Filho *et al.*, 2017). Their advantage over most other redatuming methods is that they account for the reverberations of waves within the Earth (so-called internal multiples) using just single-sided illumination of the subsurface and a smooth estimate of the subsurface velocity structure. The original implementations of these techniques, which we follow in this article, focus on acoustic problems with an absorbing surface boundary (Broggini *et al.*, 2012; Wapenaar *et al.*, 2013). However, more recent applications have extended the methodology to elastic media (da Costa Filho *et al.*, 2014, 2015) and data containing free surface multiples (Singh *et al.*, 2015, 2016; Ravasi, 2017; Slob and Wapenaar, 2017). The aim of the work in this chapter is to incorporate the additional information available from vertical seismic profile (VSP) data to improve Marchenko estimates of Green's functions, thereby improving the final images of the Earth's subsurface.

A recent theoretical advance in this field is so-called 'Marchenko source-receiver redatuming'. These methods use receiver-redatumed Green's functions calculated using Marchenko methods to also redatum the source to a second arbitrary

subsurface location (Wapenaar *et al.*, 2016; Singh and Snieder, 2017a; Wapenaar *et al.*, 2018). In this chapter we propose that the receiver redatumed signals can be replaced with a measured VSP signal. The advantage of including this type of data is that it enables more accurate Green's functions to be calculated. In particular, wavefield components can be constructed to which the Marchenko method alone is insensitive – in this case reflections from vertical or near vertical interfaces. This in turn will allow Marchenko images to be produced that identify vertical and steeply-dipping subsurface features while retaining the ability to image sub-horizontal structures and reduce internal multiple contamination.

Previous studies incorporating seismic data measured by downhole receivers into Marchenko methods aimed to reduce the sensitivity of Marchenko methods to velocity model errors (Liu *et al.*, 2016), to estimate the scaling factor of reflection data, which is normally a prerequisite for applying Marchenko methods (van der Neut *et al.*, 2015c; Thomsen *et al.*, 2017), or to develop novel methods for wavefield separation (Liu *et al.*, 2018). In all of these examples the downhole receivers are used as an additional control when calculating standard Marchenko Green's functions. None of these methods exploit the additional full wavefield recordings available from the downhole receivers.

The virtual source method proposed by Bakulin and Calvert (2006) demonstrated the applicability of interferometric concepts to use data measured downhole to redatum sources to create virtual sources inside the well. This method is advantageous as it is able to account for complexities in the overburden without requiring an accurate estimate of the velocity model. A similar approach was taken by Hornby and Yu (2007) to image the flank of salt structures. Comparisons between methods like these and source-receiver Marchenko redatuming methods have previously been analysed by Singh and Snieder (2017a).

Alternative methods for imaging vertical interfaces have also been proposed:

Xu and Jin (2006) suggested using wave equation migration of diving waves to image the flank of salt structures and Malcolm *et al.* (2009) showed that vertical interfaces can be mapped using multiply scattered seismic waves, surface seismic data and wave equation migration when abrupt interfaces are correctly included in the input velocity model. For both of these methods an exceptionally accurate velocity model is required for accurate reflector mapping, and internal multiple contamination in the final images remains a problem. More recently Zuberi and Alkhalifah (2014) suggested using multiply-scattered waves measured in surface seismic data (duplex waves) to image vertical and near vertical interfaces, but the results were shown to be prone to contamination by artifacts. Finally, Singh and Curtis (2018) also used surface seismic data and so-called time-reverse mirror imaging (TRMI) which uses an autocorrelation imaging condition: this methodology was shown to accurately image vertical interfaces but was insensitive to horizontal features.

In this chapter we first introduce the standard Marchenko theory, how this relates to the more recent 'virtual source-virtual receiver' developments, and our approach to incorporate VSP data. We then analyse the impacts of a vertical interface on standard Marchenko estimates, which are shown to produce poor reconstructions of wavefield components created by vertically orientated subsurface features. We then focus on the VSP application: we use the new method to construct improved subsurface seismic wavefield estimates, then use this wavefield for seismic imaging. The images created as a result are accurate and would be unobtainable with existing alternative imaging methods alone.

4.2 Marchenko Methods

4.2.1 Marchenko Receiver Redatuming

Standard Marchenko methods require seismic reflection data measured at co-located source and receiver positions on or near the surface of the Earth (R), and an estimated model of the subsurface velocity structure. The methods calculate directionally decomposed seismograms (the pressure recording in response to a point source) – which are referred to herein as (band-limited) Green's functions ($G^{+/-}(\mathbf{x}_i, \mathbf{x}_0, \omega)$) – between the surface source positions ($\mathbf{x}_0$) and an arbitrarily chosen virtual receiver position ($\mathbf{x}_i$) inside the subsurface. Throughout this chapter these are expressed in the frequency domain (ω). Directional decomposition is in the observed direction of wave propagation as it is measured at the receiver, and in all cases + denotes downgoing and − denotes upgoing waves. The equations that govern the relationship between the reflectivity (R) and the Green's functions of interest are:

$$G^{-}(\mathbf{x}_i, \mathbf{x}_0, \omega) = \int_{\partial \mathbb{D}_0} R(\mathbf{x}_0, \mathbf{x}'_0, \omega) f_1^{+}(\mathbf{x}'_0, \mathbf{x}_i, \omega) d\mathbf{x}'_0 - f_1^{-}(\mathbf{x}_0, \mathbf{x}_i, \omega) \tag{4.1}$$

$$G^{+}(\mathbf{x}_i, \mathbf{x}_0, \omega) = f_1^{+}(\mathbf{x}_0, \mathbf{x}_i, \omega)^* - \int_{\partial \mathbb{D}_0} R(\mathbf{x}_0, \mathbf{x}'_0, \omega) f_1^{-}(\mathbf{x}'_0, \mathbf{x}_i, \omega)^* d\mathbf{x}'_0 \tag{4.2}$$

Each of the terms in equations 4.1 and 4.2 is a function of two sets of spatial locations: $\mathbf{x}_0$ represents an array of points on the boundary $\partial \mathbb{D}_0$ with a fixed depth coordinate $z = 0$ and a variable horizontal coordinate, $\mathbf{x}_0 = \{(x_j, y_j, 0) : j = 1, 2, \ldots, N\}$ where N is the number of source/receiver positions, and for this formulation the set of points in $\mathbf{x}_0$ has to equal that in $\mathbf{x}'_0$. Location $\mathbf{x}_i = (x, y, i)$

represents a point on the boundary $\partial\mathbb{D}_i$. Here f_1 denotes a so-called focusing function: the downgoing component of this function is defined such that when it is injected as a source time function into the true subsurface model it will collapse at zero time to an impulse at the virtual source location (Slob *et al.*, 2014b). The upgoing component of the focusing function is the measured response at the surface to the injection of the downgoing functions. However, this is only the case in a truncated medium which is defined to be equal to the true medium above a boundary of constant depth $\partial\mathbb{D}_i$, and is homogeneous below this depth. We calculate these functions using the iterative solution to the coupled Marchenko equations (Wapenaar *et al.*, 2014) and we refer readers to Lomas and Curtis (2019) for an intuitive introduction and more details on this method.

The theoretical foundation of equations 4.1 and 4.2 are the one-way reciprocity theorems of the convolution and correlation type for pressure normalized one-way wavefields (Wapenaar and Grimbergen, 1996; Wapenaar *et al.*, 2014):

$$-\int_{\partial\mathbb{D}_0} \frac{1}{\rho(\mathbf{x}_0')} \left[p_A^+(\partial_z p_B^-) + p_A^-(\partial_z p_B^+)\right] d\mathbf{x}_0' = \int_{\partial\mathbb{D}_i} \frac{1}{\rho(\mathbf{x}_i')} \left[(\partial_z p_A^+)p_B^- + (\partial_z p_A^-)p_B^+\right] d\mathbf{x}_i' \tag{4.3}$$

$$-\int_{\partial\mathbb{D}_0} \frac{1}{\rho(\mathbf{x}_0')} \left[p_A^{+*}(\partial_z p_B^+) + p_A^{-*}(\partial_z p_B^-)\right] d\mathbf{x}_0' = \int_{\partial\mathbb{D}_i} \frac{1}{\rho(\mathbf{x}_i')} \left[(\partial_z p_A^+)^* p_B^+ + (\partial_z p_A^-)^* p_B^-)\right] d\mathbf{x}_i' \tag{4.4}$$

Equations 4.3 and 4.4 are given in the frequency domain, subscripts A and B refer

to two different acoustic states, $p_{A/B}$ represents a wavefield in the state defined by their subscript, ∂_z represents the vertical derivative of the corresponding wavefield and superscript $*$ denotes complex conjugation (or time reversal). Furthermore, these equations only hold under certain conditions: first there can not be any energy source at a depth level between the boundary $\partial\mathbb{D}_0$ and the boundary $\partial\mathbb{D}_i$, evanescent waves are not present in any of the measured wavefields, and for equation 4.4 to hold the medium needs to be lossless between the boundary $\partial\mathbb{D}_0$ and the boundary $\partial\mathbb{D}_i$.

If we take state A to be the state in which the focusing functions exist in the truncated medium and state B to be the Green's functions state in the true medium we can assign the values $p_A^{+/-} = f_1^{+/-}(\mathbf{x}_0'/\mathbf{x}_i', \mathbf{x}_i, \omega)$ and $p_B^{+/-} = G^{+/-}(\mathbf{x}_0'/\mathbf{x}_i', \mathbf{x}_0, \omega)$ where the receiver position is defined by the corresponding boundary integral, and to be clear, the symbol / in this context means 'or'. Following the method in appendix A of Wapenaar *et al.* (2014) these wavefields can be substituted into equations 4.3 and 4.4 to form equations 4.1 and 4.2.

4.2.2 Marchenko Source-Receiver Redatuming

The previous section describes equations 4.1 and 4.2 which are used as part of the Marchenko method to construct signals between the surface acquisition array and subsurface virtual receivers. More recent work has shown how we can use the estimated Marchenko Green's functions to redatum the Green's functions as if the source was also at an arbitrary point inside the subsurface, so-called Marchenko source-receiver redatuming. This work is the natural extension of source-receiver interferometric methods of Curtis and Halliday (2010) and Halliday and Curtis (2010) to the case of single-sided acquisition and Marchenko methods. It was pioneered by Wapenaar *et al.* (2016) and Singh and Snieder (2017a) and has recently been applied to real data (Wapenaar *et al.*, 2018), and extended to elastodynamic applications (Urruticoechea and Wapenaar, 2017).

	State A	State B
on $\partial\mathbb{D}_0$	$p_A^+ = f_1^+(\mathbf{x}_0, \mathbf{x}_i, \omega)$	$\partial_z p_B^+ = 0$
	$p_A^- = f_1^-(\mathbf{x}_0, \mathbf{x}_i, \omega)$	$\partial_z p_B^- = \partial_z G(\mathbf{x}_0, \mathbf{x}_j, \omega)$
on $\partial\mathbb{D}_i$	$\partial_z p_A^+ = -\frac{1}{2} j\omega\rho(\mathbf{x}_i')\delta(\mathbf{x}_i - \mathbf{x}_i')$	$p_B^+ = G^+(\mathbf{x}_i', \mathbf{x}_j, \omega)$
	$\partial_z p_A^- = 0$	$p_B^- = G^-(\mathbf{x}_i', \mathbf{x}_j, \omega)$

Table 4.1: A comparison of the wavefields $p_{A/B}^{+/-}$, where state A represents the focusing state and state B represents the Green's functions state. These wavefields are evaluated on the boundaries $\partial\mathbb{D}_0$ and $\partial\mathbb{D}_i$.

In this chapter we suggest a method to incorporate VSP data into the source-receiver method. The advantage of doing this is that we overcome a limitation of the Marchenko method – the ability to handle steeply dipping subsurface interfaces, which ultimately allows us to obtain more accurate Green's functions. In particular this enables the Marchenko method to better construct virtual-source virtual-receiver Green's functions, and thus to produce improved seismic images of vertical or near-vertical interfaces.

Here we follow the implemetation of the technique of Singh and Snieder (2017a), however we have simplified the problem by assuming that there are no free-surface multiples present in the data (i.e. that surface-related multiples have been removed from recorded data). However, this is not a limitation of the method we introduce in this chapter and the methodology can be applied to the case where the seismic data does contain free-surface multiples.

The relationship between the measured Green's functions from the previous section and the Green's functions of interest here are retrieved by substituting the wavefields from Table 4.1 into the modified reciprocity theorems from equations 4.3 and 4.4 ($d\mathbf{x}_0' \rightarrow d\mathbf{x}_0$). If j is the imaginary unit, ω is angular frequency and ρ is density then:

$$G^{-}(\mathbf{x}_i, \mathbf{x}_j, \omega) = \int_{\partial \mathbb{D}_0} \frac{2}{j\omega\rho(\mathbf{x}_0)} \partial_z G(\mathbf{x}_0, \mathbf{x}_j, \omega) f_1^{+}(\mathbf{x}_0, \mathbf{x}_i, \omega) d\mathbf{x}_0 \tag{4.5}$$

$$G^{+}(\mathbf{x}_i, \mathbf{x}_j, \omega) = -\int_{\partial \mathbb{D}_0} \frac{2}{j\omega\rho(\mathbf{x}_0)} \partial_z G(\mathbf{x}_0, \mathbf{x}_j, \omega) f_1^{-}(\mathbf{x}_0, \mathbf{x}_i, \omega)^* d\mathbf{x}_0 \tag{4.6}$$

If we sum equations 4.5 and 4.6 we obtain:

$$G(\mathbf{x}_i, \mathbf{x}_j, \omega) = \int_{\partial \mathbb{D}_0} \frac{2}{j\omega\rho(\mathbf{x}_0)} \partial_z G(\mathbf{x}_0, \mathbf{x}_j, \omega) f_2(\mathbf{x}_i, \mathbf{x}_0, \omega) d\mathbf{x}_0 \tag{4.7}$$

where $f_2(\mathbf{x}_i, \mathbf{x}_0, \omega) = f_1^{+}(\mathbf{x}_0, \mathbf{x}_i, \omega) - f_1^{-}(\mathbf{x}_0, \mathbf{x}_i, \omega)^*$. Equations 4.5-4.7 only hold if point $\mathbf{x}_i$ is at a depth above $\mathbf{x}_j$: $i < j$. In other words the virtual source term in the Green's functions needs to be below the virtual receiver term of the focusing functions. When both the Green's functions and the focusing functions are estimated using Marchenko methods these are interchangeable (by source-receiver reciprocity) and analogous equations exist when the depth coordinates satisfy $i > j$. However, in our implementation we propose that the Marchenko estimate of $G(\mathbf{x}_0, \mathbf{x}_j, \omega)$ be replaced by the approximation to the Green's function measured in a VSP survey. In so doing the location $\mathbf{x}_j$ and the G term cannot be changed: so when we implement equation 4.7 we can only construct Green's functions between arbitrarily chosen virtual receiver positions and the fixed VSP receivers (now virtual sources) inside the well.

We simplify equation 7 further given the definition of a particle velocity reponse to an impulsive point source of volume injection rate given by Wapenaar and Fokkema (2006):

$$v_z(\mathbf{x}_0, \mathbf{x}_j, \omega) = -\frac{1}{j\omega\rho(\mathbf{x}_0)}\partial_z G(\mathbf{x}_0, \mathbf{x}_j, \omega) \tag{4.8}$$

Here the volume injection rate sources are in the borehole and the particle velocity receivers are at the surface, however, by source-receiver reciprocity this is equivalent to a vertical force source at the surface and a pressure measurement in the borehole (Thorbecke *et al.*, 2017). Substituting equation 4.8 into equation 4.7 then leads to:

$$G(\mathbf{x}_i, \mathbf{x}_j, \omega) = -2 \int_{\partial\mathbb{D}_0} v_z(\mathbf{x}_0, \mathbf{x}_j, \omega) f_2(\mathbf{x}_i, \mathbf{x}_0, \omega) d\mathbf{x}_0 \tag{4.9}$$

The original implementation of these methods proposed that both terms inside the integral in equation 4.9 can be estimated using Marchenko methods. The focusing function is calculated using the iterative Marchenko method (Wapenaar *et al.*, 2014) and the Green's function is calculated by summing the results from equations 4.1 and 4.2. When using only inputs from previous Marchenko methods, the vertical particle velocity from equations 4.9 is not available and must be approximated (Wapenaar *et al.*, 2017) – we discuss this in more detail below.

A limitation of using Marchenko Green's functions from equations 4.1 and 4.2 is that they are only able to accurately reconstruct the reflected components of the Marchenko Green's functions from equation 4.7 when the primary reflections from the structural features that caused them are measured at the surface of the Earth. Therefore, depending on the aperture of the seismic acquisition, equation 4.7 is often only accurate for near-horizontal subsurface structures. The object of our investigation is to obtain a subsurface image in cases where this assumption does not hold, as shown in Figure 4.1. Replacing the approximate Marchenko Green's function with the VSP Green's function therefore includes the potential

to image more complex subsurface structures, whilst retaining the benefits of the Marchenko method to redatum wavefields and to account for the effects of internal multiples.

4.3 Green's Function Estimation

We first use a simple synthetic subsurface model to test these methods (Figure 4.1). This model has variable density but a constant velocity ($2500m/s$) with several horizontal layers. However, we have introduced a challenge for standard Marchenko imaging by including a vertical interface at $x = 1000m$. Along the surface there are co-located sources and receivers at $16m$ intervals which make up the acquisition array described by the vector of locations $\mathbf{x}_0$. Additionally, inside the subsurface, there is a VSP with receivers at variable depth positions, again spaced at $16m$ intervals with a constant x coordinate of $1500m$.

4.3.1 Receiver Redatuming

As a first example we consider the accuracy of Marchenko Green's function estimates for redatumed receivers with a vertical interface present in the subsurface (Figure 4.1). We first estimate the focusing functions, then use equations 4.1 and 4.2 to estimate Green's functions, and finally sum the result: $G(\mathbf{x}_i, \mathbf{x}_0, t) = G^+(\mathbf{x}_i, \mathbf{x}_0, t) + G^-(\mathbf{x}_i, \mathbf{x}_0, t)$. This is applied for a single surface source at $(2004m, 0m)$ on the boundary $\partial\mathbb{D}_0$ and an array of receivers in the subsurface, the same receivers that make up the VSP (see Figure 4.1). The results are given in Figure 4.2 where we compare the estimated Marchenko Green's functions and the measured (directly modelled) Green's functions from the VSP.

Figure 4.2 shows that the Marchenko result gives accurate Green's functions for reflections from the horizontal subsurface layers. The accuracy of these signals

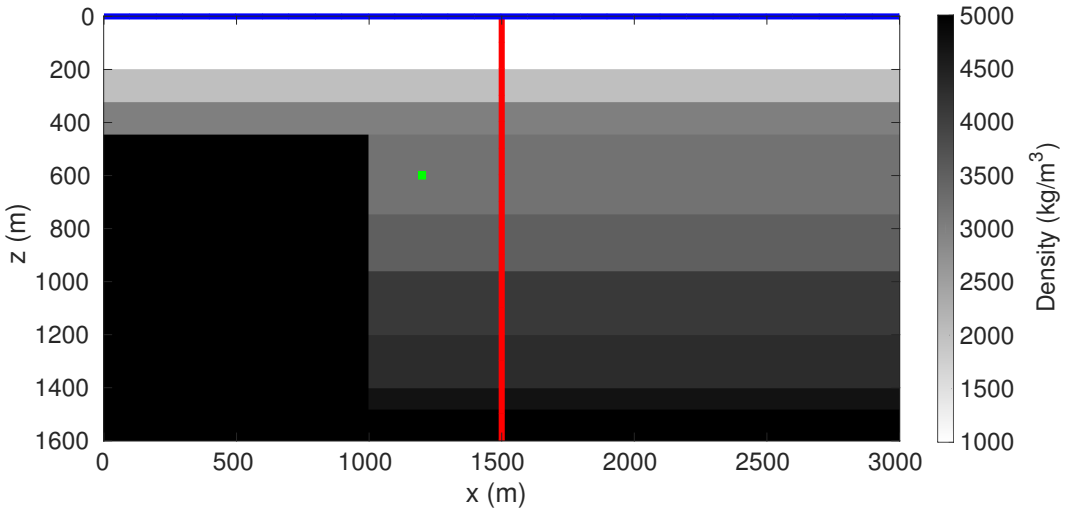

Figure 4.1: A two-dimensional synthetic variable density, constant velocity ($2500m/s$) subsurface model. Seismic data were simulated on the surface of this model ($z = 0$) from co-located sources and receivers along the blue line. A complementary VSP data set was also simulated between sources along the blue line and downhole receivers along the red line. In all cases the source and receiver spacing was $16m$. The green dot at $(1200m, 600m)$ is the virtual-source receiver used in Figure 4.3.

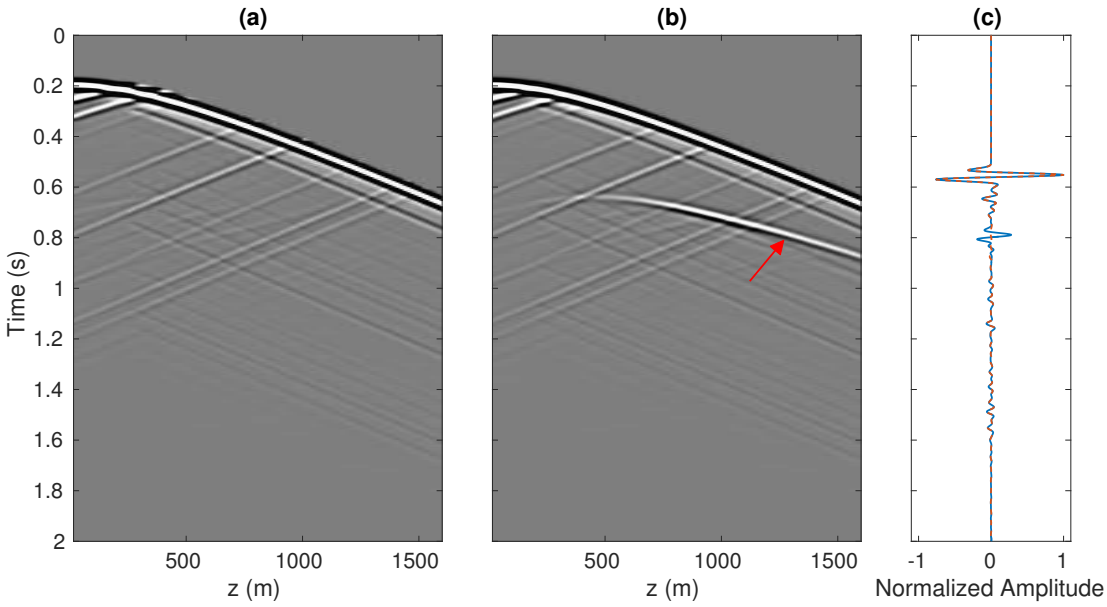

Figure 4.2: A comparison of Marchenko estimated Green's functions between a source at $x = 2004m$ on the surface and VSP receivers in the well $x = 1500m$ (Figure 4.1). Panel (a) shows the calculated recordings using Marchenko estimates (virtual receivers) and panel (b) shows the true solution as measured by the VSP. The red arrow indicates an event reflected from the vertical interfaces that is missing from the Marchenko estimate in panel (a). Panel (c) compares a single trace ($z = 1296m$) for the Marchenko estimated Green's function (orange) and the VSP Green's function (blue): for display purposes this plot has a time dependent gain applied.

is most apparent in Figure 4.2c where the match with the true solution is nearly perfect. This level of accuracy has also been demonstrated for other examples in previous literature (e.g. Wapenaar *et al.* (2013)). However, components of the seismic wavefield that have interacted with the vertical interface, marked by the red arrow, are not reconstructed and are missing from the Marchenko estimate of the VSP data. This result is to be expected because most of the energy that reflects from vertical interfaces follows paths down into the deeper Earth, hence is not recorded in surface seismic data and therefore can not be reconstructed by purely one-sided (ground-surface data driven) Marchenko methods (or any method that relies on primary reflections measured at the surface). The same focusing function term is used in equation 4.7 to produce both Figures 4.2a and 4.2b. This confirms that the focusing function is accurate (as it facilitates the accurate Green's function estimation in Figure 4.2b) and that the observed differences are due to the Green's functions on the right hand side of equation 4.7.

4.3.2 Source-Receiver Redatuming

We can use the results from Figure 4.2 to implement source-receiver redatuming using equation 4.7. The input to this equation is a vertical particle velocity measurement at the boundary $\partial\mathbb{D}_0$ in response to a volume injection rate source at point $\mathbf{x}_j$ in the subsurface (see equation 4.8 and 4.9) – reciprocal relationships exist for a reversed source-receiver layout (Thorbecke *et al.*, 2017). We can approximate the required response from the calculated Green's function in equations 4.1 and 4.2 and Figure 4.2a by making the approximation (Wapenaar and Fokkema, 2006):

$$\partial_z G(\mathbf{x}_0, \mathbf{x}_j, \omega) \approx -\frac{j\omega}{c(\mathbf{x}_0)} G(\mathbf{x}_0, \mathbf{x}_j, \omega) \tag{4.10}$$

We then substitute equation 4.10 into equation 4.7 to obtain:

$$G(\mathbf{x}_i, \mathbf{x}_j, \omega) \approx -\int_{\partial \mathbb{D}_0} \frac{2}{c(\mathbf{x}_0)\rho(\mathbf{x}_0)} G(\mathbf{x}_0, \mathbf{x}_j, \omega) f_2(\mathbf{x}_i, \mathbf{x}_0, \omega) d\mathbf{x}_0 \tag{4.11}$$

where c is velocity. These steps are similar to those taken to derive source-receiver interferometry (Curtis *et al.*, 2009; Curtis and Halliday, 2010) which also provides alternative derivations of Green's functions between virtual sources and virtual receivers.

In the examples presented in this chapter, we assume that for the VSP data we have measured the response at the downhole receivers to a vertical force source on the surface of the earth. We can therefore implement equations 4.11 and 4.9 using the Marchenko-estimated and VSP-measured Green's functions to produce figure 4.3a and 4.3b respectively. To do this we have arbitrarily chosen a subsurface source location at $\mathbf{x}_i = 1200m, 600m$ and calculated the focusing term $f_2(\mathbf{x}_i, \mathbf{x}_0, \omega)$ to this point.

Figure 4.3a again shows that standard Marchenko estimates are unable to accurately reconstruct the wavefield components attributed to the vertical interfaces. However, comparing Figure 4.3b and 4.3c shows that including the true Green's function in equation 4.7 enables accurate estimation of all wavefield components. These features are confirmed by the trace comparison in Figure 4.3d. In Figure 4.3 we have limited the display to source depths of $600m$ and below: as already discussed the equations implemented are only valid when the sources are below the receiver positions. Furthermore, for virtual sources at shallow depths the amplitudes are constructed less accurately due to limited apertures; this is because the virtual source locations are closer in terms of depth to the virtual receiver location.

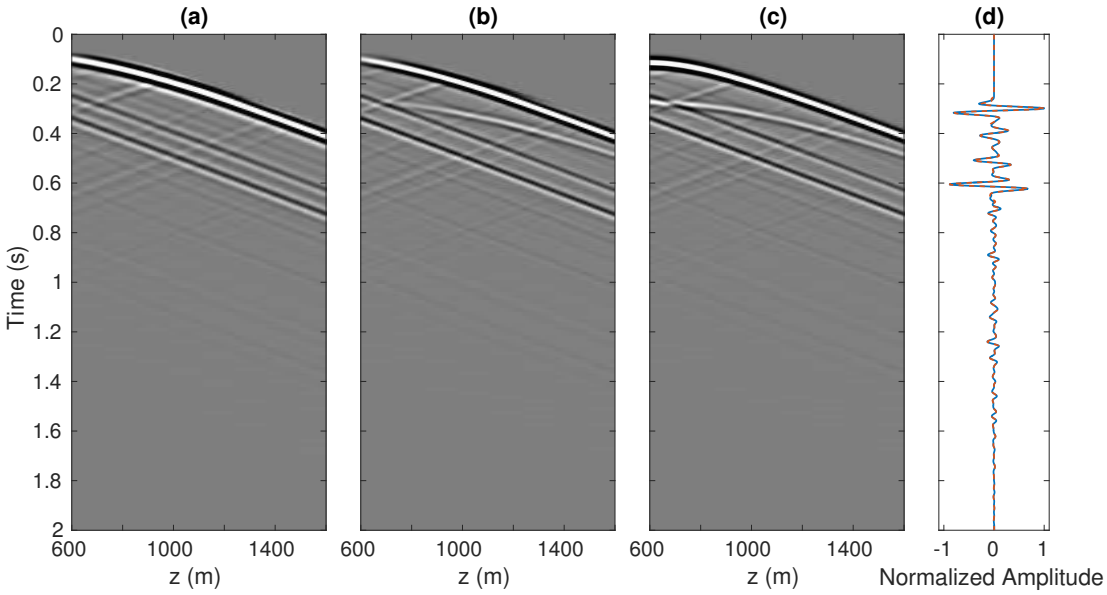

Figure 4.3: A comparison of Marchenko estimated Green's functions between a virtual receiver at $(1200m, 600m)$ and VSP receivers (now virtual sources) in the well $x = 1500m$ (Figure 4.1). Panel (a) shows the calculated recordings using Marchenko estimates (virtual receivers and virtual sources), panel (b) shows the result using the virtual receiver and VSP receivers, and for comparison panel (c) shows the modelled result between a source at the virtual receiver location and the VSP receivers. Panel (d) compares a single trace ($z = 1296m$) for the Marchenko estimated Green's function from panel (b) (orange) and the true Green's function using the VSP data from panel (c) (blue): for display purposes this plot has a time dependent gain applied.

4.3.3 Marchenko Wavefield Estimation

The source-receiver redatuming methods we have so far introduced are of particular interest to geophysicists because they are capable of estimating a full wavefield from any arbitrarily chosen virtual source location inside the subsurface (as virtual receivers can be placed anywhere in the subsurface). Our suggested methodology incorporates VSP data into this workflow, however we can then no longer place a virtual source arbitrarily in the subsurface. Instead the virtual source must be located at one of the VSP receivers. Nevertheless, virtual receivers can be placed arbitrarily as long as they are placed above the depth level of the virtual source. We have therefore implemented equation 4.7 for one virtual source location ($\mathbf{x}_j = 1500m, 1296m$) and a grid of virtual receiver locations ($\mathbf{x}_i$), transformed from the frequency to the time domain and the resulting wavefield is shown in Figure 4.4.

Figure 4.4 shows the wavefield at six time steps of $\Delta t = 0.1s$. The area of interest is the vertical interface at $x = 1000m$. Because we have included the VSP data (the true surface-to-subsurface Green's function) in the source-receiver Marchenko method we are able to construct interactions between this feature and the propagating wavefield (blue arrows show the reflection from the vertical interface). Although not shown, the wavefield constructed using standard Marchenko fields is identical except that it does not include these features as they are not included in the input Green's function as shown in Figure 4.2.

4.4 Subsurface Imaging

So far we have demonstrated a Marchenko method that uses VSP data to estimate Green's functions with improved accuracy over those constructed using existing source-receiver Marchenko methods. In this section we investigate how we can

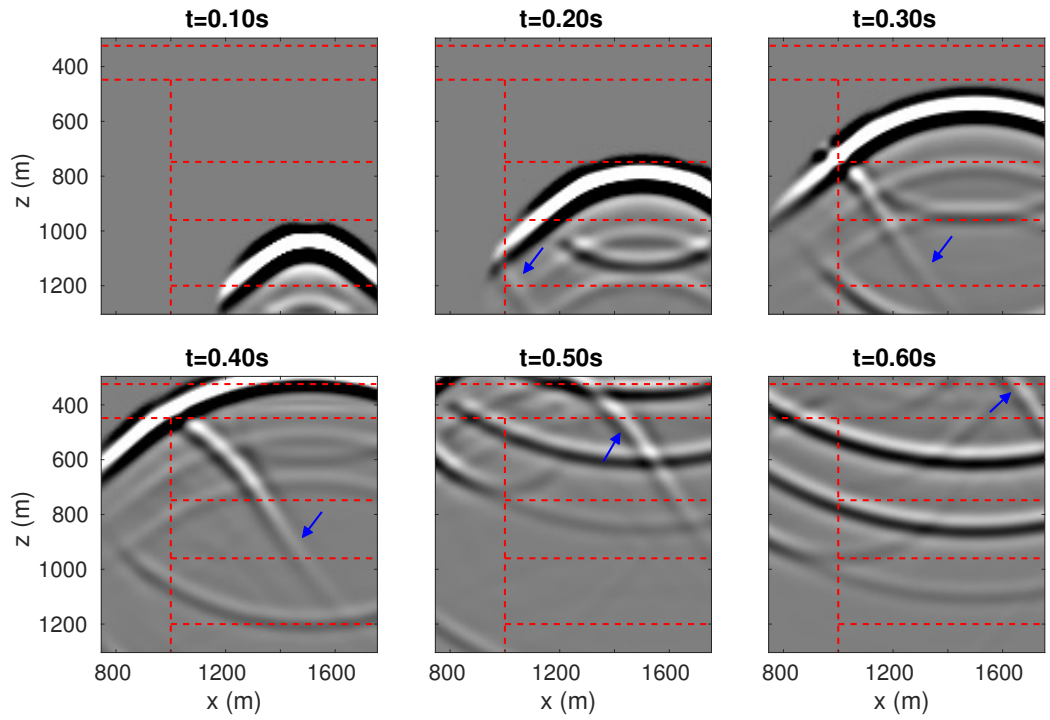

Figure 4.4: An estimated wavefield from a source at $(1296m, 1500m)$ constructed using the virtual source-receiver Marchenko method including VSP data. The panels show the wavefield at time intervals of $0.1s$ after the source origin time. The red dashed lines indicate the boundaries of true subsurface density variations and the blue arrows identify the primary reflections from the vertical interface.

use these estimates to obtain improved images of the subsurface.

4.4.1 VSP Driven Imaging

The aim of seismic imaging is to map subsurface spatial heterogeneities – locations at which seismic waves diffract or reflect. Effectively we are trying to isolate the scattering component of a wavefield and calculate where these components originate. This mapping operation can be defined as (Vasconcelos *et al.*, 2010; Fleury and Vasconcelos, 2012):

$$I_n(\mathbf{x}_k) = G_s(\mathbf{x}_k, \mathbf{x}_k, t=0) = \int_{-\infty}^{\infty} G_s(\mathbf{x}_k, \mathbf{x}_k, \omega) d\omega \tag{4.12}$$

where $G_s(\mathbf{x}_k, \mathbf{x}_k, t)$ is the scattering components of the Green's function with a single co-located source and receiver. The total Green's functions can be related to the scattered Green's function through: $G = G_0 + G_s$, where G_0 is the Green's function measured in a smooth reference model. Only if the source/receiver is on a reflector will there be a signal measured at zero time, and hence to construct an image G_s is evaluated at $t = 0$. The subscript n is an indexing term to account for the different images produced by equation 4.12 in the following sections of this chapter.

In practice, we do not have an accurate measure of G_s, nor do we have a source and receiver at every subsurface location (image point) of interest: to solve equation 4.12 we need to estimate these. Various imaging conditions are employed in wave equation based migration techniques to attempt to solve this problem (Jones, 2014). However, in the previous section we have presented a method that accurately estimates wavefields propagating through the subsurface – Green's functions to all points. In equation 4.12 we therefore choose an imaging

condition that exploits this additional information.

Our Marchenko method estimates full Green's functions G. In order to estimate the scattering Green's function we apply a mute to the Green's function such that:

$$G_s(\mathbf{x}_i, \mathbf{x}_j, t) \approx \Psi G(\mathbf{x}_i, \mathbf{x}_j, t) \tag{4.13}$$

where ΨG is the muted version of the Green's function from equation 4.9, and the mute removes components that arrive before or at the same time as the direct arrival (plus a small time lag to account for the dominant period of the source term). We can estimate the travel time required to calculate this mute using the reference velocity model, which is already a standard prerequisite for implementing the Marchenko method. Note that this is an approximation as at locations on or near scattering points the mute will also remove components of the scattered Green's function; we return to this below. If the initial velocity model is inaccurate the first arrivals could be manually or automatically picked. However, in this case alternative methods for estimating Green's functions using Marchenko methods when the subsurface velocity model is unknown would need to be applied (e.g. van der Neut and Wapenaar (2016)).

In Figure 4.4, we showed that Green's functions can be estimated between virtual sources in the well and a variety of virtual receiver locations. Waveforms constructed at each such location contain information about reflections in the subsurface, all of which we would like to use to construct the image. We do this using standard time migration methods applied to all subsurface receiver locations: first we use the reference velocity model to calculate background Green's functions G_0 between the imaging point ($\mathbf{x}_k$) and the source/receiver locations ($\mathbf{x}_j/\mathbf{x}_i$). These can be used to 'redatum' the Green's function by:

$$G_s(\mathbf{x}_k, \mathbf{x}_k, \omega) \approx \int_{\mathbb{D}_i} G_0(\mathbf{x}_k, \mathbf{x}_i, \omega)^* \left[\int_{\partial\mathbb{D}_j} G_s(\mathbf{x}_i, \mathbf{x}_j, \omega) G_0(\mathbf{x}_j, \mathbf{x}_k, \omega)^* d\mathbf{x}_j \right] d^2\mathbf{x}_i \tag{4.14}$$

where $\mathbb{D}_i$ is a volume of virtual receivers at the locations used to construct Figure 4.4. Equation 4.14 can then be used to create an image of the subsurface I_1 using equation 4.12. This imaging condition overcomes the limitations of estimating G_s by applying a mute from equation 4.13 since almost all of the wavefield components of interest will be outside of the muted zone. This methodology is not without its limitations and the amplitudes produced will not be accurate.

We can apply the workflow described above for multiple source locations (the VSP receivers in the well), multiple receiver locations at which we have calculated the wavefield in Figure 4.4, and an array of image points selected at $8m$ intervals in the area defined in Figure 4.5a. The result of this operation is given in Figure 4.5b. Equation 4.14 will not produce images completely free of multiple contamination, however, by including Marchenko Green's functions we are able to redautm the seismic data below the most significant multiple generators and increase the amount of data available to create an image, thus reducing multiple contamination in the result.

The image shown in Figure 4.5b accurately identifies all of the subsurface interfaces with few artifacts. The VSP data and the complimentary surface seismic data are both included in this imaging algorithm; therefore, due to poor illumination points at far offsets from the VSP are imaged less accurately. There is evidence of this in Figure 4.5b where the horizontal interface at $z = 450$ between $x = 800m - 1000m$ begins to loose continuity.

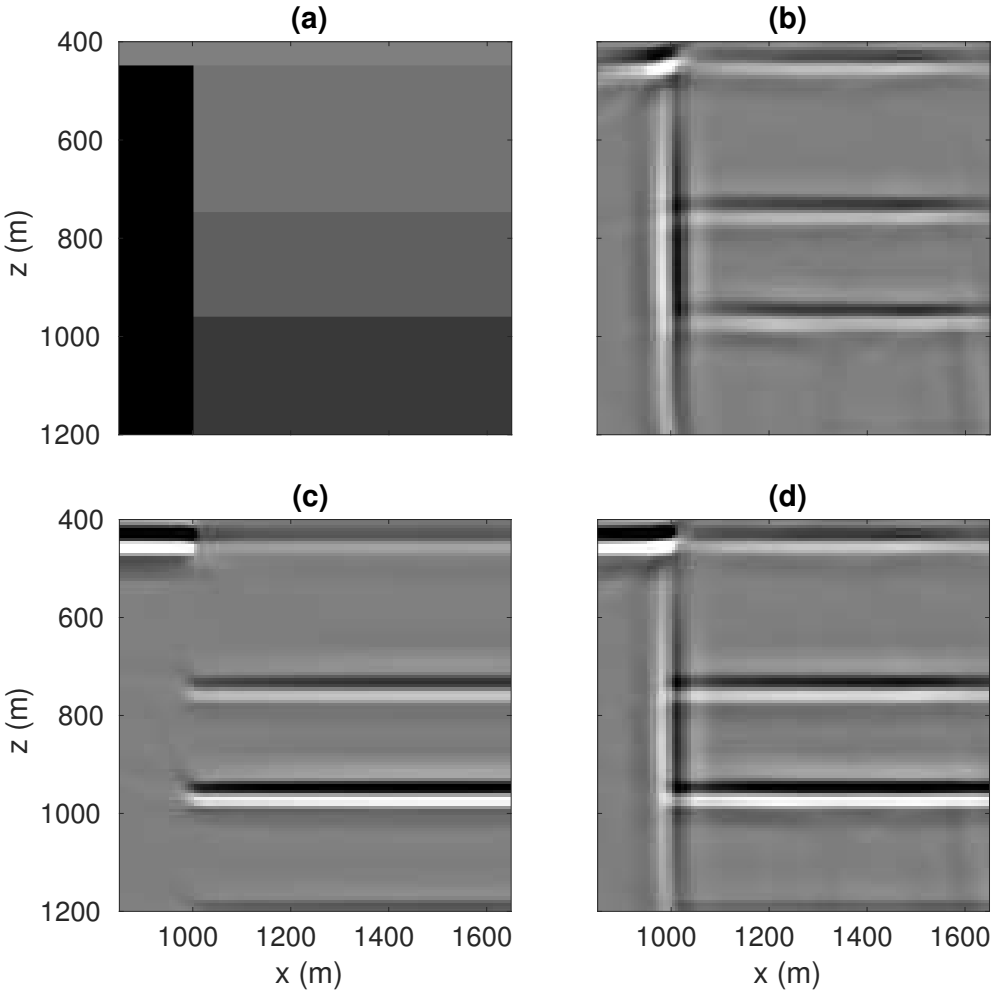

Figure 4.5: A comparison of images created using the data simulated through the model in Figure 4.1. Panel (a) shows the imaged area of the subsurface density model. Panel (b) shows imaging results using the VSP data and the imaging condition defined in equations 4.14 and 4.12. Panel (c) shows the image produced using standard Marchenko imaging methods (see equation 4.15). Panel (d) is the weighted sum of panels (b) and (c).

4.4.2 Combined Imaging

Given that the image produced in the previous section is limited by the illumination of the VSP it is also of interest to combine this data with surface seismic data which does not suffer from the same illumination issues, but which in theory cannot image the vertical structure of interest. To do so we first implement standard Marchenko imaging using just the surface seismic data from Figure 4.1. This uses the same imaging condition given in equation 4.12 and approximates the scattering Green's function as: $G_s(\mathbf{x}_k, \mathbf{x}_0, t) \approx G^-(\mathbf{x}_k, \mathbf{x}_0, t)$, where G^- is calculated using equation 4.1. This again is an approximation but is sufficient given that G^- will contain the singly reflected components required to create an image. We then apply:

$$G_s(\mathbf{x}_k, \mathbf{x}_k, \omega) \approx \int_{\partial\mathbb{D}_0} G^-(\mathbf{x}_k, \mathbf{x}_0, \omega) G_0(\mathbf{x}_0, \mathbf{x}_k, \omega)^* d\mathbf{x}_0 \tag{4.15}$$

The result of equation 4.15 can be substituted into equation 4.12 to create an image I_2. The resulting image is shown in Figure 4.5c.

Figure 4.5c shows a clean imaging result with all of the horizontal interfaces illuminated and accurately identified, but as expected, the vertical interface at $x = 1000m$ is not identified. It is clear that there are advantages and disadvantages to each of the images given in Figures 4.5b and 4.5c. We therefore propose that these images can be combined to give one imaging result.

A combined imaging condition was proposed by da Costa Filho and Curtis (2016) which is designed to maintain only features that are common to both images. Since in this case we wish to maintain the vertical interface which only appears in one of the images we need to adopt a slightly different approach. First we

apply a one-dimensional phase matching filter to the image I_2 in Figure 4.5c to ensure the mapped horizontal reflectors match those of I_1 in Figure 4.5b. We then weight the amplitudes of I_2 to ensure that the two images have similar energy distributions. Finally we sum the result ($I_3 = I_1 + I_2$), which is given in Figure 4.5d. This result draws on the benefits of both images: continuous horizontal reflectors as well as the vertical interface. It also exhibits a reduction in artifacts due to the increased signal to noise ratio.

4.4.3 Fault Imaging

The workflow described above provides a method to create images with reduced overburden multiple contamination in areas of structural complexity where there are steeply dipping interfaces such as salt flanks or fault planes. In this section we apply these methods to a more realistic synthetic subsurface model that includes a faulted structure – an adapted version of the Marmousi2 model (Martin *et al.*, 2006). We have adapted this model by isolating an area of interest and changing the velocity and density values from the original as we are only using acoustic properties. Our motivation was to create a model with a complex target feature (a fault in this case) and encourage multiply scattered waves with high values for acoustic impedance. These are the two problems to which the method we have formulated above should offer a solution. Figure 4.6a shows the subsurface velocity structure and Figure 4.6b show the density structure. Figure 4.6c shows a smoothed version of the subsurface velocity which we use as a reference model for the Marchenko method. Sources were placed on the surface ($z = 0m$) at $8m$ intervals and receivers were placed at each source point as well as at downhole locations ($x = 1600m$) again at $8m$ intervals.

We first use the surface seismic data to create an image of the subsurface as we did to obtain Figure 4.5c. The purpose of this is to asses the suitability and advantages of implementing Marchenko imaging in this subsurface model.

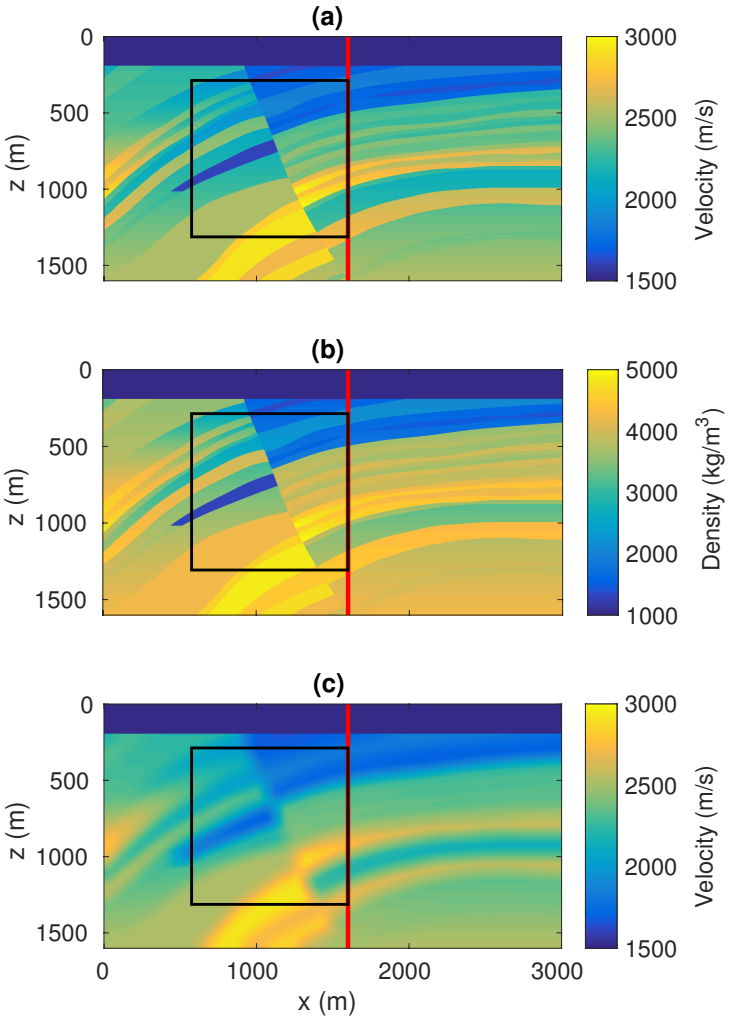

Figure 4.6: Acoustic properties of a synthetic subsurface model. Panel (a) shows the velocity structure, panel (b) shows the density structure and panel (c) shows a smoothed estimate of the velocity structure. This model is an adapted version of the original Marmousi2 model. We created synthetic surface seismic data from co-located sources and receivers at $8m$ intervals on the surface. Furthermore we created VSP data between the same surface sources and downhole receivers at $x = 1600m$, spaced at $8m$ intervals, indicated by the red line. The black square highlights the area imaged in Figure 4.7

Therefore for comparison we have also included an RTM-style image where we approximate:

$$G_s(\mathbf{x}_k, \mathbf{x}_k, \omega) \approx \int_{\partial \mathbb{D}_0} G_0^-(\mathbf{x}_k, \mathbf{x}_0, \omega) G_0(\mathbf{x}_0, \mathbf{x}_k, \omega)^* d\mathbf{x}_0 \tag{4.16}$$

where

$$G_0^-(\mathbf{x}_k, \mathbf{x}_0, \omega) = \int_{\partial \mathbb{D}_0} R(\mathbf{x}_0, \mathbf{x}_0', \omega) G_0(\mathbf{x}_0', \mathbf{x}_k, \omega)^* d\mathbf{x}_0' \tag{4.17}$$

Equations 4.16 and 4.17 are intended to approximate conventional migration methods that assume single scattering. A similar approach is taken in previous publications (see da Costa Filho and Curtis (2016) and Meles *et al.* (2018) for more details). In Figure 4.7a and 4.7b we compare the results from the imaging condition in equation 4.12 using the two scattering Green's function estimates in equation 4.15 and 4.16 respectively. The image result is target-oriented as we have only imaged a small portion of the subsurface model from Figure 4.6.

The results in Figure 4.7a and 4.7b show two images of the fault structure shown in Figure 4.6. Both show accurate images of the spatial heterogeneity with the best results observed in shallow areas. In the deeper parts the illumination deteriorates, in particular illumination of the fault structure which is poorly imaged in both panels. If we compare the two images it can be seen that the signal to noise ratio is worse in Figure 4.7b. This is highlighted by the difference panel in Figure 4.7c in which we observe many of the anomalous features of Figure 4.7b. The number of false reflectors is not significant however, which can be attributed to a limited number of high impedance continuous reflectors. Rather, the high impedance reflectors are shallow and discontinuous (see Figure

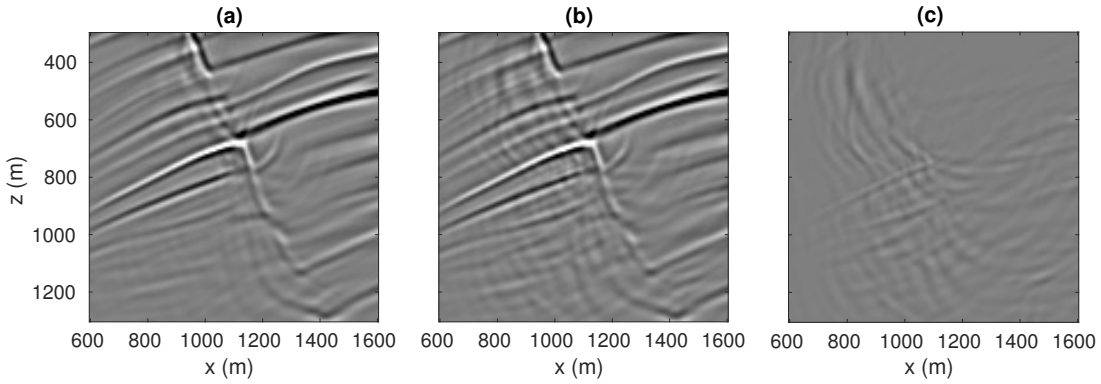

Figure 4.7: A comparison of images formed using (a) Marchenko Imaging and (b) conventional imaging methods. Both images have been formed using the same imaging condition (equation 4.12) but different approximations in estimating the scattering Green's function (equation 4.15 for (a) and equation 4.17 for (b)). Panel (c) shows the difference between the images, calculated by subtracting panel (a) from panel (b).

4.6) which instead contributes noise to the image in Figure 4.7b. Nevertheless this example highlights some advantages of Marchenko imaging over standard RTM-style migration.

If we follow the same workflow as defined in the previous section for the model defined in Figure 4.1, but instead apply it to data from the model in Figure 4.6 we produce the three images shown in Figure 4.8. The image is targeted around the fault where the illumination using the surface seismic data in Figure 4.7 was insufficient to resolve the structural features of interest. It can be seen that VSP Marchenko imaging (Figure 4.8b) and standard Marchenko imaging (Figure 4.8c) are sensitive to different features marked by red and blue arrows respectively. Note that the middle blue arrow in Figure 4.8c is an error which is masking the true event which you can see emerges at around $(1200m, 950m)$. The result in figure 4.8b compared to 4.8c shows a clearer image of the fault in shallow areas, where primary reflections from the fault are measured at the surface, and illumination from the VSP deteriorates (due to increasing offset). Therefore when we combine the images (using the workflow defined above) we obtain an enhanced image (Figure 4.8d) which better resolves the subsurface features when compared to the alternative methods alone.

4.5 Discussion

A condition for the application of the subsurface source-receiver method presented in this chapter is the requirement for the virtual receiver ($\mathbf{x}_i$) to be above the virtual source ($\mathbf{x}_j$). When both of the input fields are Marchenko estimates, both the focusing and Green's functions can be calculated at every point, so these two terms are interchangeable and Green's functions can be calculated between any two points (Singh and Snieder, 2017a). However, in our examples it is the Green's function measured at the well location that contains the additional data in which

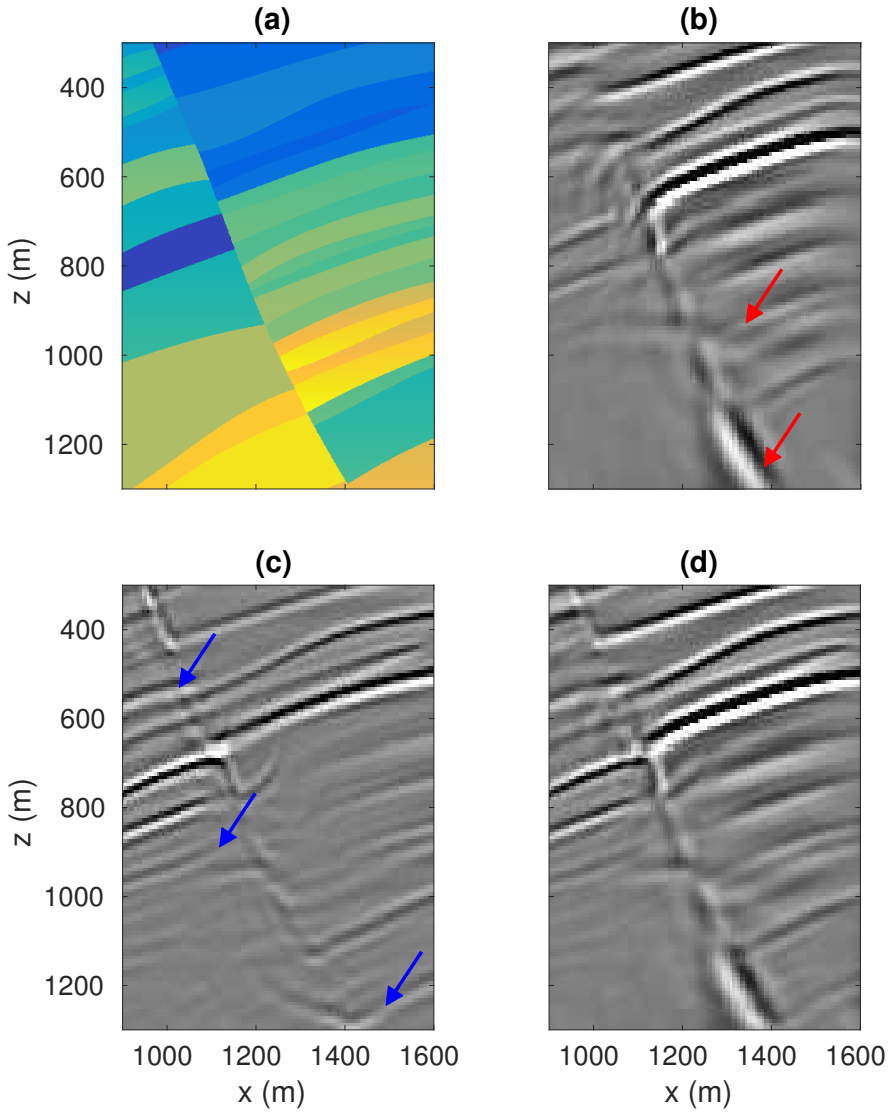

Figure 4.8: A comparison of images created using: (b) VSP Marchenko imaging, (c) standard Marchenko imaging and (d) combined VSP Marchenko imaging. The results presented in panels (b) and (c) are sensitive to different features so for comparison we have highlighted features unique to the result in panel (b) with red arrows and features unique to panel (c) with blue arrows. The true model from Figure 4.6 is given for comparison in panel (a).

we are interested. The Green's function is calculated between a surface point $\mathbf{x}_0$ and the virtual source position $\mathbf{x}_j$ at the well (the latter is therefore inflexible). As a result, we impose the condition on the depth co-ordinates $i < j$ and only place virtual receivers above the virtual source position. When we produced the images in this chapter we integrated over multiple VSP receiver positions $\mathbf{x}_j$, each with a different depth coordinate. However, we also integrated over the virtual receiver positions $\mathbf{x}_i$ and this number changes depending on the virtual source location. This leaves the images prone to bias in their amplitudes as near surface image points have a larger number of contributions. In our results we have applied a depth dependent weighting factor to account for these effects and this was implemented to produce the image in Figure 4.5. However, this will not undo the bias which will more accurately image near-surface reflectors rather than those in the deeper areas. If this was to be violated and the virtual receiver was below the VSP receivers the focusing term (f^+) would need to be calculated at the VSP receiver and the Green's function would need to be calculated using Marchenko methods at a depth level below this. However, this would forgo the advantages of using the real VSP measurements, and the results from equation 4.7 would be comparable to those that could be obtained when both of the input fields were calculated using Marchenko methods.

In Figure 4.7 we have applied standard Marchenko methods to the Marmousi2 model. The results show that Marchenko imaging improves on conventional RTM-style methods. However, this does not mean that Marchenko methods redatum Green's functions as accurately in this more complex model as we have demonstrated is possible in simple synthetic models (Figures 4.2 and 4.3). In Figure 4.9 we compare redatumed common virtual receiver gathers from two image point in the model given in Figure 4.6 $\mathbf{x}_i = (1300m, 400m)$ and $\mathbf{x}_i = (1000m, 1100m)$: the first is relatively shallow and above the fault, the second is deep and below the fault. If we compare the Marchenko Green's

functions with the modelled Green's functions there is a good match between Figure 4.9a and 4.9b, however this is not the case if we compare Figure 4.9c and 4.9d. This poor match can be attributed to difficulty in estimating accurate focusing functions beneath the fault, as the primary reflection from the fault, which is required to construct accurate focusing functions, is not measured at the surface. So although the results we have presented are promising, more in-depth analysis is required in future studies to ascertain how to improve these estimates.

The focus of this chapter has been on the inclusion of VSP data in the Marchenko method. However, it may be possible to use alternative signals to replace the Green's function term instead of the VSP data in equation 4.7 – for example micro-seismic signals. In this case the Green's functions are unlikely to be as numerous or as well distributed as for a VSP dataset. However, during testing for this chapter, images of the vertical interfaces could be obtained with relatively few VSP Green's functions. Furthermore, if the aim is not to produce an image but rather to estimate a wavefield, this would be possible with only one single Green's function from a subsurface source (assuming complimentary surface receivers and surface seismic reflection data are available).

We have focused on using the estimated Marchenko wavefield for imaging, but the VSP-Marchenko wavefields contain a significant amount of information to which we do not normally have access. It could be possible to exploit that information to invert for subsurface properties, rather than just to image. We have shown that the virtual-source to virtual-receiver Green's functions are accurate so this could be possible although the implications of using a smoothed reference model as input will need to be investigated.

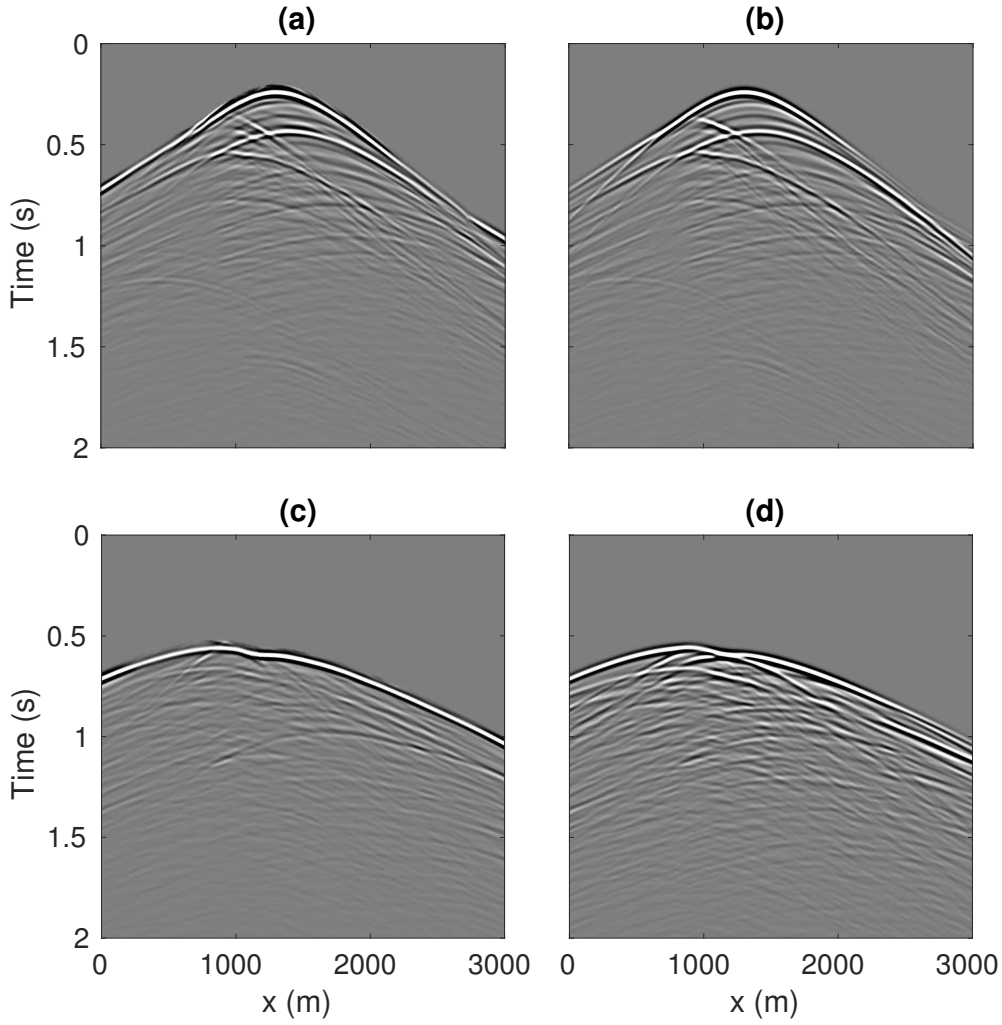

Figure 4.9: A comparison of Marchenko Green's functions (a and c) and modelled Green's functions (b and d). Panels (a) and (b) are calculated between the surface source array and a virtual receiver position at $\mathbf{x}_i = (1300m, 400m)$ in Figure 4.6. Panels (c) and (d) were calculated between the surface source array and point $\mathbf{x}_i = (1000m, 1100m)$.

4.6 Conclusion

We have presented a way to incorporate VSP data into the Marchenko method and Marchenko imaging. The output of this method is an estimate of the subsurface wavefield from a subsurface virtual source, which potentially contains a large amount of information about the properties of the Earth. In numerical examples we successfully used this wavefield to create images of two synthetic subsurface structures. These images contain reduced contamination due to internal multiples and include vertical features that standard Marchenko imaging and reverse time migration would otherwise struggle to identify.

4.7 Acknowledgements

The authors would like to thank Petrobras and Shell for their sponsorship of the International Centre for Carbonate Reservoirs (ICCR), and for permission to publish this work from the VSP project. We would also like to thank the fellow members of the ICCR and members of the Edinburgh Interferometry Project (EIP) for their numerous fruitful discussions. The data used within this chapter was generated with the Madagascar open-source software package freely available from **www.ahay.org**.

Chapter 5

Heaviside Marchenko Imaging

Angus Lomas[1], Satyan Singh[1] and Andrew Curtis[1,2]

In the preceding chapter we formulated a novel subsurface imaging method that accounts for internal multiples and creates images of vertical or near interfaces. However, the method we have formulated requires downhole seismic data, which is not always available and therefore restricts the application of this method to locations where such a dataset is available. In this chapter we approach the same problem, again we focus on creating images of vertical interfaces but alternatively we remove the requirement for downhole seismic data.

5.1 Introduction

In preparation for conventional migration-based seismic imaging algorithms, seismic data undergo significant pre-processing to remove all energy from the seismic

[1]School of GeoSciences, University of Edinburgh, Edinburgh, UK
[2]Institute of Geophysics, ETH Zurich, Zurich, Switzerland

record with the exception of singly-scattered components (primary reflections) of the seismic wavefield. The other components are usually removed because conventional imaging methods do not account for the more complex components of the seismic wavefield correctly, so for those methods multiply scattered waves constitute a source of noise in resulting images. However, there has recently been a shift in approach: the multiply-scattered components of seismic recordings contain a significant amount of additional information about the subsurface. It is therefore potentially beneficial to leave these components in the seismic record, providing we have imaging methods that are able to use them correctly. Examples of retaining such components include: the transmitted (non-reflected) waves in the seismic data can be used to improve Full Waveform Inversion (FWI) results (Pratt, 1999; Virieux and Operto, 2009), and multiply scattered seismic waves can be used to increase subsurface illumination (Malcolm *et al.*, 2009). In this chapter we aim to use duplex waves – wavefield components that have scattered twice within the subsurface of the Earth to create images. These signals are of particular interest because they predominately form in the presence of steeply dipping subsurface structures – features to which conventional imaging methods are usually insensitive.

Several methods have been suggested previously to use duplex waves to improve imaging of vertical interfaces. However, generally these methods have two major limitations: either they assume prior knowledge of the subsurface horizontal interfaces (Martin *et al.*, 2006; Davydenko and Verschuur, 2013) or they image only vertical interfaces (Jin *et al.*, 2006; Singh and Curtis, 2018). Alternatively, diving waves and two-way wave equation imaging methods can be used to create images of vertical interfaces, but these methods only use primary waves and will only work if the primary reflections from diving waves are measured at the surface which often required extremely long acquisition arrays. Alternative approaches have also been taken to image vertical interfaces by incorporating

Vertical Seismic Profile (VSP) data into the imaging method (Hornby and Yu, 2007; Lomas *et al.*, 2018) but both a borehole and an additional seismic dataset is required to implement such methods.

An ideal imaging method would use a single imaging algorithm to identify both vertical and horizontal interfaces using both primaries and duplex waves, without a borehole and with limited prior knowledge of the subsurface. In this chapter we offer a solution to this using a new method, so-called Heaviside imaging, which is an extension of work presented by Singh and Curtis (2018). We demonstrate the new method on three synthetic models: the first is a step model which provides an intuitive demonstration of the methodology. The second model is the more realistic *Amoco* model. The results from both of these tests are positive, however they are prone to imaging artifacts due to multiples. We therefore then extend the method to account for multiples by incorporating elements of the Marchenko method (Rose, 2001, 2002; Broggini *et al.*, 2012; Wapenaar *et al.*, 2013; Singh *et al.*, 2015; Lomas and Curtis, 2019) into the newly formed imaging method. This is demonstrated on a third model where the input seismic data contains strong internal and free-surface multiples but again positive results are achieved, this time using Heaviside Marchenko imaging.

5.2 Method

Claerbout (1971) proposed that subsurface reflectors can be mapped by applying imaging conditions to estimates of the upgoing and downgoing signals at subsurface image points in response to a source of seismic energy. Throughout this chapter we refer to upgoing waves ($-$) as wavefield components that are traveling towards a linear array of seismic sources at the observation point and downward signals ($+$) are traveling away from the same array. In all cases this source array is on or close to the surface of the Earth. An imaging condition is then used to

test the similarity of the up- and down-going waves travelling between the same source-observation point pair. The first component of the estimated downgoing signal at the image point is commonly the direct (non-scattered) component of the propagating wavefield. If the image point of interest is on a reflector, the first component of the upgoing signal at the image point will be the singly-scattered component of the wavefield from the local reflector. This will correlate temporally with the downgoing signal because the two have near-identical travel paths, given the upgoing component is estimated immediately after scattering. Therefore, if the similarity of these two signals is tested using an imaging condition, a relatively high value will be produced. However, as the image point moves away from the reflector the similarity of the upgoing and dowgoing signals diverges rapidly and the imaging condition produces a relatively low value. A map of the value of the imaging condtion therfore provides an approximate image of the medium. There were two forms of imaging condtion suggested by Claerbout (1971): the deconvolution and cross-correlation imaging conditions. Throughout this chapter we focus on cross-correlation. The imaging condition of interest can be written as (equivalent to equation 5 presented by Claerbout (1971)):

$$I(\mathbf{x}_i) = \int\limits_{\partial\mathbb{D}_0} d\mathbf{x}_s \int \left[U(\mathbf{x}_i, \mathbf{x}_s, t) D(\mathbf{x}_i, \mathbf{x}_s, t)\right] \, dt \tag{5.1}$$

We define I as our image and $\mathbf{x}_i$ is the location of the subsurface image point with coordinates (x, z). Equation 5.1 is given in the time domain (t) and is the multiplication of the downgoing signal (D) and upgoing signal (U) measured at the image point $(\mathbf{x}_i)$ in response to a source at point $\mathbf{x}_s$. The integral term is over the surface boundary $(\partial\mathbb{D}_0)$ which is composed of a finite array of source (and receiver) positions.

A limitation of the imaging condition given in equation 5.1 is the assumption

that a downward propagating wave interacts with a subsurface interface, reflects, becomes an upward propagating wave and does not scatter again. We are able to accurately image the subsurface by making this assumption because the Earth's subsurface geology is often composed of horizontal or sub-horizontal layers. However, when there is subsurface complexity (e.g. salt flanks), this assumption is inaccurate and with limited prior information the imaging condition given in equation 5.1 will not be able to map these features.

Recent work by Singh and Curtis (2018) has proposed an alternative imaging condition that enables vertical or sub-vertical subsurface features to be accurately mapped:

$$I(\mathbf{x}_i) = \frac{\partial^2}{\partial \mathbf{x}_i^2} \int_{\partial \mathbb{D}_0} d\mathbf{x}_s \int U(\mathbf{x}_i, \mathbf{x}_s, t)^2 \, dt \tag{5.2}$$

There are only two differences between equations 5.1 and 5.2: first, is the downgoing signal (D) has been replaced by the upgoing signal (U). This means that the imaging condition is now applied to two identical signals. This may appear counter-intuitive – we now test the similarity of the signal to itself, and of course the signal is going to be the same as itself everywhere and will therefore always produce a high value of the imaging condition. However, the second difference is the inclusion of the Laplacian operator ($\frac{\partial^2}{\partial \mathbf{x}_i^2}$) which acts as a high-pass filter; this modifies the imaging condition such that it becomes sensitive only to the spatial changes in the energy distribution of the signals. We provide an intuitive demonstration of this process in the following section. The original implementation of equation 5.2, so-called time reversed mirror imaging (TRMI), was shown to image vertical interfaces but to be insensitive to horizontal interfaces. Equations 5.1 and 5.2 therefore only image different subsurface features with accuracy (near horizontal and near vertical features,

respectively) and it was proposed that these two equations could be summed to form a single image.

Unfortunately since equations 5.1 uses primary reflections whereas equation 5.2 can be shown to only use multiply-scattered reflections (Singh and Curtis, 2018) their amplitudes are very different. If we sum the results obtained from equations 5.1 and 5.2, one of the two results needs to be multiplied by a weighting factor to match the amplitudes of the other, and the factor is always unknown and must be chosen subjectively. Therefore, here we propose an alternative imaging condition that incorporates the advantages of both equations 5.1 and 5.2 into a single imaging condition, enabling both vertical and horizontal structures to be imaged together. This imaging condition is defined as:

$$I(\mathbf{x}_i) = \frac{\partial^2}{\partial \mathbf{x}_i^2} \int_{\partial \mathbb{D}_0} d\mathbf{x}_s \int \underbrace{\left[H(t - \hat{t}(\mathbf{x}_i, \mathbf{x}_s))U(\mathbf{x}_i, \mathbf{x}_s, t)\right]^2}_{\textit{Figure 2}} \, dt \tag{5.3}$$

Equation 5.3 includes an additional Heaviside function $H(t-\hat{t}(\mathbf{x}_i, \mathbf{x}_s))$, which sets wavefield components in the upgoing signal U that travel faster than the direct wave between the source ($\mathbf{x}_s$) and the image point ($\mathbf{x}_i$) to zero, this travel time is denoted $\hat{t}$. This incorporates the source side information from equation 5.1 (that enables horizontal interfaces to be imaged) into equation 5.2, as well as reducing image noise from spurious cross-correlations.

In Figure 5.1 we present an intuitive illustration of the operation of the the imaging conditions presented in equations 5.1-5.3. In the first row of Figure 5.1, which represents equation 5.1, the forward propagated wavefield (the first column) is multiplied by the back propagated wavefield (the second column). Where the two wavefronts coincide in space there is a contribution to the image. Here we show a single time step but summing across all time forms an image of

the subsurface. Similarly the second row of Figure 5.1 illustrates the operation of equation 5.2. In this row the two back propagated wavefields are multiplied, and because two different wavefronts coincide in space at the vertical interface the resulting image identifies this feature. In the final two rows of Figure 5.1 we illustrate the operation of equation 5.3. The operation is identical to the first two columns but the forward propagated wavefield in the third row is replaced by a Heaviside function with a value of 1 behind the wavefront and 0 everywhere else. This enables two imaging conditions to operate simultaneously, these imaging conditions operate in the same way as those presented in the first two rows of the same figure. However, this is only possible by including the Heaviside source wavefield, rather than the standard wavefield from the first row, as this standard source wavefield will be equal to zero at the location of multiple scattering.

The imaging condition given in equation 5.3 is the main advancement proposed in this chapter. In the following sections we focus on its implementation, example applications and refinement.

5.3 Numerical Examples

5.3.1 Step Model

The first step in implementation of equations 5.1-5.3 is to estimate the upgoing (U) and downgoing (D) signals at an image point. In the first example this is achieved by implementing reverse time migration (RTM) methods (Baysal *et al.*, 1983). To do this we take the data $R(\mathbf{x}_r, \mathbf{x}_s, t)$ measured at a surface receiver ($\mathbf{x}_r$) in response to a surface source ($\mathbf{x}_s$) – $R(\mathbf{x}_r, \mathbf{x}_s, t)$ and reverse the seismic experiment. To do this we computationally back propagate the measured data from all receiver positions $\mathbf{x}_r$ simultaneously, through an estimated model of the subsurface velocity structure, to the image points ($\mathbf{x}_i$), thus producing an estimate

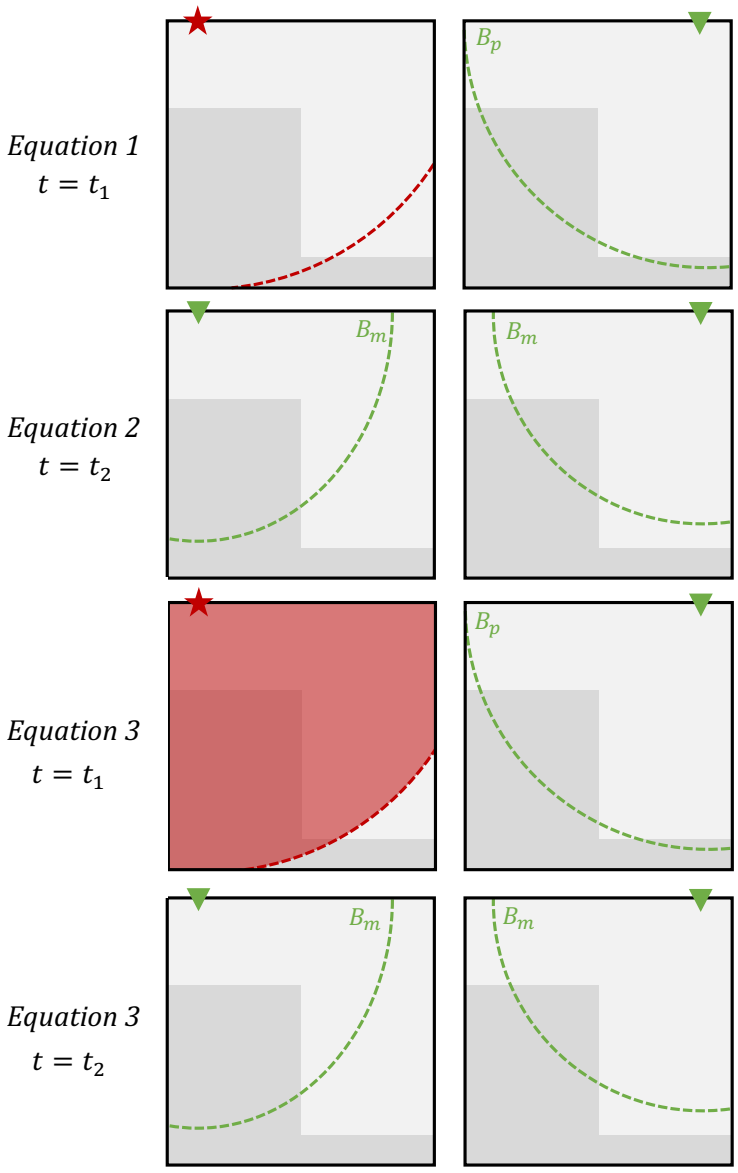

Figure 5.1: An illustration of the operation of the imaging conditions given in equations 5.1, 5.2 and 5.3. In each of the panels the green arc represents a single event from the measured (at the green triangle) wavefield back propagated in time. Likewise, the red wavefront is the forward propagated wavefront from the red star, the red wavefront in the third row is a Heaviside wavefront and is equal to 1 in the red area and zero elsewhere. The back propagated wavefronts are labeled as either a primary (B_p) or multiple (B_m), in all case the multiple is a duplex wave. All rows show a single time interval (t_1 or t_2) and the grey blocks represent layers of different densities.

of the upgoing field U at $\mathbf{x}_i$. To estimate the downgoing field D at $\mathbf{x}_i$ we forward propagate a source wavelet from the single source position $\mathbf{x}_s$ to the image point, again through an estimate of the subsurface velocity structure.

To demonstrate this process we use a synthetic subsurface model with a 'step' structure shown in Figure 5.2a. This model has variable density and a constant velocity ($2000m/s$). Just below the surface of this model at $z = 12m$ are 601 co-located sources and receivers at $4m$ horizontal intervals. A seismic reflection dataset is created from every source position to every receiver position and the injected source wavelet is a $25Hz$ Ricker wavelet. We use this data to form estimates of the upgoing and downoing signals as discussed in the preceeding paragraph and use these estimates to implement equations 5.1, 5.2 and 5.3, the results of which are given in Figures 5.2b, 5.2c and 5.2d respectively.

Figure 5.2 demonstrates that the newly formed imaging condition given in equation 5.3 is able to accurately map both vertical and horizontal interfaces given data collected on just one side of the medium (close to the surface of the Earth). This is not possible using the alternative imaging methods given in equations 5.1 and 5.2 alone – given in Figures 5.2b and 5.2c respectively.

Whilst the results shown in Figure 5.2 are positive it may not be clear how the imaging condition in equation 5.3 is operating. To provide more intuition, in Figure 5.3 we present a series of common image point gathers, these are the signals between a single subsurface image point and multiple surface sources. The gathers displayed correspond to equation 5.3 prior to integration over time and the boundary $\partial\mathbb{D}_0$, this component of the equation is highlighted and labeled. We have selected six image points in the medium and plotted the gathers for these points in Figures 5.3a-f; the points are labelled accordingly in Figure 5.2a. For each panel in Figure 5.3 we have included a number which is the value for $I(\mathbf{x}_i)$ prior to application of the Laplacian operator, and the signal components

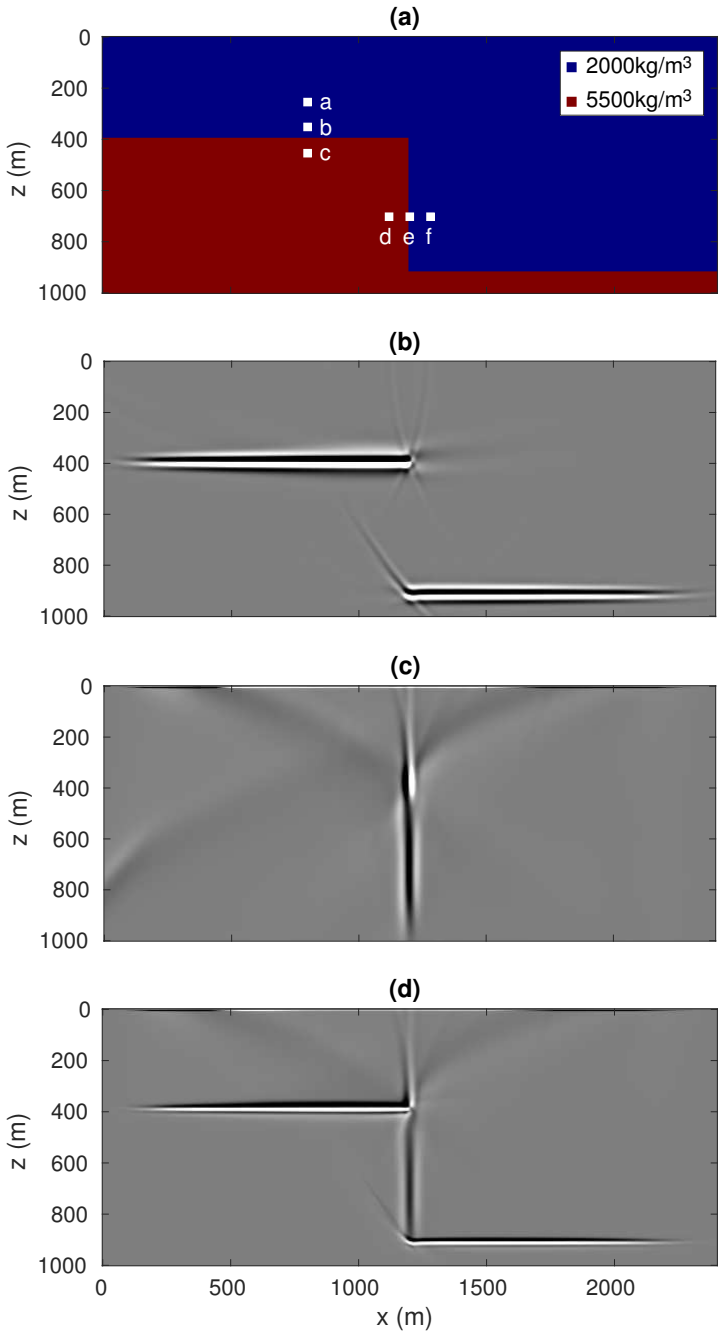

Figure 5.2: A comparison of the true subsurface model and the images produced using alternative imaging conditions. Panel (a) shows the true subsurface density model, panel (b) shows the RTM image produced by equation 5.1, panel (c) shows the TRMI image produced by equation 5.2 and panel (d) shows the result formed by the new imaging condition – Heaviside imaging in equation 5.3. The results in panels (b) and (c) have both previously been presented by Singh and Curtis (2018).

of interest are highlighted by dashed lines in the gathers.

In the first set of panels (a)-(c) in Figure 5.3 a single component of the gather is highlighted: the primary reflection from the interface at $z = 400m$. As the depth of the image point increases (see Figure 5.2a) the back extrapolated primary reflection arrives earlier in time. In panels (a) and (b) this signal arrives after the zeroing component of the Heaviside function from equation 5.3. In panel (c) this is not the case, which is to be expected as the image point is below the interface; the primary reflection is therefore muted to zero. Therefore, when we perform the integral from equation 5.3 there is a rapid loss in the total energy of the gather as the image point moves across the horizontal interface, quantified by the $I(\mathbf{x}_i)$ value in Figure 5.3. This feature is enhanced and then mapped by the inclusion of the Lapalcian operator to produce Figure 5.2d.

In the second set of panels (d)-(f) in Figure 5.3, two components of the gathers are highlighted: the back extrapolated primary reflection from the interface at $z = 900m$ and the back extrapolated duplex wave from the same horizontal interface and the vertical interface at $x = 1200m$. As the image point (see Figure 5.2a) moves towards the vertical interface the duplex and primary reflections converge and coincide in space and time; when the image point is on the vertical interface this causes a peak in the value for $I(\mathbf{x}_i)$. This peak allows the vertical interface to be mapped in the image shown in Figure 5.2d.

5.3.2 Amoco Model

To test Heaviside imaging in a more realistic subsurface setting we have taken a second synthetic subsurface model – a modified subsection of the *Amoco* model (Etgen and Regone, 1998). We have modified this model from the original by only using density contrasts (a constant velocity of $2000m/s$), this eliminates the requirement for refracted and diving wave removal. Furthermore, we have

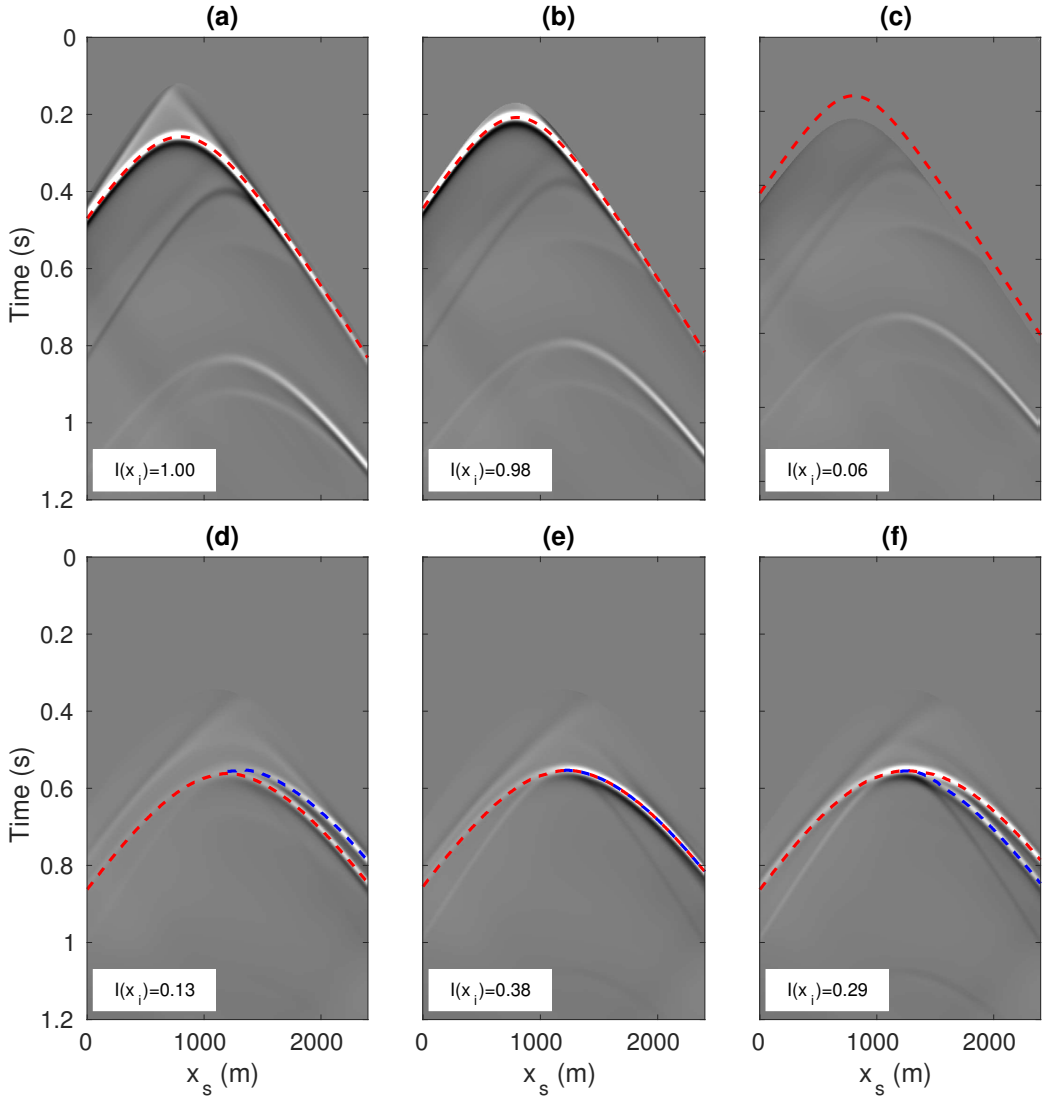

Figure 5.3: A comparison of the integrand components of equation 5.3 for a set of different image point locations and multiple fixed source locations (the *x-axis*). The locations of these image points are defined in Figure 5.2a. The value for $I(\mathbf{x}_i)$ is given **prior** to the operation of the Laplacian component of equation 5.3. In all panels the red dashed lines highlight back extrapolated primary reflections and the blue dashed lines highlight back extrapolated duplex reflections.

now included free-surface multiples in the input seismic data, as well as a high impedance boundary at the base of the model to encourage strong duplex waves – given in figure 5.4a. The seismic data was collected at a depth of $12m$ with co-located sources and receivers at $4m$ intervals. We have implemented RTM and Heaviside imaging from equations 5.1 and 5.3, and the results are given in Figures 5.4b and 5.4c respectively.

The results shown in Figure 5.4 demonstrate that RTM methods are unable to accurately image near vertical interfaces given the limited aperture in this seismic source/receiver array. However, using the same seismic data and the reformulated Heaviside imaging condition from equation 5.3 we are able to obtain improved results. Within the imaging condition two operations work in tandem. The first uses duplex waves and creates the events highlighted by red arrows, mapping interfaces at a longer wavelength when compared to the second operation shown by blue arrows, which uses the primary reflections. There is an issue with artifacts due to multiples however, highlighted in Figure 5.4c by green arrows. The multiples could be removed by pre-processing the seimic data, however Singh and Curtis (2018) showed that the TRMI imaging condition uses these to improve the imaging of the vertical interface. Therefore, in the following section we introduce a method that enables us to account for the multiples whilst retaining their contribution to the resulting image.

5.4 Heaviside Marchenko Imaging

Recent work has demonstrated that Marchenko methods (Wapenaar *et al.*, 2014; Singh *et al.*, 2016) are able to accurately compute directionally decomposed signals (Green's functions) between surface sources and subsurface image points whilst accounting for internal and free-surface multiples. This provides a method to more accurately estimate the upgoing signal U. We can therefore modify

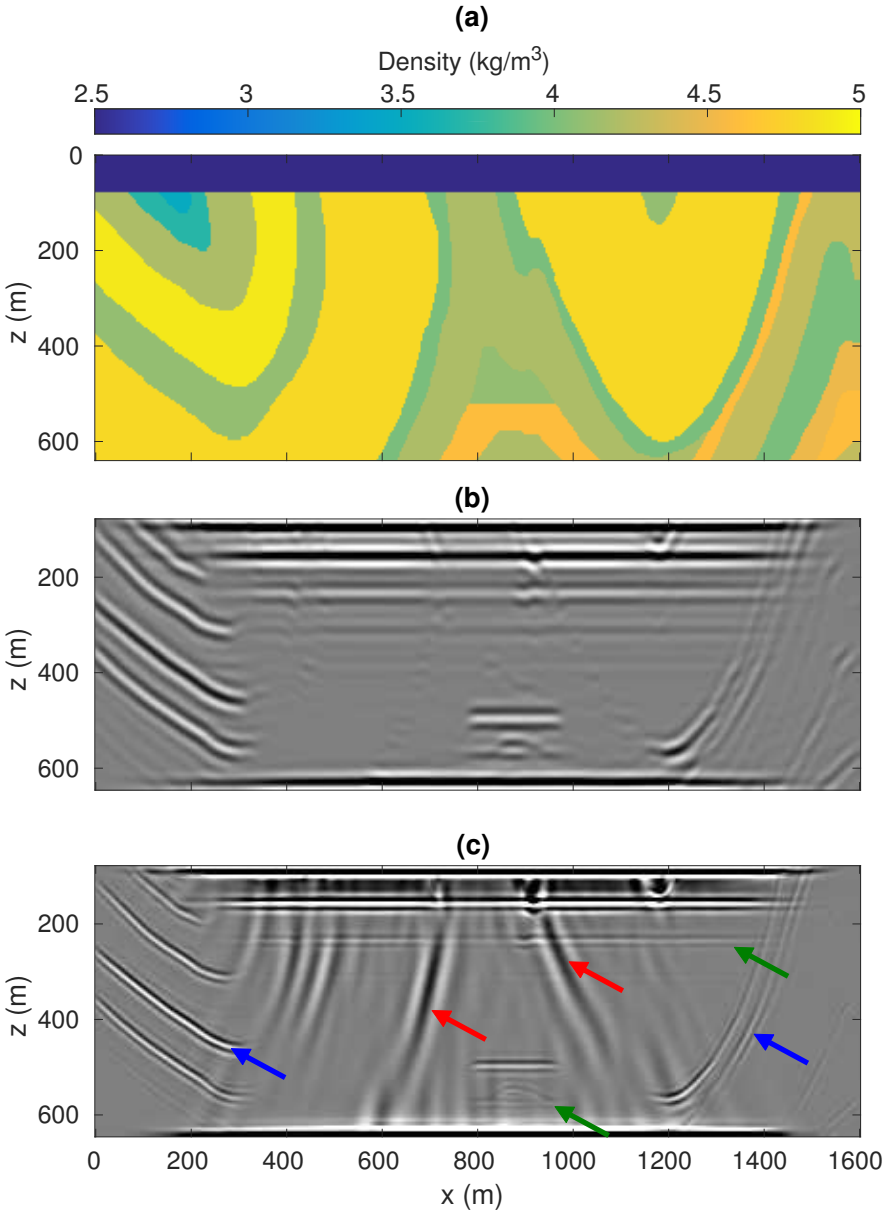

Figure 5.4: A comparison of images created using the imaging conditions defined in equations 5.1 and 5.3. Panel (a) shows the true subsurface density model, panel (b) shows the time reversed mirror imaging result produced by equation 5.2 and panel (c) shows the newly formed Heaviside imaging result produced by equation 5.3. The blue arrows highlight reflectors imaged with primary waves, red arrows highlight reflectors imaged with duplex waves, and green arrows indicate artifacts caused by multiples.

equation 5.3 to:

$$I(\mathbf{x}_i) = \frac{\partial^2}{\partial \mathbf{x}_i^2} \int\limits_{\partial \mathbb{D}_0} d\mathbf{x}_s \int \left[H(t - \hat{t}(\mathbf{x}_i, \mathbf{x}_s)) G^+(\mathbf{x}_i, \mathbf{x}_s, t) \right]^2 \, dt \tag{5.4}$$

The new term G^+ is the upgoing Green's function arriving at the image point calculated using (Singh *et al.*, 2016):

$$G^+(\mathbf{x}_i, \mathbf{x}_s, \omega) = \int\limits_{\partial \mathbb{D}_0} \left[R(\mathbf{x}_r, \mathbf{x}_s, \omega) f_1^+(\mathbf{x}_r, \mathbf{x}_i, \omega) \right.$$
$$\left. - rR(\mathbf{x}_r, \mathbf{x}_s, \omega) f_1^-(\mathbf{x}_r, \mathbf{x}_i, \omega) \right] d\mathbf{x}_r - f_1^-(\mathbf{x}_r, \mathbf{x}_i, \omega) \tag{5.5}$$

where $f_1^{+/-}$ are so-called focusing functions and are found using the iterative Marchenko method presented by (Wapenaar *et al.*, 2014), and r is the free surface reflection coefficient which we have set equal to -1. Note that for convenience of notation equation 5.5 is expressed in the frequency (ω) rather than the time domain. Whilst the output of equation 5.5 is of a similar form to U, it is calculated using a different methodology: the Green's functions are formed using a series of convolution steps, rather than using wavefield propagation as in the results presented in Figures 5.2 and 5.4. Therefore, for comparison purposes we can redefine the upgoing signal of interest as:

$$U(\mathbf{x}_i, \mathbf{x}_s, \omega) \approx \int\limits_{\partial \mathbb{D}_0} \left[R(\mathbf{x}_r, \mathbf{x}_s, \omega) G_0(\mathbf{x}_i, \mathbf{x}_r, \omega)^* \right] d\mathbf{x}_r \tag{5.6}$$

where G_0 is an estimate of the direct travel time of a delta function source

through a low-wavenumber, smoothly-varying estimate of the true subsurface velocity structure, and * denotes complex conjugation. We can then implement equations 5.5 and 5.6 to obtain G^+ and U, followed by equations 5.3 and 5.4 which form two new images. We show these two images, including a new synthetic subsurface model in Figure 5.5. The subsurface model presented in Figure 5.5a is a constant velocity ($2000m/s$) variable density medium. On the surface of this model ($z = 0m$) are 376 co-located sources and receivers at $8m$ intervals. The true model extends with no lateral variations for $750m$ in both directions beyond the edges of the section displayed in Figure 5.5a.

The synthetic model shown in Figure 5.5a was designed to encourage strong internal and free-surface multiples. Therefore, the resulting images for RTM and Heaviside imaging (Figures 5.5b and 5.5c) contain strong artifacts (false interfaces). However, this is not the case for the image in Figure 5.5d where we have implemented Marchenko Heaviside imaging (equations 5.4 and 5.5). By including the Marchenko Green's function we are able to place energy from multiples at the correct location in space and time, and as a result the images produced contain a reduction in multiple related artifacts, yet retain the benefits of Heaviside imaging for imaging vertical interfaces.

5.5 Discussion

Throughout this chapter we have used variable density constant velocity synthetic subsurface models. We have used constant velocity media to remove the requirement for refracted wave removal, which will be a significant source of noise in Heaviside imaging. In real data applications these components of the seismic record will require careful removal. Furthermore, we showed in Figure 5.4 that the mapped waveforms are inconsistent; this is attributed to the operation of the imaging condition. However, it is possible that these effects could be minimised

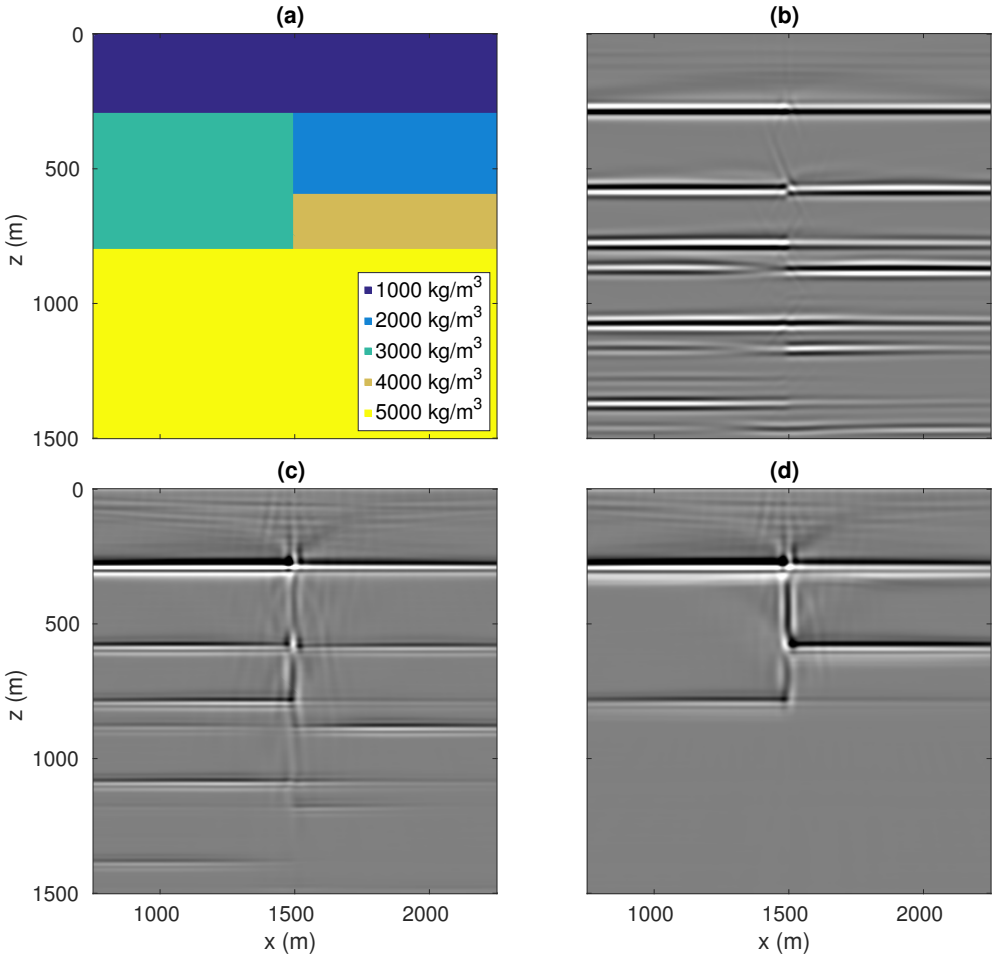

Figure 5.5: A comparison of images assessing the implications of multiples on the imaging condition defined in equation 5.1, 5.3 and 5.4. Panel (a) is the true subsurface density model, panel (b) is the imaging result using conventional imaging methods from equation 5.1 and 5.6, panel (c) is the image produced using Heaviside imaging from equation 5.3, and panel (d) is the Heaviside Marchenko imaging result from equation 5.4.

by deconvolving one of the back extrapolated wavefields (U) in equation 5.3.

Nevertheless, we have demonstrated that Heaviside imaging may prove beneficial in the interpretation of complex subsurface structures where there are steeply dipping interfaces (e.g. salt flanks, faults). Furthermore, the computation cost of implementing Heaviside imaging in addition to the computational cost of RTM (or in the latter example, Marchenko imaging) is negligible. Therefore, there appears to be no downside to creating complimentary Heaviside imaging results to aid subsurface interpretation.

The final example we present exploits the advantage of Marchenko methods to account for the effects of multiples in imaging results. However, at the time of writing there are considerations that need to be made regarding the practicalities of implementing Marchenko methods to real seismic datasets (da Costa Filho *et al.*, 2018). Likewise the tests that we have provided for Heaviside imaging are limited to synthetic datasets. It is therefore of scientific interest and a direction of future research to extend these methods to real seismic data.

5.6 Conclusion

The approach that we have presented in this chapter, so-called Heaviside imaging is a method that is able to use both duplex and primary wavefield components to improve the accuracy of images of a subsurface containing both vertical and horizontal interfaces. We have demonstrated this methodology on three synthetic subsurface models: the first is a simple step model, the second is the geometrically more realistic *Amoco* model, and finally a model designed to emphasis the impact of multiples – a known limitation of standard imaging methods. In all cases the Heaviside imaging method is beneficial over standard methods producing more accurate images of the subsurface. We have also formulated an extension of this

method, so-called Heaviside Marchenko imaging that produces imaging results with greatly reduced multiple contamination. Whilst the proposed methodology will not be beneficial in all situations (only when the input seismic data contains strong duplex waves) it may offer additional information about the structure of the subsurface at negligible additional computational if already implementing alternative imaging methods (i.e. RTM or Marchenko imaging).

5.7 Acknowledgments

The authors would like to thank Petrobras and Shell for their sponsorship of the International Centre for Carbonate Reservoirs (ICCR), and for permission to publish this work from the VSP project. We would also like to thank Dominic Cummings for numerous fruitful discussions and Stephanie Earp for help modelling the seismic wavefields. The numerical examples in this paper are generated with the Madagascar open-source software package freely available from **http://www.ahay.org** and the finite difference package in Thorbecke and Draganov (2011).

Chapter 6

Discussion

Within each of the preceding chapters we have raised key points of discussion. In this chapter we focus on broader topics, and we consider the practicalities for real world applications of the methods we have presented and some additional observations regarding the way we approach seismic imaging problems.

6.1 3D Plane-wave Marchenko Imaging

In Chapter 3 of this thesis we explored the implications of moving from two-dimensional Marchenko methods (currently the standard dimension of implementation) to three-dimensions. Our results showed that it is possible, and more accurate, to implement Marchenko methods in three-dimensions, but the associated computational cost of using three-dimensional data is significant, increasing by several orders of magnitude when compared to two-dimensional Marchenko methods. There are two reasons for this increase: first, the size of the dataset required for implementation is larger so the operations in equations 3.3-3.8 take

longer to execute. The second difference is the size of the medium – in three dimensions the number of image points increases by the size of the third dimension. For this reason the results presented in Figure 3.7 are limited to two-dimensional slices of the subsurface. We therefore have two obvious options for reducing the computational cost of Marchenko imaging in three-dimensions: either reduce the size of the data or reduce the number of image point calculations. We demonstrated in Figure 3.8 that reducing the size (spatial sampling) of the input seismic data can cause Marchenko methods to fail. However, recent work by Meles *et al.* (2018) has suggested a method to reduce the number of image point calculations, and therefore facilitate accelerated three-dimensional Marchenko imaging.

This new method replaces a point source Green's functions with a plane wave source Green's function. The equation that governs this has a similar form to those presented previously (equation 3.14):

$$I_{PMI}(\mathbf{x}_i) = \sum_{\mathbf{x}_0} \sum_{t} T_d(\mathbf{x}_0, \mathbf{x}_i, t)\, G_p^+(\mathbf{x}_0, z_i, t) \tag{6.1}$$

where

$$G_p^+(\mathbf{x}_0, z_i, t) = \iint\limits_{\partial\mathbb{D}_i} G^+(\mathbf{x}_0, \mathbf{x}_i, t)\; dx_i\; dy_i \tag{6.2}$$

where G_p^+ is the downgoing Green's function measured at the surface receiver positions ($\mathbf{x}_0$) in response to a plane wave source injected at the depth level z_i. For consistency of notation we have written this in a similar form to the equations presented ealier this thesis (more specifically chapter 2). The integral in equation 6.2 over the boundary $\partial\mathbb{D}_i$ removes the x_i and y_i components from the point $\mathbf{x}_i = (x_i, y_i, z_i)$ making G_p^+ only spatially variant with depth (z). However, these

two equations are equivalent to, and of a similar form to, equations 14 and 8 presented by Meles *et al.* (2018).

Throughout this thesis we have solved for a set of spatially varying (x, y and z) Green's functions using equations 3.3 and 3.4. However, Meles *et al.* (2018) showed that the same equations (as well as the preceding equations for focusing function calculation) hold when the point source is changed to a line source (in two-dimensions, equivalent to a surface source in three-dimensions). This means we can use an estimate of the transmission response from a source at the image point that only varies with depth to retrieve accurate plane-wave Green's functions (G_p). The resulting Green's functions are spatially invariant in the x and y dimension, reducing the number of calculations required for three-dimensional Marchenko imaging and therefore also reducing the computational cost. This means the number of Green's function calculations required can be reduced from $nx \times ny \times nz$ to simply nz, for the example presented in Figure 3.7 this equates to a reduction from $18,969,576$ to 201. The imaging condition given in equation 6.1 is still implemented in three-dimensions but the computational cost of this is negligible when compared to the cost of estimating the Green's functions. We have therefore implemented three-dimensional plane-wave Marchenko imaging for the model in Figure 3.7, the results are given in Figure 6.1.

The results in Figure 6.1 show that we are able to image the three-dimensional subsurface using plane-wave Marchenko imaging. The subsurface interfaces are all identified and there is no evidence of contamination in the image due to multiples. However, there are artifacts that contaminate the image, the most significant of which can be seen below the deepest layer ($z > 1550m$) in Figure 6.1a and 6.1c. Furthermore, in Figure 6.1c there is phase mismatch between the imaged interface of the steeply dipping flanks of the trough structure and the basement

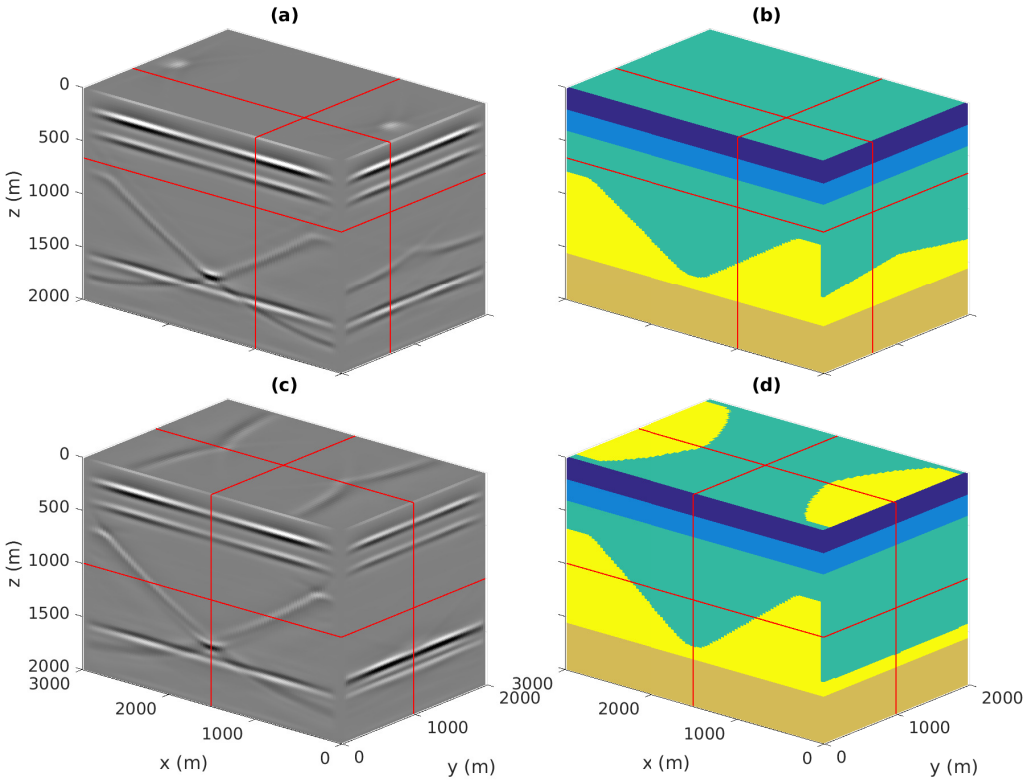

Figure 6.1: The results of three-dimensional plane wave Marchenko imaging. In panels (a) and (c) we project two-dimensional slices onto the sides of a three-dimensional cuboid: the projected slices are those indicated by the red lines. For comparison purposes the true model is given in panels (b) and (d), this is identical to the model presented in Figure 3.3.

of the same structure. Neither of these errors were observed in the full three-dimensional Marchenko imaging result we presented in Figure 3.7. Therefore, these effects can be attributed to the use of plane wave Green's functions rather than than the original point source Green's functions. It is not surprising that such effects are present in the results: a plane-wave source is one-dimensional and therefore has diminished sensitivity to two- or three-dimensional structures. However, a solution to overcome this problem suggested by Meles *et al.* (2018) is that the horizontally invariant plane-wave source can be replaced by an angled plane-wave. The resulting plane-wave Green's function will then be sensitive to dipping geological structure of the corresponding angle.

We have shown that the three-dimensional imaging results offered by plane-wave Marchenko image are not perfect, however it does offer significant advantages in terms of computation cost when compared to the alternative method, in this case a reduction by a factor of $\sim 10^5$ If internal multiples hamper interpretation, plane-wave Marchenko imaging may offer an efficient solution which could aid seismic interpretation or could be used in combination with target-orientated point source Marchenko imaging (Meles *et al.*, 2018).

6.2 Errors in Marchenko Redatuming

The underlying theory of Marchenko methods assumes that the surface sources and receivers completely cover the boundary $\partial\mathbb{D}_0$ to infinity in all dimensions. This is impossible in practice and within this thesis we have assumed a limited aperture for all seismic datasets. However, generally this assumption does not compromise the quality of the results when using limited aperture seismic data, providing the structures in the subsurface are not steeply dipping and the focusing location is not directly beneath the extremities of the survey. In both chapters 4 and 5 we have challenged this approximation by introducing vertical and near

vertical interfaces. In the aforementioned chapters our goal was to construct and image and we only briefly considered the accuracy of the focusing and Green's functions calculated using Marchenko methods when we have limited aperture and steeply dipping structures. Whilst we have shown accurate Green's functions estimation throughout this thesis, it is possible that there are areas of the subsurface where their accuracy deteriorates, in this section we investigate the location and cause of these errors.

Let us take the example presented in Figure 4.1 where we estimated Green's functions using Marchenko methods around a simple vertical structure. We can use this model to test the accuracy of Marchenko methods by comparing estimated Green's functions with the true Green's functions. We can in turn use this to identify locations where Marchenko methods are prone to errors. The results are given in Figure 6.2 where we compare a section of the subsurface model with the percentage error calculated using:

$$error = \frac{|G_{TRUE} - G_{MAR}|}{|G_{TRUE}|} \tag{6.3}$$

where $|G|$ densotes the l_1-norm of the vector G. The results in Figure 6.2b show that the largest errors in Marchenko Green's function estimation occur near subsurface interfaces. Let us first consider the vertical interface at $x = 1000m$. Unsurprisingly there is a gradual increase in the error at locations increasingly close to this interface. This is because the Marchenko method does not have the information (measured primaries) required to reconstruct all of the wavefield components that have interacted with the vertical interface (Ravasi, 2017). However, these features are not as detrimental to the results as expected and in the cross section shown in panel (d) the error at the interface is only around 5% higher than the background error.

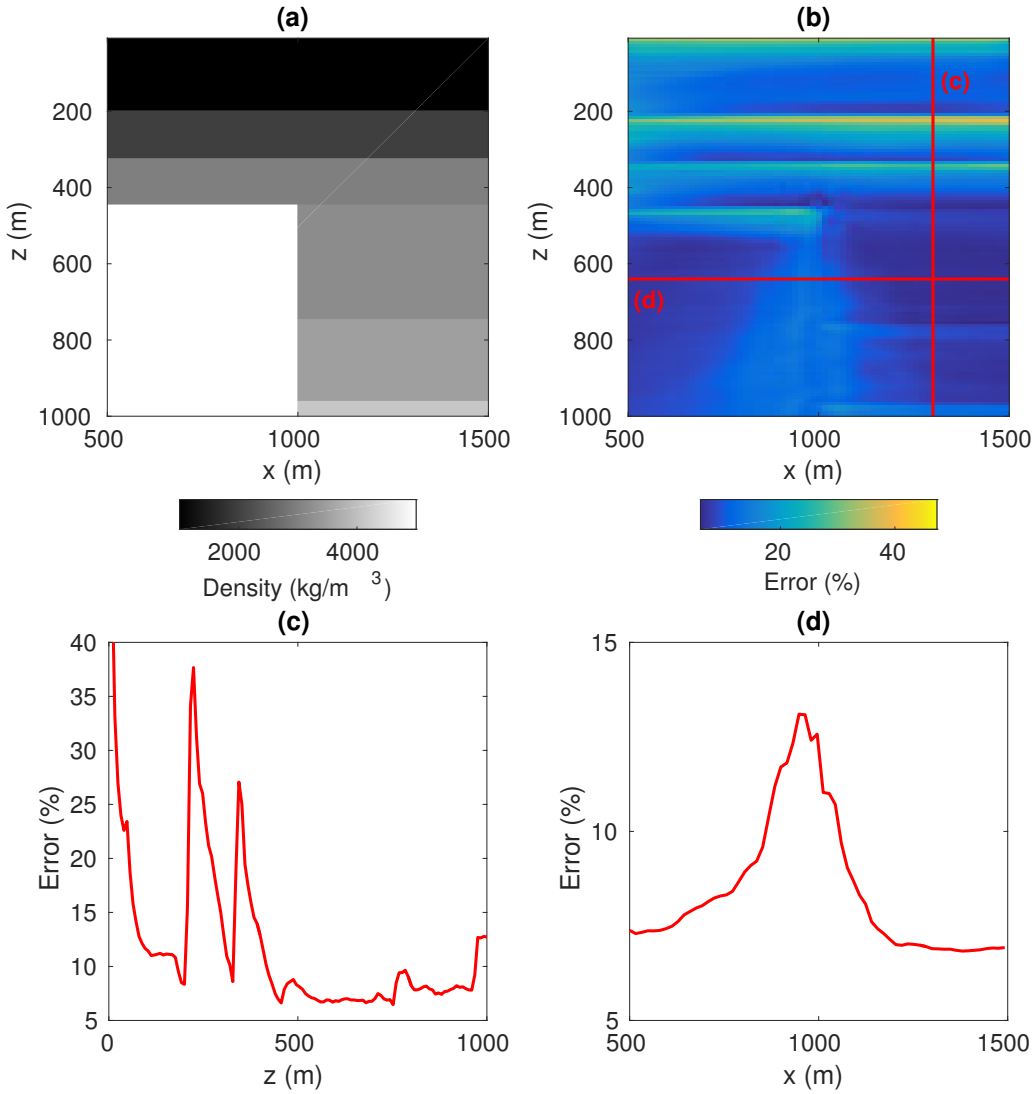

Figure 6.2: Analysis of errors in Marchenko Green's function estimation. Panel (a) is the true subsurface density model, and panel (b) is the error in the estimated Green's function for this model compared to the true modelled Green's functions. In panels (c) and (d) we compare two error profiles indicated by the red lines in panel (b).

The most significant errors in Figure 6.2b are just below horizontal subsurface interfaces. The significance of these errors decreases with depth, however they peak at ∼40% (Figure 6.2c), significantly higher than the background error of ∼7%. The most likely source of these errors is the inability of Marchenko methods to discriminate the focusing and Green's function components from one another in the time domain by simple time windowing:

$$\begin{aligned} \theta(\mathbf{x}_i, \mathbf{x}_0, t) G(\mathbf{x}_i, \mathbf{x}_0, t) &= 0 \\ \Psi(\mathbf{x}_0, \mathbf{x}_i, t) \left[f_1(\mathbf{x}_0, \mathbf{x}_i, t) - f_0^+(\mathbf{x}_0, \mathbf{x}_i, t) \right] &= 0 \end{aligned} \tag{6.4}$$

where θ is defined in equation 3.9 and Ψ is equal to:

$$\Psi(\mathbf{x}_i, \mathbf{x}_0, t) = 1 - \theta(\mathbf{x}_0, \mathbf{x}_i, t) \tag{6.5}$$

However, with band-limited seismic data this separation is impossible directly below interfaces. The size of the errors is more significant at low frequencies and methods to reduce these errors warrants further research. Furthermore, it is worth considering the implications of these errors when implementing Marchenko redatuming. When selecting a subsurface boundary to which we wish to redatum, these errors should be considered and such boundaries should perhaps best be placed above subsurface interfaces.

6.3 Marchenko Methods – Opportunities for Further Research

A limitation of the work within this thesis is that all of the examples we have presented are based on synthetic seismic datasets. It is therefore of significant

scientific interest to extend the methods we have presented to real seismic data. However, at the stages of methodological development in this thesis, for quality control purposes we required the use of the true clean synthetic seismic data for testing purposes. This allowed us to bypass some of the pre-processing that would be required for real seismic data. Significant advances have recently been made in applying Marchenko methods to real seismic data (Ravasi *et al.*, 2016; Jia *et al.*, 2018; Brackenhoff *et al.*, 2018; Staring *et al.*, 2018), but ins some cases the imaging results of these tests are inconclusive. Therefore, there remains concerns regarding the robustness of Marchenko methods when applied to real seismic data. It appears likely that significant Marchenko method-dependent pre-processing is going to be required to obtain optimal solutions. A thorough analysis of errors (e.g. due to incorrect velocity models, or source signature deconvolution) would also help to alleviate some of these concerns.

There are however issues that require further investigation and provided opportunities for further research. In the following subsections I highlight three of these, which I consider to be the most significant when applying Marchenko methods to real seismic data. They are: the impact of noise within the seismic data, Marchenko scaling factors, and the implications of applying acoustic imaging methods in viscoelastic media. While the strict requirements imposed on acquisition geometries is often quoted as a limitation of Marchenko methods, it appears likely that data interpolation and regularisation will offer a solution to this. Furthermore, there are alternative implementations for Marchenko methods which do not have the same strict acquisition geometry requirements (Ravasi, 2017).

6.3.1 Seismic Noise

One concern surrounding the application of Marchenko methods to real seismic data is the impact that noise in the input seismic data will have on the results. Quantifying the effect of noise is difficult because noise can manifest itself in a

variety of different ways. Let us consider the acoustic case, in which seismic noise can be classified as anything that the method cannot correctly process - anything other than P-wave reflections. Random perturbations in amplitude (incoherent noise) are unlikely to pose a significant problem given that they will stack out and cancel during any multi-dimensional convolution steps. A much more pressing concern is the presence of coherent noise in the seismic data.

Unfortunately there is a limited amount of existing research on this topic. Nevertheless, this is a problem that has been considered by da Costa Filho *et al.* (2015, 2018), here S-waves were present during the implementation of acoustic Marchenko methods for synthetic and real data respectively. The results attributed contamination and reduced accuracy of estimated Marchenko Green's functions to this noise, which makes sense as they will cause spurious cross-correlations in the formation of the Marchenko Green's functions. I would expect similar effects to appear when any form of coherent noise is present in the seismic data, therefore careful noise removal will be required to optimise results.

6.3.2 Scaling Factors

In chapter 3 we commented on scaling factors and their role in the implementation of Marchenko methods. In order for Marchenko methods to converge to accurate focusing functions the amplitude of the input reflectivity needs to be 'correct'. However, for synthetic experiments we often use perfectly scaled wave propagation codes which allows this problem to be ignored. However, this is not an option for real data applications. It has been suggested (Thomsen, 2016) that if borehole data are available this can be calculated easily. In this case the true Green's function is available and the misfit between the true and Marchenko Green's functions will be minimised by the optimal scaling factor. Undoubtedly, this would be the most accurate solution to the scaling problem but in most cases a downhole seismic dataset is not available and alternative solutions need to be

applied.

The first application of Marchenko methods to real data was by Ravasi *et al.* (2016). The scaling problem was highlighted, but it was overcome by analysing the energy change of the downgoing focusing term. For incorrect scaling factors the energy in this term will either converge to zero or diverge away from the initial value rapidly. The results from this method positive but they were inexact and subjective, with many solutions meeting the critera described above. A more quantitative solution was suggested by van der Neut *et al.* (2015c) where it was proposed that the total energy in the upgoing Marchenko Green's functions at the first iteration should be higher than the energy in the last iteration. This makes sense because, as we discussed in chapter 2, beyond the first iteration the Marchenko method should only cancel events, thus decreasing the total energy. This method refereed to as the so-called 'j-curve' method: the following which function should be minimized for the optimal value a:

$$j(a) = \frac{||G^{-}(\mathbf{x}_i, \mathbf{x}_0, t)||}{||G_0^{-}(\mathbf{x}_i, \mathbf{x}_0, t)||} \tag{6.6}$$

here $||.||$ denotes the l_2-norm. The factor a is used within the Marchenko Green's estimation workflow by replacing the seimic dataset R with the seimic dataset aR (see chapters 2 and 3), and it is independent of the image point $\mathbf{x}_i$ and therefore only needs to be calculated once for a single seismic dataset. The results for synthetic data were shown to be successful (Brackenhoff, 2016); however da Costa Filho *et al.* (2018) applied the 'j-curve' method to real ultrasonic data and it was not successful. This was attributed to the additional complexity (e.g. elastic waves, noise, non-ideal acquisition geometries) of real data. Therefore, whilst there are solutions to this problem they are not guaranteed to be successful when applied to real data; this is an area that warrants further research. The

solution to this problem has to be data-driven (calculated using the seismic data) but inevitably if there are components within the seismic data that the methods cannot correctly process (i.e. noise) then the accuracy of the methods could be comprised. I think it is likely that the solutions to this problem are never going to be exact and are always going to be a potential source of error in the resulting estimates of Marchenko Green's functions.

6.3.3 Viscoelastic Media

Throughout this thesis we have assumed the subsurface to be acoustic, so the methods we have presented do not account for dissipation, anisotropy, dispersion or elastic waves. Marchenko methods are very sensitive to amplitude variations and therefore any discrepancies in amplitudes due to the effects of dissipation will be detrimental to the outputs. Commonly in pre-processing flows, seismic data will undergo amplitude corrections to account for these effects; and these will be essential for workflows incorporating Marchenko methods but there are no studies quantifying the required accuracy of such steps. Furthermore, methods have been suggested that use Marchenko methods to calculate dissipation factors (Slob, 2016; Cui *et al.*, 2018a). However, these assume two-sided boundary measurements and tests have been limited to one-dimensional data.

Marchenko methods ideally require a deconvolved reflection response, as we showed in Figure 2.6. Realistically it is impossible to obtain this: problems with ghost-notching, energy dissipation and estimating the source signature will all prohibit our ability to obtain a perfect deconvolution (Ikelle and Amundsen, 2005). Methods have been suggested to exploit this feature of Marchenko methods in order to invert for a source-signature (Mildner *et al.*, 2017). However, this method is image point dependent and therefore will not be suitable for every point in the subsurface. For real seismic data obtaining the ideal deconvolved data is always going to be problematic, therefore in practice the number of iterations

should be limited to restrict spurious effects in the outputs.

6.4 Can We Improve The Way We Interpret Seismic Data?

The primary application of seismic imaging is for subsurface exploration. Here seismic imaging is one component of the workflow that aims to understand the subsurface geology in order to predict the location and size of subsurface fluid accumulations (e.g. hydrocarbon reservoirs, CO_2 storage). It is important to develop accurate imaging algorithms because this reduces uncertainty in geological interpretations and therefore potential errors in quantifying the properties of subsurface accumulations. However, every segment of this workflow requires specialists knowledge to achieve optimal results: a specialist will build the image of the subsurface which in turn will be passed onto another specialist to interpret and develop an understanding of the subsurface geology. A significant amount of effort goes into creating these images and, as we have shown in this thesis, we are able to generate a lot of information about the interactions of the seismic wavefield with the subsurface geology prior to forming the image. However, this image could be described as the 'bottleneck' of the workflow. A significant amount of information (the understanding of the seismic wavefield) is compacted into a single image which is then used to develop detailed understanding of the subsurface geology. The dependency on a single image appears to be a significantly limiting factor and a potentially large source of error in this workflow. Nevertheless, in standard workflows it remains inflexible that the output of the seismic imaging process is a single image of the subsurface.

In Figure 4.4 we demonstrated it was possible to accurately estimate wavefield propagation through the subsurface using just downhole and surface seismic data. We then used this information to create an image of the subsurface, given

in Figure 4.5. However, the wavefield we produced in Figure 4.4 undoubtedly contains more information about the subsurface than the image from Figure 4.5, but as already discussed, it is the image that is the preferred final output of the seismic processing flow. It is understandable that there is a preference for a singular image to interpret the seismic images we produce and develop an understanding of the subsurface geology. However, it is less understandable that we are willing to discard the wavefield that is produced as a bi-product of the processing flow which may contain additional information and that could be used to enhance our understanding of the subsurface geology.

In chapter 5 we have developed a new imaging method, so-called Heaviside imaging. The results we have presented showed this method is capable of producing improved images when compared to conventional methods, however it is clear that this method is only going to outperform conventional methods (e.g. RTM) in localised areas of the subsurface where strong duplex waves are present in the measured seismic data. In some cases it will provide a second image with additional information about the subsurface at negligible additional computational cost. While it is unconventional to obtain two images of the subsurface, if we are open to using both in the exploration workflow, and the advantages of each image were communicated carefully, errors in the final geological interpretation could be reduced.

It appears that as technology continues to develop and we change our approach to seismic imaging problems, the emphasis on creating a singular seismic image is somewhat inflexible. Perhaps if the exploration workflow was approached with more flexibility the physics of the seismic imaging problem could be better integrated, and thus uncertainty in geological interpretation and quantification of the properties of subsurface reservoirs could be reduced.

Chapter 7

Conclusion

The aim of this thesis is to develop techniques that improve the performance of imaging algorithms when multiply scattered components of the wavefield are present within the observed seismic data. Usually these components of the wavefield would be removed, using a variety of (imperfect) processing techniques. However, that is not the ideal solution. Ideally these components of the wavefield should be accurately accounted for within the imaging algorithm and/or used within the imaging algorithm to contribute to the final imaging result. In this thesis we propose novel methods that employ both of these approaches and demonstrate their potential on a range of synthetic datasets.

In chapter 2 we provide an intuitive introduction and demonstration of the operation of Marchenko methods. We demonstrated their applicability and accuracy for both one-dimensional and two-dimensional redatuming and imaging problems. Accompanying this chapter is a MATLAB code (discussed in chapter 2 and included in appendix B) which can be used to recreate many of the figures from this chapter. This also provides readers with further insight into the implementation of Marchenko methods. The accompanying code is the basis

of work in the subsequent chapters, so with some modifications many of the results within this thesis are reproducible.

Prior to undertaking the research within this thesis the application of Marchenko methods had been limited to two-dimensional seismic data. In chapter 3 we investigate and apply Marchenko methods to three-dimensional synthetic seismic data. First we show that the same relationships hold in three dimensions as they do in two dimensions – provided that seismic data with full areal coverage is available. However, given that it is more common to collect seismic data using linear (two-dimensional) arrays of sources and receivers we also considered the impact of three-dimensional propagation effects and structures on the results of two-dimensional Marchenko methods. We show that correction factors can account for some of these effects but out-of-plane events remain a problem in cases where there is insufficient data coverage.

In chapter 4 we investigate the inclusion of additional observations from downhole seismic data into Marchenko methods. This is not a completely novel direction of research, but previous studies have focussed on using downhole seismic data as an additional control on the direct waves (non-scattered) for standard Marchenko methods. As an alternative we focus on incorporating all of the wavefield observations from the borehole into the results, including scattered waves. We use the reflections from vertical and near vertical interfaces exclusively observed in the borehole data and incorporated this information into virtual source-virtual receiver Marchenko methods. We demonstrate that including the borehole data facilitates construction of wavefield components to which conventional Marchenko methods alone are insensitive. We then formulate an imaging condition that uses this new information, and as a result we were able to obtain images that resolve both vertical and horizontal subsurface interfaces whilst also accounting for internal multiples in the overburden.

The final set of results we present in chapter 5 followed a similar theme to the previous chapter. Here we investigate methods to image vertical or near vertical interfaces, but we remove the additional constraint of downhole seismic data. We reformulate the imaging conditions that are usually applied so alternatively, both primary and multiply scattered waves contribute to the resulting image. Using our new method, called Heaviside imaging, we demonstrate that we are able to create images using both singly and multiply scattered waves. Furthermore, we extend this method to include elements of Marchenko methods (from chapters 2, 3 and 4), which enable us to reduce multiple related artifacts in the resulting images. However, this method is dependent on the presence of strong duplex waves, therefore its application will only be advantageous when certain geological features such as salt flanks or faults are present in the subsurface.

In chapter 6 of this thesis we outline some of the unresolved issues in the implemention of Marchenko methods. The issues focus on real data applications and they include, but are not limited to: computational cost, seismic noise, scaling factors and realistic media. Due to such issues, many of the existing real data examples of Marchenko methods have produced inconclusive results. However, it has been thoroughly demonstrated that these methods have the potential to alleviate some of outstanding issues in seismic imaging problems and therefore they warrant continued research.

The idea of turning what is often viewed as noise (multiples) into signal is an appealing prospect, particularly in locations where multiples provide additional information about the subsurface. Even if using multiples is not possible, accurately accounting for them remains an unresolved issue. In this thesis we propose a range of solutions to address these issues, all of which enhance imaging results of the subsurface. Moreover, the word noise is a misleading term when used to describe multiples (and many other components of the signal which we commonly view as noise): more precisely they are not noise, but wavefield

components that conventional imaging algorithms are unable to process.

Appendix A

Solving for Marchenko Focusing Functions

In Chapter 2 we introduced a method which solves for Marchenko focusing functions and we provided a schematic demonstration in Figure 2.3 and 2.4 of how this procedure operates. Alternatively this procedure can be derived mathematically following the notation and method suggested by van der Neut *et al.* (2015b). The starting point for this is equations 2.7 and 2.6 which can be written in matrix form as:

$$\mathbf{f}_K^- = \boldsymbol{\Theta}\mathbf{R}\mathbf{f}_0^+ + \boldsymbol{\Theta}\mathbf{R}\mathbf{M}_K^+ \tag{A.1}$$

$$\mathbf{M}_K^+ = \boldsymbol{\Theta}\mathbf{R}^*\mathbf{f}_K^- \tag{A.2}$$

Where the multiplication by $\mathbf{R}$ is the multidimensional convolution with the

reflection response R and multiplication by $\mathbf{\Theta}$ is multiplication by the time window defined by equation 3.9. If we take equation A.1, multiply it by $\mathbf{\Theta R}^*$, where * denotes time reversal, simplify using equation A.2 and rearrange we obtain:

$$[\mathbf{I} - \mathbf{\Theta R}^*\mathbf{\Theta R}]\mathbf{M}_K^+ = \mathbf{\Theta R}^*\mathbf{\Theta R}\mathbf{f}_0^+ \tag{A.3}$$

This equation is now dependent on only one unknown $\mathbf{M}_K^+$ and identified by van der Neut *et al.* (2015b) as a Fredholm equation of the second kind which can therefore be solved as a Neumann series in the form:

$$\mathbf{f}_K^+ = \sum_{k=0}^{K} (\mathbf{\Theta R}^*\mathbf{\Theta R})^k \mathbf{f}_0^+ \tag{A.4}$$

Substituting this result into equation A.2 we can obtain:

$$\mathbf{f}_K^- = \mathbf{\Theta R} \sum_{k=0}^{K} (\mathbf{\Theta R}^*\mathbf{\Theta R})^k \mathbf{f}_0^+ \tag{A.5}$$

Equations A.4 and A.5 are equivalent to those decibed as the iterative Marchenko method in equations 2.4-2.7. It is worth nothing that convergence of this series is not guaranteed, this will only occur when $|(\mathbf{\Theta R}^*\mathbf{\Theta R})^k f_0^+|_2 \to 0$ as $k \to \infty$.

Appendix B

Two-dimensional Marchenko Code

An output and significant point of discussion in chapter 2 is the two-dimesnional Marchenko code. This code can be used for Marchenko redatuming and imaging. Below I have included two links to access this online. This code accompanies an article recently accepted for publication (see Lomas and Curtis (2019)), which is included within this thesis as chapter 2. The original code will be published on the SEG source-code archive (**http://software.seg.org**).

Upon download and extraction the codes/data/documents are organised into three main sections, as we discussed in chapter 2. However, prior to implementing any of the Marchenko codes a data preparation script will need to be executed. The data we have included in the download is stored as *.csv* files, as this was required for publication, these are converted to *.mat* files and reformatted to the correct shape and size within this script.

Below we have include a list outlining the downloaded files and their organisation:

```
marchenko_package_geophysics
├── CODE_1
│   └── ICCR_marchenko.m
├── CODE_2
│   └── ICCR_marchenko_vect.m
├── CODE_3
│   └── ICCR_marchenko_imaging.m
├── ICCR_marchenko_dataprep.m
├── READ_ME.txt
└── UTILS
    ├── FUNCTIONS
    │   ├── ICCR_marchenko_vect_func.m
    │   └── ICCR_marchenko_direct.m
    └── DATA
        ├── DAT
        │   ├── ICCR_marchenko_eik_base.csv
        │   ├── ICCR_marchenko_GT.csv
        │   ├── ICCR_marchenko_R_base.csv
        │   ├── ICCR_marchenko_TD.csv
        │   ├── ICCR_marchenko_theta.csv
        │   ├── ICCR_marchenko_vel.csv
        │   └── ICCR_marchenko_wav.csv
        └── MAT
```

Appendix C

Derivation of the Focusing and Green's Function Relations

In this appendix we derive the governing equations of Marchenko methods from the underlying reciprocity theorems, given in equations 3.1, 3.2, 4.3 and 4.4. Let us begin by defining the components of the wavefield states, where state A is the focusing state, $p_A^{\pm} = f_1^{\pm}(\mathbf{x}, \mathbf{x}_i, \omega)$, and state B is the Green's function state, $p_B^{\pm} = G^{\pm}(\mathbf{x}, \mathbf{x}_0, \omega)$. More details can be found in Wapenaar *et al.* (2014), chapter 4 of this thesis (both two dimensions) as well as chapter 3 of this thesis (three dimensions).

	State A	State B
on $\partial\mathbb{D}_0$	$p_A^+ = f_1^+(\mathbf{x}_0', \mathbf{x}_i, \omega)$	$\partial_z p_B^+ = -\frac{1}{2} j\omega\rho(\mathbf{x}_0')\delta(\mathbf{x}_0 - \mathbf{x}_0')$
	$p_A^- = f_1^-(\mathbf{x}_0', \mathbf{x}_i, \omega)$	$\partial_z p_B^- = \partial_z G(\mathbf{x}_0', \mathbf{x}_0, \omega)$
on $\partial\mathbb{D}_i$	$\partial_z p_A^+ = -\frac{1}{2} j\omega\rho(\mathbf{x}_i')\delta(\mathbf{x}_i - \mathbf{x}_i')$	$p_B^+ = G^+(\mathbf{x}_i', \mathbf{x}_0, \omega)$
	$\partial_z p_A^- = 0$	$p_B^- = G^-(\mathbf{x}_i', \mathbf{x}_0, \omega)$

Table C.1: The directionally decomposed wavefield designations for the focusing state A and Green's function state B. These wavefields are evaluated on the boundaries $\partial\mathbb{D}_0$ and $\partial\mathbb{D}_i$.

We are able to simplify the substituted values in Table C.1 by assuming there are no upgoing signals in the focusing state below $\partial\mathbb{D}_i$, $\partial_z p_A^-|_{z=z_i} = 0$. Additionally the downgoing terms for both the Green's function state and focusing state where the source and observations are on the same boundary equate to the spatial derivative of a delta function in the z direction. If we then substitute the values from Table C.1 into equation 4.3 we obtain:

$$\int_{\partial\mathbb{D}_0} \frac{1}{\rho(\mathbf{x}_0')} \left[f_1^+(\mathbf{x}_0', \mathbf{x}_i, \omega)\partial_z G(\mathbf{x}_0', \mathbf{x}_0, \omega) - f_1^-(\mathbf{x}_0', \mathbf{x}_i, \omega)\frac{1}{2}j\omega\rho(\mathbf{x}_0')\delta(\mathbf{x}_0 - \mathbf{x}_0') \right] d\mathbf{x}_0' = -\int_{\partial\mathbb{D}_i} \frac{1}{\rho(\mathbf{x}_i')} \left[-\frac{1}{2}j\omega\rho(\mathbf{x}_i')\delta(\mathbf{x}_i - \mathbf{x}_i')G^-(\mathbf{x}_i', \mathbf{x}_0, \omega) \right] d\mathbf{x}_i' \quad \text{(C.1)}$$

We can cancel redundant density (ρ) terms and exploit the sifting property of the delta function, $\int f(y)\delta(x-y)dy = f(x)$, to produce:

$$\int_{\partial\mathbb{D}_0} \left[\frac{1}{\rho(\mathbf{x}_0')}\ f_1^+(\mathbf{x}_0', \mathbf{x}_i, \omega)\partial_z G(\mathbf{x}_0', \mathbf{x}_0, \omega) \right] d\mathbf{x}_0' - \frac{1}{2}j\omega f_1^-(\mathbf{x}_0, \mathbf{x}_i, \omega) = \frac{1}{2}j\omega G^-(\mathbf{x}_i, \mathbf{x}_0, \omega) \quad \text{(C.2)}$$

If we then multiply equation C.2 by $2/j\omega$ we obtain:

$$\int_{\partial\mathbb{D}_0} \left[\frac{2}{j\omega\rho(\mathbf{x}_0')} f_1^+(\mathbf{x}_0', \mathbf{x}_i, \omega)\partial_z G(\mathbf{x}_0', \mathbf{x}_0, \omega) \right] d\mathbf{x}_0' - f_1^-(\mathbf{x}_0, \mathbf{x}_i, \omega) = G^-(\mathbf{x}_i, \mathbf{x}_0, \omega) \quad \text{(C.3)}$$

Finally we can take the measured reflection response (R) to be the particle velocity in the z direction (equation 4.8) in response to source and receiver on the boundary $\partial\mathbb{D}_0$ multiplied by -2:

$$R(\mathbf{x}_0, \mathbf{x}_0', \omega) = \frac{2}{j\omega\rho(\mathbf{x}_0')}\partial_z G(\mathbf{x}_0', \mathbf{x}_0, \omega) = -2v_z(\mathbf{x}_0', \mathbf{x}_0, \omega) \tag{C.4}$$

Equation C.3 is therefore equivalent to the equations presented throughout this thesis (e.g. equation 4.2). Furthermore, equations C.3 and C.4 justify the inclusion of the -2 scaling factor in the accompanying MATLAB code which we introduced in chapter 2 and included in appendix A.

For completeness we can also derive an equivalent expression for G^+ by substituting the values from Table C.1 in the the reciprocity theorem of the correlation type from equation 4.4, the steps are similar to those presented above:

$$\begin{aligned}\int_{\partial\mathbb{D}_0} \frac{1}{\rho(\mathbf{x}_0')}\left[-f_1^+(\mathbf{x}_0', \mathbf{x}_i, \omega)^* \frac{1}{2} j\omega\rho(\mathbf{x}_0')\delta(\mathbf{x}_0 - \mathbf{x}_0') + f_1^-(\mathbf{x}_0', \mathbf{x}_i, \omega)^* \partial_z G(\mathbf{x}_0', \mathbf{x}_0, \omega)\right] d\mathbf{x}_0' \\ = -\int_{\partial\mathbb{D}_i} \frac{1}{\rho(\mathbf{x}_i')}\left[-\frac{1}{2} j\omega\rho(\mathbf{x}_i')\delta(\mathbf{x}_i - \mathbf{x}_i')\right]^* G^+(\mathbf{x}_i', \mathbf{x}_0, \omega)\, d\mathbf{x}_i'\end{aligned} \tag{C.5}$$

Alternatively, here we have the complex conjugate of the delta function term on the right side, we can remove this by replacing the imaginary term (j) inside the square bracket with its negative ($-j$), as well as sifting using the delta function and cancelling the density terms we obtain:

$$-\frac{1}{2}j\omega f_1^+(\mathbf{x}_0,\mathbf{x}_i,\omega)^* + \int\limits_{\partial\mathbb{D}_0} \frac{1}{\rho(\mathbf{x}_0')}\left[f_1^-(\mathbf{x}_0',\mathbf{x}_i,\omega)^*\partial_z G(\mathbf{x}_0',\mathbf{x}_0,\omega)\right] d\mathbf{x}_0' = -\frac{1}{2}j\omega G^+(\mathbf{x}_i,\mathbf{x}_0,\omega) \quad \text{(C.6)}$$

We then multiply equation C.6 by $-2/j\omega$ to obtain:

$$f_1^+(\mathbf{x}_0,\mathbf{x}_i,\omega)^* - \int\limits_{\partial\mathbb{D}_0}\left[\frac{2}{j\omega\rho(\mathbf{x}_0')}f_1^-(\mathbf{x}_0',\mathbf{x}_i,\omega)^*\partial_z G(\mathbf{x}_0',\mathbf{x}_0,\omega)\right] d\mathbf{x}_0' = G^+(\mathbf{x}_i,\mathbf{x}_0,\omega) \quad \text{(C.7)}$$

Given our definition in equation C.4, equation C.7 is equivalent to equation 4.1.

Appendix D

Derivation of Virtual Source-Virtual Receiver Marchenko Methods

The starting point of deriving equation 4.5 is the reciportivty theorem of the convolution type given in equation 4.3. If we substitute the wavefield values given in Table 4.1 in this equation we obtain:

$$-\int_{\partial\mathbb{D}_0} \frac{1}{\rho(\mathbf{x}_0)} \left[f_1^+(\mathbf{x}_0,\mathbf{x}_i,\omega)\partial_z G(\mathbf{x}_0,\mathbf{x}_j,\omega)\right] d\mathbf{x}_0 = \int_{\partial\mathbb{D}_i} \frac{1}{\rho(\mathbf{x}_i')} \left[-\frac{1}{2} j\omega\rho(\mathbf{x}_i')\delta(\mathbf{x}_i-\mathbf{x}_i')G^-(\mathbf{x}_i',\mathbf{x}_j,\omega)\right] d\mathbf{x}_i' \quad \text{(D.1)}$$

We have removed all components from equation D.1 that are multiplied by 0 during substitution. If we then exploit the sifting property of the delta function

and cancel the ρ terms on the right hand side we obtain:

$$-\int_{\partial\mathbb{D}_0} \frac{1}{\rho(\mathbf{x}_0)}\ f_1^+(\mathbf{x}_0,\mathbf{x}_i,\omega)\partial_z G(\mathbf{x}_0,\mathbf{x}_j,\omega)\ d\mathbf{x}_0 = -\frac{1}{2}j\omega\ G^-(\mathbf{x}_i,\mathbf{x}_j,\omega) \tag{D.2}$$

Rearranging the terms in equation D.2 gives equation 4.5.

We can undertake a similar process to derive equation 4.6, by substituting the values given in Table 4.1 into the reciprocity theorem of the correlation type from equation 4.4 we obtain:

$$\begin{aligned}-\int_{\partial\mathbb{D}_0} \frac{1}{\rho(\mathbf{x}_0)}\ f_1^-(\mathbf{x}_0,\mathbf{x}_i,\omega)^*\partial_z G(\mathbf{x}_0,\mathbf{x}_j,\omega)\ d\mathbf{x}_0 \\ = \int_{\partial\mathbb{D}_i} \frac{1}{\rho(\mathbf{x}_i')}\left[-\frac{1}{2}j\omega\rho(\mathbf{x}_i')\delta(\mathbf{x}_i-\mathbf{x}_i')\right]^* G^+(\mathbf{x}_i',\mathbf{x}_j,\omega)\ d\mathbf{x}_i'\end{aligned} \tag{D.3}$$

Alternatively to the previous example this time the delta function on the right hand side is a complex conjugate. We therefore replace j with $-j$ inside the square brackets, again exploit the sifting property of the delta function and cancel redundant terms to produce:

$$-\int_{\partial\mathbb{D}_0} \frac{1}{\rho(\mathbf{x}_0)}\ f_1^-(\mathbf{x}_0,\mathbf{x}_i,\omega)^*\partial_z G(\mathbf{x}_0,\mathbf{x}_j,\omega)\ d\mathbf{x}_0 = \frac{1}{2}j\omega\ G^+(\mathbf{x}_i,\mathbf{x}_j,\omega) \tag{D.4}$$

Rearranging the terms in equation D.4 gives equation 4.6.

We can then sum the two resulting equations 4.5 and 4.6, to calculate the total Green's functions ($G = G^+ + G^-$) this gives:

$$G^-(\mathbf{x}_i, \mathbf{x}_j, \omega) + G^+(\mathbf{x}_i, \mathbf{x}_j, \omega) = \int\limits_{\partial\mathbb{D}_0} \frac{2}{j\omega\rho(\mathbf{x}_0)}\ f_1^+(\mathbf{x}_0, \mathbf{x}_i, \omega)\partial_z G(\mathbf{x}_0, \mathbf{x}_j, \omega)\ d\mathbf{x}_0 - \int\limits_{\partial\mathbb{D}_0} \frac{2}{j\omega\rho(\mathbf{x}_0)}\ f_1^-(\mathbf{x}_0, \mathbf{x}_i, \omega)^*\partial_z G(\mathbf{x}_0, \mathbf{x}_j, \omega)\ d\mathbf{x}_0 \quad \text{(D.5)}$$

This can be reduced to:

$$G(\mathbf{x}_i, \mathbf{x}_j, \omega) = \int\limits_{\partial\mathbb{D}_0} \frac{2}{j\omega\rho(\mathbf{x}_0)}\ \partial_z G(\mathbf{x}_0, \mathbf{x}_j, \omega)\left[f_1^+(\mathbf{x}_0, \mathbf{x}_i, \omega) - f_1^-(\mathbf{x}_0, \mathbf{x}_i, \omega)^*\right]\ d\mathbf{x}_0 \quad \text{(D.6)}$$

If we take the definition given in chapter 4 ($f_2(\mathbf{x}_i, \mathbf{x}_0, \omega) = f_1^+(\mathbf{x}_0, \mathbf{x}_i, \omega) - f_1^-(\mathbf{x}_0, \mathbf{x}_i, \omega)^*$), this is equivalent to equation 4.7. We have therefore related virtual source-virtual receiver Green's functions to the focusing and Green's functions between the surface and a subsurface virtual source/virtual receiver.

References

Aki, K. and Richards, P.G. (2002). *Quantitative seismology*.

Amundsen, L. (2001). Elimination of free-surface related multiples without need of the source wavelet. *Geophysics*, **66**, 327–341.

Auer, L., Nuber, A.M., Greenhalgh, S.A., Maurer, H. and Marelli, S. (2013). A critical appraisal of asymptotic 3D-to-2D data transformation in full-waveform seismic crosshole tomography. *Geophysics*, **78**, R235–R247.

Bakulin, A. and Calvert, R. (2006). The virtual source method: Theory and case study. *Geophysics*, **71**, SI139–SI150.

Baysal, E., Kosloff, D.D. and Sherwood, J.W. (1983). Reverse time migration. *Geophysics*, **48**, 1514–1524.

Behura, J., Wapenaar, K. and Snieder, R. (2014). Autofocus imaging: Image reconstruction based on inverse scattering theory. *Geophysics*, **79**, A19–A26.

Bleistein, N. (1986). Two-and-one-half dimensional in-plane wave propagation. *Geophysical Prospecting*, **34**, 686–703.

Brackenhoff, J. (2016). Rescaling of incorrect source strength using Marchenko redatuming.

Brackenhoff, J., Thorbecke, J. and Wapenaar, K. (2018). Homogeneous green's function retrieval on field data using the Marchenko method. In *80th EAGE Conference and Exhibition 2018*.

Broggini, F., Snieder, R. and Wapenaar, K. (2012). Focusing the wavefield inside an unknown 1D medium: Beyond seismic interferometry. *Geophysics*, **77**, A25–A28.

Broggini, F., Wapenaar, K., Neut, J. and Snieder, R. (2014). Data-driven Green's function retrieval and application to imaging with multidimensional deconvolution. *Journal of Geophysical Research: Solid Earth*, **119**, 425–441.

Buske, S. (1999). Three-dimensional pre-stack Kirchhoff migration of deep seismic reflection data. *Geophysical Journal International*, **137**, 243–260.

Cassereau, D. and Fink, M. (1992). Time-reversal of ultrasonic fields. iii. theory of the closed time-reversal cavity. *IEEE transactions on ultrasonics, ferroelectrics, and frequency control*, **39**, 579–592.

Claerbout, J.F. (1971). Toward a unified theory of reflector mapping. *Geophysics*, **36**, 467–481.

Cui, T., Becker, T.S., van Manen, D.J., Rickett, J.E. and Vasconcelos, I. (2018a). Marchenko redatuming in a dissipative medium: Numerical and experimental implementation. *Physical Review Applied*, **10**, 044022.

Cui, T., Vasconcelos, I., Manen, D.J.v. and Wapenaar, K. (2018b). A tour of Marchenko redatuming: Focusing the subsurface wavefield. *The Leading Edge*, **37**, 67a1–67a6.

Curtis, A. and Halliday, D. (2010). Source-receiver wave field interferometry. *Physical Review E*, **81**, 046601.

Curtis, A., Gerstoft, P., Sato, H., Snieder, R. and Wapenaar, K. (2006). Seismic interferometry – turning noise into signal. *The Leading Edge*, **25**, 1082–1092.

Curtis, A., Nicolson, H., Halliday, D., Trampert, J. and Baptie, B. (2009). Virtual seismometers in the subsurface of the earth from seismic interferometry. *Nature Geoscience*, **2**, 700.

da Costa Filho, C.A. and Curtis, A. (2016). Attenuating multiple-related imaging artifacts using combined imaging conditions. *Geophysics*, **81**, S469–S475.

da Costa Filho, C.A., Ravasi, M., Curtis, A. and Meles, G.A. (2014). Elastodynamic Green's function retrieval through single-sided Marchenko inverse scattering. *Physical Review E*, **90**, 063201.

da Costa Filho, C.A., Ravasi, M. and Curtis, A. (2015). Elastic P-and S-wave autofocus imaging with primaries and internal multiples. *Geophysics*, **80**, S187–S202.

da Costa Filho, C.A., Meles, G.A. and Curtis, A. (2017). Elastic internal multiple analysis and attenuation using marchenko and interferometric methods. *Geophysics*, **82**, Q1–Q12.

da Costa Filho, C.A., Tant, K., Curtis, A., Mulholland, A. and Moran, C.M. (2018). Using laboratory experiments to develop and test new Marchenko and imaging methods. In *SEG Technical Program Expanded Abstracts 2018*, 4352–4356, Society of Exploration Geophysicists.

Davydenko, M. and Verschuur, D. (2013). Full wavefield migration without dip limitation-using duplex waves in the imaging with multiples. In *75th EAGE Conference & Exhibition incorporating SPE EUROPEC 2013*.

Etgen, J. and Regone, C. (1998). Strike shooting, dip shooting, widepatch shootingdoes prestack depth migration care? a model study. In *SEG Technical Program Expanded Abstracts 1998*, 66–69, Society of Exploration Geophysicists.

Etgen, J.T. (1994). Stability of explicit depth extrapolation through laterally-varying media. In *SEG Technical Program Expanded Abstracts 1994*, 1266–1269, Society of Exploration Geophysicists.

Fleury, C. and Vasconcelos, I. (2012). Imaging condition for nonlinear scattering-based imaging: Estimate of power loss in scattering. *Geophysics*, **77**, S1–S18.

Galetti, E., Halliday, D. and Curtis, A. (2013). A simple and exact acoustic wavefield modeling code for data processing, imaging, and interferometry applications. *Geophysics*, **78**, F17–F27.

Halliday, D. and Curtis, A. (2010). An interferometric theory of source-receiver scattering and imaging. *Geophysics*, **75**, SA95–SA103.

Hornby, B.E. and Yu, J. (2007). Interferometric imaging of a salt flank using walkaway VSP data. *The Leading Edge*, **26**, 760–763.

Ikelle, L. and Amundsen, L. (2005). *Introduction to Petroleum Seismology*, vol. 12. SEG Books.

Jakubowicz, H. (1998). Wave equation prediction and removal of interbed multiples. In *SEG Technical Program Expanded Abstracts 1998*, 1527–1530, Society of Exploration Geophysicists.

Jia, X., Guitton, A., Singh, S. and Snieder, R. (2017). Subsalt Marchenko imaging: A Gulf of Mexico example. In *SEG Technical Program Expanded Abstracts 2017*, 5588–5592, Society of Exploration Geophysicists.

Jia, X., Guitton, A. and Snieder, R. (2018). A practical implementation of subsalt Marchenko imaging with a gulf of mexico dataset. *Geophysics*, **83**, 1–57.

Jin, S., Xu, S. and Walraven, D. (2006). One-return wave equation migration: Imaging of duplex waves. In *SEG Technical Program Expanded Abstracts 2006*, 2338–2342, Society of Exploration Geophysicists.

Jones, I. (2014). Tutorial: migration imaging conditions. *First Break*, **32**, 45–55.

Jones, I.F. (2010). Tutorial: Velocity estimation via ray-based tomography. *First Break*, **28**, 45–52.

Kaelin, B. and Guitton, A. (2006). Imaging condition for reverse time migration. In *SEG Technical Program Expanded Abstracts 2006*, 2594–2598, Society of Exploration Geophysicists.

Kelly, K., Ward, R., Treitel, S. and Alford, R. (1976). Synthetic seismograms: a finite-difference approach. *Geophysics*, **41**, 2–27.

Liu, Y., van der Neut, J., Arntsen, B. and Wapenaar, K. (2016). Combination of surface and borehole seismic data for robust target-oriented imaging. *Geophysical Journal International*, **205**, 758–775.

Liu, Y., Arntsen, B., van der Neut, J. and Wapenaar, K. (2018). Up-and downgoing borehole wavefield retrieval using single component borehole and reflection data. *Journal of Applied Geophysics*, **155**, 256–264.

Lomas, A. and Curtis, A. (2017). 3D seismic imaging using Marchenko methods. In *AGU Fall Meeting Abstracts*, NS31C–03.

Lomas, A. and Curtis, A. (2019). An introduction to marchenko methods for imaging. *Geophysics*, **84**, F35–F45.

Lomas, A., Singh, S. and Curtis, A. (2018). Marchenko imaging of both vertical and horizontal interfaces using VSP data. 5027–5031.

Malcolm, A.E., Ursin, B. and De Hoop, M.V. (2009). Seismic imaging and illumination with internal multiples. *Geophysical Journal International*, **176**, 847–864.

Marchenko, V.A. (1955). On reconstruction of the potential energy from phases of the scattered waves. In *Dokl. Akad. Nauk SSSR*, vol. 104, 695–698.

Martin, G.S., Wiley, R. and Marfurt, K.J. (2006). Marmousi2: An elastic upgrade for Marmousi. *The Leading Edge*, **25**, 156–166.

Mayne, W.H. (1962). Common reflection point horizontal data stacking techniques. *Geophysics*, **27**, 927–938.

McMechan, G.A. (1983). Migration by extrapolation of time-dependent boundary values. *Geophysical Prospecting*, **31**, 413–420.

Meles, G.A., Löer, K., Ravasi, M., Curtis, A. and da Costa Filho, C.A. (2014). Internal multiple prediction and removal using Marchenko autofocusing and seismic interferometry. *Geophysics*, **80**, A7–A11.

Meles, G.A., Wapenaar, K. and Curtis, A. (2016). Reconstructing the primary reflections in seismic data by Marchenko redatuming and convolutional interferometry. *Geophysics*, **81**, Q15–Q26.

Meles, G.A., Wapenaar, K. and Thorbecke, J. (2018). Virtual plane-wave imaging via Marchenko redatuming. *Geophysical Journal International*, **214**, 508–519.

Mildner, C., Becker, T.S., de Vos, K., Broggini, F. and Robertsson, J.O. (2017). Source wavelet estimation using Marchenko focusing functions: Theory and laboratory data example. In *SEG Technical Program Expanded Abstracts 2017*, 5521–5525, Society of Exploration Geophysicists.

Mulder, W.A. and Plessix, R.E. (2004). A comparison between one-way and two-way wave-equation migration. *Geophysics*, **69**, 1491–1504.

Plessix, R.E. and Mulder, W. (2004). Frequency-domain finite-difference amplitude-preserving migration. *Geophysical Journal International*, **157**, 975–987.

Pratt, R.G. (1999). Seismic waveform inversion in the frequency domain, part 1: Theory and verification in a physical scale model. *Geophysics*, **64**, 888–901.

Pratt, R.G., Shin, C. and Hick, G. (1998). Gauss–Newton and full Newton methods in frequency–space seismic waveform inversion. *Geophysical Journal International*, **133**, 341–362.

Ravasi, M. (2017). Rayleigh-Marchenko redatuming for target-oriented, true-amplitude imaging. *Geophysics*, **82**, S439–S452.

Ravasi, M., Vasconcelos, I., Kritski, A., Curtis, A., Filho, C.A.d.C. and Meles, G.A. (2016). Target-oriented Marchenko imaging of a North Sea field. *Geophysical Supplements to the Monthly Notices of the Royal Astronomical Society*, **205**, 99–104.

Rose, J.H. (2001). Single-sided focusing of the time-dependent Schrödinger equation. *Physical Review A*, **65**, 012707.

Rose, J.H. (2002). Single-sided autofocusing of sound in layered materials. *Inverse problems*, **18**, 1923.

Sava, P. and Biondi, B. (2004). Wave-equation migration velocity analysis. i. theory. *Geophysical Prospecting*, **52**, 593–606.

Schneider, W.A. (1978). Integral formulation for migration in two and three dimensions. *Geophysics*, **43**, 49–76.

Singh, S. and Curtis, A. (2018). Imaging vertical interfaces using acoustic time-reversal. *Geophysics*, **Submitted**.

Singh, S. and Snieder, R. (2017a). Source-receiver Marchenko redatuming: Obtaining virtual receivers and virtual sources in the subsurface. *Geophysics*, **82**, Q13–Q21.

Singh, S. and Snieder, R. (2017b). Strategies for imaging with Marchenko-retrieved Greens functions. *Geophysics*, **82**, 1–68.

Singh, S., Snieder, R., Behura, J., van der Neut, J., Wapenaar, K. and Slob, E. (2015). Marchenko imaging: Imaging with primaries, internal multiples, and free-surface multiples. *Geophysics*, **80**, S165–S174.

Singh, S., Snieder, R., van der Neut, J., Thorbecke, J., Slob, E. and Wapenaar, K. (2016). Accounting for free-surface multiples in Marchenko imaging. *Geophysics*, **82**, R19–R30.

Slob, E. (2016). Green's function retrieval and marchenko imaging in a dissipative acoustic medium. *Physical review letters*, **116**, 164301.

Slob, E. and Wapenaar, K. (2017). Theory for marchenko imaging of marine seismic data with free surface multiple elimination. In *79th EAGE Conference and Exhibition 2017*.

Slob, E., Hunziker, J., Thorbecke, J. and Wapenaar, K. (2014a). Creating virtual vertical radar profiles from surface reflection ground penetrating radar data. In *Ground Penetrating Radar (GPR), 2014 15th International Conference on*, 525–528, IEEE.

Slob, E., Wapenaar, K., Broggini, F. and Snieder, R. (2014b). Seismic reflector imaging using internal multiples with Marchenko-type equations. *Geophysics*, **79**, S63–S76.

Snieder, R. (2004a). Extracting the Green's function from the correlation of coda waves: A derivation based on stationary phase. *Physical Review E*, **69**, 046610.

Snieder, R. (2004b). *A Guided Tour of Mathematical Methods*. Cambridge University Press.

Snieder, R. (2015). Demystifying Marchenko imaging. In *77th EAGE Conference and Exhibition-Workshops*.

Staring, M., Pereira, R., Douma, H., van der Neut, J. and Wapenaar, K. (2018). Source-receiver Marchenko redatuming on field data using an adaptive double-focusing method. *Geophysics*, **83**, 1–48.

Stork, C. (1992). Reflection tomography in the postmigrated domain. *Geophysics*, **57**, 680–692.

Tarantola, A. (1984). Inversion of seismic reflection data in the acoustic approximation. *Geophysics*, **49**, 1259–1266.

Thomsen, H. (2016). Investigating the robustness of Green's function retrieval via Marchenko focusing and seismic interferometry.

Thomsen, H.R., Broggini, F., van Manen, D.J., Ravasi, M. and Kritski, A. (2017). Robust Marchenko focusing-calibrating surface reflection with VSP data. In *79th EAGE Conference and Exhibition 2017*.

Thorbecke, J., Slob, E., Brackenhoff, J., van der Neut, J. and Wapenaar, K. (2017). Implementation of the Marchenko method. *Geophysics*, **82**, 1–56.

Thorbecke, J.W. and Draganov, D. (2011). Finite-difference modeling experiments for seismic interferometry. *Geophysics*, **76**, H1–H18.

Urruticoechea, C.R. and Wapenaar, C. (2017). Elastodynamic single-sided homogeneous Green's function representation-theory and examples. In *79th EAGE Conference and Exhibition 2017*.

van der Neut, J. and Wapenaar, K. (2016). Adaptive overburden elimination with the multidimensional Marchenko equation. *Geophysics*, **81**, T265–T284.

van der Neut, J., Thorbecke, J., Mehta, K., Slob, E. and Wapenaar, K. (2011). Controlled-source interferometric redatuming by crosscorrelation and multidimensional deconvolution in elastic media. *Geophysics*, **76**, SA63–SA76.

van der Neut, J., Thorbecke, J., Wapenaar, K. and Slob, E. (2015a). Inversion of the multidimensional Marchenko equation. In *77th EAGE Conference and Exhibition 2015*.

van der Neut, J., Vasconcelos, I. and Wapenaar, K. (2015b). On Green's function retrieval by iterative substitution of the coupled Marchenko equations. *Geophysical Journal International*, **203**, 792–813.

van der Neut, J., Wapenaar, K., Thorbecke, J. and Slob, E. (2015c). Practical challenges in adaptive Marchenko imaging. In *SEG Technical Program Expanded Abstracts 2015*, 4505–4509, Society of Exploration Geophysicists.

van der Neut, J., Wapenaar, K., Thorbecke, J., Slob, E. and Vasconcelos, I. (2015d). An illustration of adaptive Marchenko imaging. *The Leading Edge*, **34**, 818–822.

van der Neut, J., Johnson, J.L., van Wijk, K., Singh, S., Slob, E. and Wapenaar, K. (2017). A Marchenko equation for acoustic inverse source problems. *The Journal of the Acoustical Society of America*, **141**, 4332–4346.

van Manen, D.J., Robertsson, J.O. and Curtis, A. (2005). Modeling of wave propagation in inhomogeneous media. *Physical Review Letters*, **94**, 164301.

van Manen, D.J., Curtis, A. and Robertsson, J.O. (2006). Interferometric modeling of wave propagation in inhomogeneous elastic media using time reversal and reciprocity. *Geophysics*, **71**, SI47–SI60.

van Trier, J. and Symes, W.W. (1991). Upwind finite-difference calculation of traveltimes. *Geophysics*, **56**, 812–821.

Vasconcelos, I. (2008). Generalized representations of perturbed fieldsapplications in seismic interferometry and migration. In *SEG Technical Program Expanded Abstracts 2008*, 2927–2931, Society of Exploration Geophysicists.

Vasconcelos, I. (2013). Source-receiver, reverse-time imaging of dual-source, vector-acoustic seismic data. *Geophysics*, **78**, WA123–WA145.

Vasconcelos, I., Sava, P. and Douma, H. (2010). Nonlinear extended images via image-domain interferometry. *Geophysics*, **75**, SA105–SA115.

Verschuur, D.J., Berkhout, A. and Wapenaar, C. (1992). Adaptive surface-related multiple elimination. *Geophysics*, **57**, 1166–1177.

Vidale, J. (1988). Finite-difference calculation of travel times. *Bulletin of the Seismological Society of America*, **78**, 2062–2076.

Virieux, J. and Operto, S. (2009). An overview of full-waveform inversion in exploration geophysics. *Geophysics*, **74**, WCC1–WCC26.

Wapenaar, C. and Grimbergen, J. (1996). Reciprocity theorems for one-way wavefields. *Geophysical Journal International*, **127**, 169–177.

Wapenaar, K. (2014). Single-sided Marchenko focusing of compressional and shear waves. *Physical Review E*, **90**, 063202.

Wapenaar, K. and Fokkema, J. (2006). Green's function representations for seismic interferometry. *Geophysics*, **71**, SI33–SI46.

Wapenaar, K. and Slob, E. (2014). On the Marchenko equation for multicomponent single-sided reflection data. *Geophysical Journal International*, **199**, 1367–1371.

Wapenaar, K., Slob, E. and Snieder, R. (2008). Seismic and electromagnetic controlled-source interferometry in dissipative media. *Geophysical prospecting*, **56**, 419–434.

Wapenaar, K., Broggini, F., Slob, E. and Snieder, R. (2013). Three-dimensional single-sided Marchenko inverse scattering, data-driven focusing, Greens function retrieval, and their mutual relations. *Physical Review Letters*, **110**, 084301.

Wapenaar, K., Thorbecke, J., van der Neut, J., Broggini, F., Slob, E. and Snieder, R. (2014). Marchenko imaging. *Geophysics*, **79**, WA39–WA57.

Wapenaar, K., Thorbecke, J. and van der Neut, J. (2016). A single-sided homogeneous Green's function representation for holographic imaging, inverse scattering, time-reversal acoustics and interferometric Green's function retrieval.

Geophysical Supplements to the Monthly Notices of the Royal Astronomical Society, **205**, 531–535.

Wapenaar, K., Thorbecke, J., van der Neut, J., Slob, E. and Snieder, R. (2017). Virtual sources and their responses, part ii: data-driven single-sided focusing. *Geophysical Prospecting*, **65**, 1430–1451.

Wapenaar, K., Brackenhoff, J., Thorbecke, J., van der Neut, J., Slob, E. and Verschuur, E. (2018). Virtual acoustics in inhomogeneous media with single-sided access. *Scientific reports*, **8**, 2497.

Weglein, A.B., Gasparotto, F.A., Carvalho, P.M. and Stolt, R.H. (1997). An inverse-scattering series method for attenuating multiples in seismic reflection data. *Geophysics*, **62**, 1975–1989.

Whitmore, N.D. (1983). Iterative depth migration by backward time propagation. In *SEG Technical Program Expanded Abstracts 1983*, 382–385, Society of Exploration Geophysicists.

Xu, S. and Jin, S. (2006). Wave equation migration of turning waves. In *SEG Technical Program Expanded Abstracts 2006*, 2328–2332, Society of Exploration Geophysicists.

Yilmaz, Ö. (2001). *Seismic data analysis*, vol. 1. Society of Exploration Geophysicists Tulsa.

Zuberi, M. and Alkhalifah, T. (2014). Generalized internal multiple imaging. *Geophysics*, **79**, S207–S216.